Dissertation

MIMO Satellite Communications for Fixed Satellite Services

Robert Schwarz

der Bundeswehr
Universität München

Faculty of Electrical Engineering and Information Technology
Institute of Information Technology
Chair of Signal Processing

Supervisor and first reviewer	Professor Dr.-Ing. Andreas Knopp, MBA
Second reviewer	Professor Dr. María Ángeles Vázquez Castro

October 2019

UNIVERSITÄT DER BUNDESWEHR MÜNCHEN

MIMO Satellite Communications for Fixed Satellite Services

Robert Schwarz

Vollständiger Abdruck der von der Fakultät für Elektrotechnik und Informationstechnik der Universität der Bundeswehr München zur Erlangung des akademischen Grades eines

Doktor-Ingenieurs

genehmigten Dissertation.

Gutachter:

1. Universitätsprofessor Dr.-Ing. Andreas Knopp, MBA
2. Professor Dr. María Ángeles Vázquez Castro

Die Dissertation wurde am 09.04.2019 bei der Universität der Bundeswehr München eingereicht und durch die Fakultät für Elektrotechnik und Informationstechnik am 02.09.2019 angenommen. Die mündliche Prüfung fand am 18.10.2019 statt.

Acknowledgement

First and foremost, I would like to express my sincere gratitude to my supervisor, Professor Andreas Knopp, for giving me the opportunity to write this thesis. Thank you Andreas, for your support, your steady inspiration and guidance not only throughout this thesis but also during the last 15 years that we have been working together. I am extremely thankful especially for the very exciting and successful time together in the Federal Office of the Bundeswehr for Information Management and Information Technology, where we were (and still are) involved in the SATCOM program of the Bundeswehr. In particular your inspiration in the summer of 2007 motivated me to start with the first simulation of MIMO over Satellite. Your critical view in the following years, suggestions and research directions to put this topic into the right context, have greatly enhanced the value of this contribution to the scientific community and SATCOM industry in general. Without your encouragement, this work would not have been possible.

I would also like to thank Professor Berthold Lankl for his guidance and support through my early years as an external doctoral student at his institute and for agreeing to serve as chairman of my dissertation committee. I am also very grateful to Professor María Ángeles Vázquez Castro from the Universitat Autònoma de Barcelona for agreeing to serve as a second reviewer.

I would also like to thank my former employer, the Federal Office of the Bundeswehr for Information Management and Information Technology, for giving me the outstanding opportunity to be a part of the SATCOM program of the Bundeswehr. In particular, I would like to express my deep gratitude to my former chief Colonel Pirmin Meisenheimer for his enormous trust in me and my work. Pirmin, you provided me the best and most flexible working environment which certainly surpassed anything that I could have expected. During that time I gained extremely valuable experience and had an excellent insight into the SATCOM business and the industry.

I would like to thank all my colleagues, members and former members of the Chair of Signal Processing for their open and cooperative spirit and a stimulating working environment. In particular, I would like to acknowledge Christian Hofmann, who gratefully substituted for me last summer when I wrote this thesis and he finally managed the calibration phase of our new anchor station antennas. I wish also to thank Dirk Ogermann, who is now with Rohde & Schwarz, for his commitment in the early years. A special thank goes to Kai-Uwe Storek and Thomas Delamotte

for the very fruitful and stimulating discussions. Thomas, your exceptionally detailed and very critical view on methods, approaches and results is really a valuable feedback and you contributed to the quality of my work.

I am also indebted to my fellow doctoral students for their feedback and the cooperation in the numerous projects we had to manage. I would also like to thank Professor Werner Wolf who provided useful comments and corrections in the final stage of this thesis. Special credits are due to Wolfgang Weber, Wolfgang Hanzl, our head of IT, and Josef Dochtermann for their exceptional support in the preparation of all measurement campaigns and numerous demonstrations, and in the establishment of our SATCOM research facility, the Munich Center for Space Communications.

I also would like to acknowledge Balachander (Bala) Ramamurthy and Professor Bill Cowley from the University of South Australia, as well as Gerald Bolding from the Defence Science and Technology Group for supporting Bala's research trip to us. Bala, I really appreciate the time we spent together during your visit in Germany. A special thank goes to Hans-Peter Schmitt, Fritz Schurig and their colleagues from Eutelsat who have supported us for many years with satellite access and capacity for scientific purposes and measurements. I am also very grateful to my neighbor Paul for proofreading and his suggestions on how to approach optimization problems, but also to his wife Ana for allowing him to spend that time in the evenings and on the weekends.

Last but not the least, I would like to thank my family: my parents who never gave up to believe that this journey will ever has an end, but in particular my lovely wife Maja. I really appreciate your phenomenal support especially with our two children Paulina and Ferdinand. The completion of this dissertation would not have been possible without your faithful support not only during the last months when I started writing. Thank you very much especially for your enduring patience with me and your understanding for the many nights and long weekends I spent the last years to meet yet again the next paper submission deadline.

I thankfully dedicate this thesis to my wife.

Gronsdorf, April 2019, Robert Schwarz

Abstract

This work investigates the potentials of the multiple-input multiple-output (MIMO) technology to improve the throughput of geostationary satellite systems for fixed satellite services (FSS). The data rate performance of modern satellite systems, such as high-throughput satellites (HTSs) with multibeam antennas, is limited by interference between adjacent antenna beams rather than by thermal noise at the receiver. The distribution of multiple antennas in space, which is also known as spatial MIMO in the literature, provides a further degree of freedom. This additional degree of freedom can be exploited to address the interference issue and, in the optimal case, achieve a linear increase of the throughput with the minimum of the number of antennas on ground and in orbit.

To achieve this gain, interference alignment is performed through a careful arrangement of the satellite and ground antennas. The geometrical lengths of the Line-of-Sight (LOS) propagation paths between all antennas must have a particular difference such that the MIMO signals at the receive antennas are combined with a distinct offset in phase. This requires a particular geometrical positioning of the satellite and ground antennas. The criterion of the **O**ptimal **P**ositioning of the MIMO **A**ntennas (OPA) is derived that allows to optimally place the antennas on Earth and in orbit such that the maximum channel capacity is achieved. The spacing between the antennas is a key parameter in the design of a maximum-capacity MIMO satellite communication system. Based on the antenna spacing in orbit, basically three different categories of MIMO satellite scenarios are defined: The Single-Satellite Application, the Co-Located Satellites Application and the Multiple-Satellites Application.

All relevant effects that possibly degrade the MIMO capacity of a geometrically optimized satellite system are identified, including atmospheric perturbations, antenna patterns and satellite motion in orbit. Their impact on the capacity is thoroughly analyzed and the necessary positioning accuracy of the antennas to achieve high capacity gains is presented. As a basic result, no practical constraints prohibit the application of MIMO to FSS. Simulation results of an HTS scenario with MIMO in the feeder link and full frequency reuse in a multiuser MIMO downlink show the data rate advantage compared to the state-of-the-art. Measurement results collected with a MIMO satellite testbed support the theory presented in this work. The presented approach provides the necessary fundamentals to practically achieve the capacity gains that are promised by spatial MIMO.

Kurzfassung

Diese Arbeit untersucht die Potenziale der Multiple-Input Multiple-Output (MIMO) Technologie mit dem Ziel, den Datendurchsatz von geostationären Satellitensystemen für den festen Satellitenfunk (FSS) zu steigern. Die erreichbare Datenrate moderner Satellitensysteme, wie beispielsweise High-Throughput-Satelliten (HTS) mit Multibeam Antennen, ist weniger durch thermisches Rauschen am Empfänger, sondern vielmehr durch Interferenzen benachbarter Beams begrenzt. Die räumliche Verteilung von mehreren Antennen bietet hierbei einen bisher ungenutzten Freiheitsgrad. Mit dem als räumliches MIMO bekannten Verfahren können die Limitierungen durch Interferenz aufgehoben und es kann gleichzeitig eine mit der Anzahl der genutzten Antennen lineare Steigerung der Datenrate erreicht werden.

Um diesen Gewinn zu erzielen, werden die Bodenstations- und Satellitenantennen so angeordnet, dass sich eine vorteilhafte Überlagerung zwischen Nutz- und Interferenzsignal ergibt (Interference Alignment). Die Längendifferenzen der Line-of-Sight Ausbreitungspfade müssen einen definierten Wert annehmen, so dass sich die Signale mit einer entsprechenden Phasendifferenz an den Empfangsantennen überlagern. Diese Anforderung führt zu bestimmten räumlichen Anordnungen der Antennen am Boden und im Orbit. Es wird das als **O**ptimal **P**ositioning of the MIMO **A**ntennas (OPA) bezeichnete Kriterium eingeführt. MIMO Satellitensysteme, die das OPA Kriterium erfüllen, erreichen die maximale Kanalkapazität. Der Antennenabstand ist ein Schlüsselparameter, wobei sich anhand des Antennenabstandes im Orbit drei Kategorien wie folgt unterscheiden lassen: Einsatellitenanwendungen, Kolokierte Satellitenanwendungen und Mehrsatellitenanwendungen.

In dieser Arbeit werden alle relevanten Effekte – einschließlich atmosphärischer Störungen und Satellitenbewegungen im Orbit – identifiziert, die möglicherweise die Kapazität des geometrisch optimierten Systems reduzieren. Ihr Einfluss wird ausführlich untersucht und die erforderliche Genauigkeit bei der Antennenpositionierung dargestellt. Im Ergebnis zeigen sich keine nennenswerten Einschränkungen, die eine praktische Anwendung von MIMO für den FSS verhindern würden. Simulationsergebnisse eines HTS Szenarios mit MIMO im Feederlink sowie mit voller Frequenzwiederverwendung im Multiuser Downlink zeigen den Datenratengewinn im Vergleich zu herkömmlichen Systemdesigns. Mit einer MIMO Satellitentestanlage aufgenommene Messergebnisse bestätigen die entwickelte Theorie. Das in dieser Arbeit entwickelte Verfahren legt den Grundstein dafür, die theoretisch möglichen Gewinne der räumlichen MIMO Technologie auch praktisch erzielen zu können.

Contents

1. Introduction

1.1. Motivation and Background

Arthur C. Clarke's visionary idea in 1945 to place three *extra-terrestrial relays* into a stationary orbit [Cla45] inspired communications engineers and system designers around the globe. Today almost 1200 active satellites are located in the geostationary earth orbit (GEO) [Uni]. The reason for this impressive success is the ability of a geostationary satellite to bridge large ranges without a need of terrestrial radio or cable based infrastructure at reasonable costs [MB09]. A single satellite in the GEO covers already 43 % of the Earth's surface. In contrast to terrestrial communications networks, new services can be quickly rolled out over a wide area reaching millions of subscribers at once [ETC+11]. Since the geostationary satellite appears fixed in the sky, the ground antennas are very simple to deploy so that also non-professional users are easily able to accomplish the antenna installation, e.g. on a house roof. Because of these great advantages, geostationary satellite communication (SATCOM) plays a vital role of people's everyday life at home and in business, constituting an indispensable part of our global communications infrastructure. Millions of households and business users have pointed a small dish towards the sky and receive broadband fixed satellite services (FSS) such as television (TV) broadcasting[1] or Internet access.

The advent of the Internet along with the introduction of Video-on-Demand (VoD) services has considerably changed the user's expectations how multimedia contents and Internet Protocol (IP) based services shall be delivered. Broadcasting of same video content to many home users has been the key application scenario of geostationary satellite systems for many decades. Meanwhile, individually selectable content at any time is the current state-of-the art, which requires the implementation of unicast transmission capabilities in future satellite systems in order to compete with terrestrial telecommunications systems [MVCS11]. Moreover, the advent of 5G networks and the introduction of integrated satellite-terrestrial architectures will considerably change the role of SATCOM in the near future [EWL+05]. Traffic offloading to the network edges, backhauling or direct broadband access (e.g., VoD) to remote areas belong to the most promising use cases of SATCOM

[1] For example, the satellite fleet of the Société Européenne des Satellites (SES) reaches over 145 million households around the world [SES17b] of which 17.7 million are located in Germany and receive satellite TV as primary source of TV reception [SES17a].

[SCA18]. Other use cases include the delivery of broadband data to earth station on mobile platforms (ESOMPs) like trains, cruise ships and airplanes. In addition, high-definition (HD) and, more recently, ultra-high-definition (UHD) multimedia contents have dramatically increased the data rate demands to be supported by modern satellite systems for FSS [MVCS11]. This challenge will persist, as the global IP data traffic is expected to increase nearly threefold over the next five years. Globally, IP video traffic will be 82 % of all consumer Internet traffic by 2021 [CIS17].

This sustaining demand for higher data rates has motivated the development of high-throughput satellites (HTSs) in the past decade. While the first commercial geostationary satellite *Early Bird* in 1965 provided a capacity of 240 telephone circuits *or* one TV channel [Pel10], the first generation of broadband satellites, such as the WildBlue I launched in 2004, provided a total capacity of already around 20 Gb/s [VVL+12a]. The real era of HTSs was opened by Eutelsat's KA-SAT in 2010 [FTA+16] and the ViaSat-1 in 2011 providing total capacities of up to 90 Gb/s and 140 Gb/s, respectively [VVL+12a]. The ViaSat-2, launched in 2017, provides a total throughput of about 300 Gb/s. This HTS is currently the highest-capacity communications satellite in orbit. The 1 Tb/s of the ViaSat-3, expected launch in 2020 [KET+14], will certainly not be the end of the scale. These peak data rates are necessary to follow the technical and economical demands of the market [CIS17]. The service costs per bit must be drastically reduced in order to remain competitive with the terrestrial counter parts [Gay09]. To achieve this goal, the logical way is to further increase the capacity per satellite by simultaneously decreasing the production costs.

One obvious solution to further increase the system capacity is to additionally exploit higher frequency bands because the capacity scales linearly with the frequency bandwidth. The Ku band as the traditional frequency band used for broadband FSS has recently proven incapable to provide sufficient bandwidth to approach the 1 Tb/s per satellite [Gay09]. Current HTSs operate in the Ka band, but even higher bands such as the Q/V band (40/50 GHz) or the W band (70/80 GHz) are considered necessary to achieve the 1 Tb/s regime and go beyond [Gay09, KET+14].

Simply using higher frequency bands alone is still insufficient to achieve even several tens of gigabit per second. To realize such data rates, one important key technology of modern HTSs is multibeam antennas (see Figure 1.1 for an illustration of a typical HTS architecture). They create hundreds of geographically separated spot beams in the service area, basically similar to the cellular coverage of the fourth generation of terrestrial mobile networks (4G) or its successor 5G. This allows to reuse the available frequency spectrum multiple times, which translates into a *linear increase* of the system capacity. While the KA-SAT supports already a total of 82 spot beams, ViaSat claims to deploy around 2000 very narrow and highly focusing

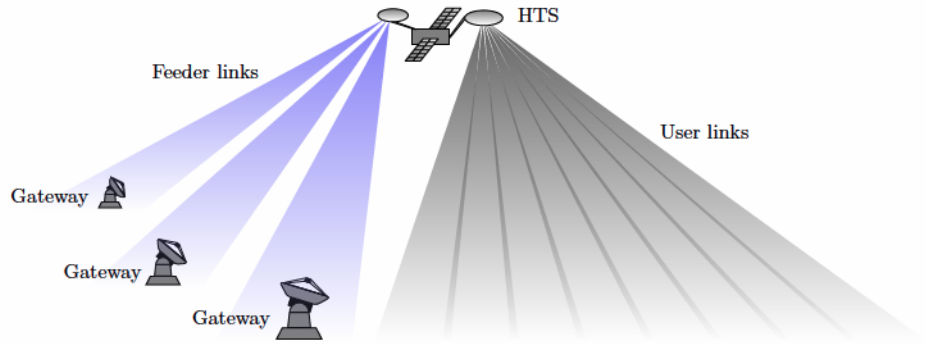

Figure 1.1.: HTS system showing multiple geographically separated gateway stations in the feeder link and a multibeam architecture in the user links

beams with a single ViaSat-3 HTS. An attractive possibility to further increase the capacity seems to be the use of even larger satellite antennas resulting in narrower and more spot beams over the same area. Dimensional constraints on the satellites, however, as well as requirements regarding the pointing stability and beam-isolation limit the size and the number of the antennas in practice.

The insufficient isolation between the beams and the resulting inter-beam interference are indeed the major obstacles to achieve the envisaged linear capacity increase. In the user links, especially those users who are located at the edge of the beams suffer from the most severe inter-beam interference, which is also known as co-channel interference (CCI). As a consequence, they experience a strong degradation of their achievable carrier-to-interference-noise-ratio (CINR), which ultimately limits their data rates. One approach to reduce this interference is to split the available spectral resource in terms of frequency and polarization into sub-bands, and assign a unique sub-band to each beam so that adjacent beams do not use the same frequency and polarization. If the angular separation between two beams is sufficiently large, the same frequency/polarization sub-band can then be reused. The degree of reuse is often described numerically by means of a frequency and polarization reuse factor [MB09]. The conventional solution today is the so-called four color frequency reuse (FR4) scheme, in which four sub-bands (colors) are defined. Each color refers to a unique combination of a frequency sub-band and polarization. While orthogonality between adjacent beams is then achieved by using disjoint frequencies and polarizations (i.e. disjoint colors), only one fourth of the total available spectral resources (half of the spectrum, one of two polarizations) are exploited per beam. To approach the 1 Tb/s, the resort to a full frequency reuse (FFR) is deemed to be necessary [KET+14], where in each beam the full frequency band and all polarizations are used.

In the feeder link, a full reuse of the frequency spectrum among the gateways is

already common practice in order to support the aggregate user link bandwidth of several hundreds of gigahertz. Moreover, even though up to 5 GHz of bandwidth is available in the Q/V band, tens of gateway stations will still be necessary in future designs [KET+14, DSSK18]. The isolation between feeder beams is achieved by gateway locations that are sufficiently far apart, but finding appropriate locations for all gateways becomes challenging. The usable geographical region is limited (e.g. Western Europe), and technical aspects (e.g. required backbone connectivity) additionally reduce the number of potential locations, not to mention political obstacles through country borders. If, therefore, the inter-beam interference cannot be kept at sufficiently low level, the feeder link budgets will be deteriorated, which again prevents the linear capacity increase.

The advent of multibeam satellites has turned the satellite channel for the first time into an interference limited channel, a property held in common with the wireless channels of terrestrial cellular systems. The challenge in the design of future HTS systems is, therefore, to find appropriate strategies that handle this interference. While this field of research is fairly new for satellite systems, numerous solutions exist from the terrestrial mobile network design, and they are already integral part of terrestrial wireless standards such as Long Term Evolution (LTE). They basically rely on a joint processing of the signals and an allocation management of time-frequency physical resource blocks such as inter-cell interference coordination. The applicability of such techniques to satellite networks is the subject of current research, e.g. in [CCZ+12] and the references therein.

Since the users are usually not connected, a joint processing can only be performed either in the satellite, which is subject to signal processing capabilities in the payload, or in the gateways, assuming a backbone connectivity. In the forward link from the gateways to the user terminals, a precoding of the signals aims to precancel the interference [VPNC+16, GCO12, JVPN16]. Different precoding strategies exist ranging from very complex non-linear methods like Dirty Paper Coding [WSS06] to sub-optimal linear but easy to implement methods like zero forcing (ZF) precoding [YG06, ADMPN12]. In the return link, i.e. from the user terminals to the gateways, a joint postprocessing aims to cancel out the interference between the multiple signal streams. Examples are equalization based on non-linear minimum mean square error (MMSE) filtering [Kam08] followed by successive interference cancellation (SIC) [CCZ+12] or the joint decoding [Wyn94].

In this work, the potentials of using the spatial dimension as a further physical resource besides time, frequency and polarization is investigated to cope with the interference in the satellite channel as well as to address the data rate requirements in future HTS applications. Using the space as a further dimension requires multiple spatially distributed antennas at each side of the link, a concept which is well-known as multiple-input multiple-output (MIMO).

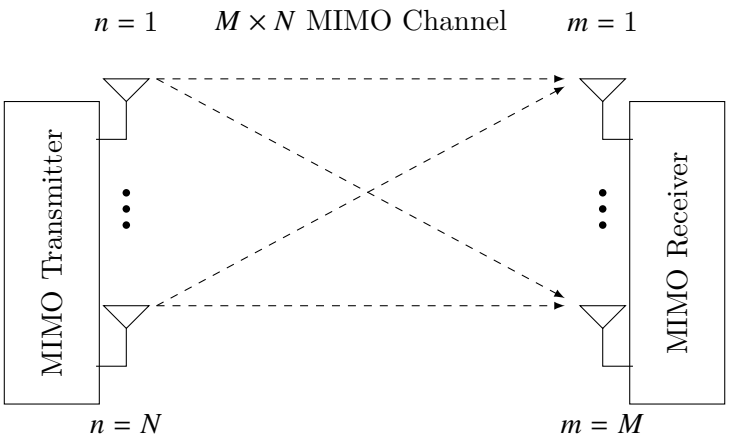

Figure 1.2.: The principle of a MIMO system with N transmit antennas and M receive antennas resulting in an $M \times N$ MIMO system.

1.2. Introduction to MIMO

1.2.1. Gains and Potentials of MIMO to HTS Networks

The term MIMO is widely used in the literature for all systems utilizing multiple transmit and receive antennas. The principle is depicted in Figure 1.2, in which the so-called $M \times N$ MIMO channel is formed between N transmit and M receive antennas. All transmit signals use the same frequency spectrum and polarization and add up at each receive antenna. The spatial distribution of the $M \cdot N$ antennas offer an additional degree of freedom that can be used to realize different performance gains. In general, three fundamentally different performance gains can be distinguished as follows [IN05a, IN05b].

(1) A higher transmit *power efficiency* is achieved by transmit signal processing, also known as beamforming, resulting in an increased receive power while the total transmit power is kept constant. This increased transmit power efficiency is referred to as antenna gain. In this case the space is exploited by distributing N radiating (respectively, M receiving) elements over a larger area which constitutes the antenna aperture. The benefit is that the antenna beam can be controlled towards a wanted direction while possible interfering signals from other directions can be suppressed. Note that the maximum directivity is, however, equal to that of a single antenna with the same equivalent aperture.

(2) The *link reliability* can be increased with transmit or receive signal processing or both aiming at a reduction of receive signal fluctuations in a fading channel environment. The performance gain that can be achieved is also known as *spatial diversity gain*. This gain is realized by providing the receiver with multiple and ideally independent replicas of the transmitted signal [BCC+07].

By sending multiple copies of the same signal over different antennas the bit error probability (BEP) can be decreased resulting in an increased reliability of the data transmission. The maximum diversity gain that can be achieved is limited to the product of the number of transmit and receive antennas [LT03].

(3) The *bandwidth efficiency* is increased if the additional degree of freedom of a MIMO system is used to transmit multiple independent data streams in parallel over the same channel, i.e. at the same time using the same frequency and polarization. This gain is referred to as *spatial multiplexing gain* [FG98], and it is limited to the number of transmit or receive antennas, whatever number is smaller.

A promising benefit of MIMO for future HTS scenarios is the spatial multiplexing gain to address the data rate requirements. Under favorable channel conditions, the channel capacity can be linearly increased by $\min\{M, N\}$ compared to that of a conventional single-input single-output (SISO) system. Moreover, the interference limitation in the satellite channel can be solved by actively exploiting the interference as an information bearing signal. The superposition of the multiple signals from neighboring beams is indeed the key and a mandatory requirement to achieve a MIMO gain. Instead of trying to suppress or even completely avoid the interference by, e.g., a radio resource management like the FR4, the advantages of MIMO actually rely on the use of the signal power from the interfering signals. In this respect, applying MIMO is a completely different approach from satellite network architectures that have been proposed so far. The potentials of the spatial MIMO technology and its applicability to HTS satellite systems is the subject of this work.

The actual gain that can be achieved by MIMO strongly depends on the wireless channel. In terrestrial mobile networks, in which MIMO is already an integral part of wireless standards such as LTE, MIMO systems can usually take advantage of a large scattering environment. In this case, the channel is dominated by multipath propagation leading to statistically independent receive signals, a property that can be exploited by the MIMO receiver. On the contrary, the presence of highly directive antennas leads to predominant Line-of-Sight (LOS) components in the satellite propagation channel [KFC+00]. Due to this strong LOS component and the absence of multipath, the applicability of MIMO to high-frequency FSS scenarios has long been doubted [ALB+11].

1.2.2. Terrestrial LOS MIMO Contributions

In contrast to the widespread belief in the scientific community that multipath in the channel is a mandatory requirement to obtain high MIMO capacities, Driessen et al. [DF99] have already shown in 1999 that the *maximum MIMO channel capacity* can indeed be achieved in pure LOS channels. The fundamental prerequisite

to achieve this gain is a particular geometrical arrangement of the antennas and the physically correct modeling of the LOS signal by applying ray tracing between the transmit-receive antenna pairs. Inspired by [DF99], Gesbert et al. [GBGP02] and Haustein et al. [HK03] have analytically derived design rules for an optimal arrangement of the transmit and receive antennas in outdoor and indoor environments, respectively. Chouayakh et al. [CKL04] have shown that it is actually possible to find realistic antenna arrangements that achieve the upper capacity bound in terrestrial LOS channels. Based on channel measurements in different indoor locations, Knopp et al. [KCL05] have shown the dependence on the geometrical arrangement of the transmit and receive antennas on the channel capacity. They provided antenna array design approaches that reduce capacity variations in typical wireless local area network (WLAN) indoor environments. These results have later been extended to more general MIMO antenna array configurations by Bohagen et al. in [BOO05], [BOO07], and Sarris et al. in [SN06]. The results of extensive channel measurement campaigns by Knopp reported in [KSH+07] and [Kno08] have practically proven the significance of the antenna arrangement on the MIMO capacity in indoor LOS environments. Even in LOS channels with sparse multipath components, the geometrical arrangement of the antenna arrays remains the dominating design factor to achieve high capacity gains [KSH+07]. After almost ten years of research on terrestrial indoor and outdoor LOS MIMO channels, two key results can be summarized as follows:

(1) Particular geometrical arrangements of the transmit and receive antennas are required to obtain the maximum MIMO capacity gain. The spacing between the antennas in relation to the transmitter-receiver distance is a key design parameter.

(2) The physically correct modeling of the LOS signal component by applying the spherical wave model (SWM) [JI05] is a prerequisite to reliably forecast capacity gains [HKO+08].

1.2.3. Application of LOS MIMO to Fixed Satellite Networks

These promising results from terrestrial LOS MIMO channels have motivated the author's research on MIMO for FSS. In [SKO+08, SKL+08] the requirements for maximum-capacity MIMO channels over geostationary satellites have been investigated. As a main contribution, an analytic formula for the optimal positioning of the ground antennas in relation to the satellite antennas has been derived. Due to the large satellite-to-ground distance of around 36 000 km in GEO applications, large spacings between the antennas either on the ground or in orbit are necessary to take advantage of the maximum multiplexing gain. Feasible system design examples based on uniform linear array (ULA) arrangements for fixed services as well

as uniform circular array (UCA) arrangements for mobile services have been proposed. Based on the UCA design proposal in [SKO+08], an analytic solution for the optimal UCA arrangement on mobile platforms has later been derived in [DSKL10]. The design of an optimal MIMO uplink and downlink including transparent payloads has been discussed in [KSO+08] and [SKO+09]. It has been revealed that the antenna arrangements in both the uplink and in the downlink must be optimized simultaneously in order to achieve the maximum MIMO capacity.

The effect of atmospheric perturbations on the performance of geometrically optimized MIMO satellite links have then been analyzed in [SKL09, KSL10] showing that the capacity is not degraded by disturbances of the signal phase. By contrast, an attenuation of the signal amplitude reduces the receive signal-to-noise ratio (SNR), similar to that of an equivalent SISO system. Since large separations between the antennas on the ground were considered, the capacity gain due to MIMO is accompanied by significant diversity effects resulting in very low probabilities of simultaneous amplitude fades at all ground antennas [KSL10].

On the other hand, large separations between the antennas result in long differential propagation delays between the MIMO signals that form a single code word. This problem has been addressed in [KSL11, SKL11, SKL12], where a receiver based on a single carrier - frequency domain equalizer (SC-FDE) architecture has been proposed that is able to cope with such differential delays.

These results, showing the feasibility of MIMO to fixed satellite networks, constitute the cornerstones and provide the necessary fundamentals to achieve the gains that are promised by theory. The early publications, in particular [SKO+08, SKL+08, SKL09, SKO+09], have motivated the investigation of numerous further applications and inspired new research directions in SATCOMs in general. Some examples are listed below:

- **Physical Layer Security:** The potentials to exploit MIMO to secure satellite links on the physical layer has been analyzed in [KSL13]. By an optimal arrangement of the MIMO antennas in combination with a limited coverage of the satellite antennas, the channel capacity of the primary satellite link is considerably higher compared to that of a possible eavesdropper. Assuming the lower capacity of the eavesdropper cannot be economically compensated by, e.g., a larger antenna dish, the primary satellite link is secured on the physical layer without applying any data encryption, an idea that were patented in [KLS13].
- **Reduction of adjacent satellite interference (ASI):** As proposed in [SWK14], the benefit of MIMO can also be used to reduce the radiated power while achieving the same capacity compared to that of a SISO satellite system. This facilitates frequency coordination among satellite operators since ASI is significantly reduced.

- **Channel measurements and measurement methods:** Extensive measurement campaigns have been carried out to validate the channel model assumptions. First, the theoretical assumptions from [SKL09, KSL10] about the effect of the atmosphere on the signal phase have been verified through channel measurements in the Ku band [SHK15a, SHK15b]. Second, the analytic equation from [SKO+08] regarding the optimal geometrical antenna arrangement in MIMO satellite links were finally proven by channel measurements reported in [HSSK16, SHK16]. The results of this campaign are summarized in Section 4.5.2. They are used to validate the developed theory in this thesis. In the course of this measurement campaign, a novel passive measurement method has been developed enabling the measurement of the MIMO satellite channel without the need to occupy satellite capacity [RSC+18].
- **Applications to UHF SATCOM:** Whereas the initial results were primarily focused on FSS channels and frequency bands above 10 GHz, the general ideas have also been adopted to address the bandwidth demands in UHF SATCOM applications. In [RCB16] the application of MIMO to military UHF SATCOM has been proposed. Theoretical analysis including simulation results assuming a Rician channel model have shown significant capacity gains if the geometry between the MIMO antennas is appropriately considered. The relevance of the LOS component in the UHF satellite channel for the geometry of the antenna arrangement has later been verified through channel measurements reported in [HSK17].
- **MIMO for feeder links:** Delamotte concentrated his work on the application of spatial MIMO in the feeder link in order to support the huge amount of aggregated data rates for the user beams [DSSK18], [DK18]. On-ground and on-board signal processing approaches as well as an advanced smart diversity for MIMO-based Q/V band feeder links have also been proposed [DK19].
- **User grouping and user scheduling:** Very recent research has now started by Storek to propose first practical applications of MIMO to SATCOM in the user links of an HTS system with FFR. In [SK17] a novel user grouping algorithm, called Multiple Antenna Downlink Orthogonal Clustering (MADOC), has been developed that maximizes the system throughput while ensuring maximal fairness between the users. The proposed concept in [SK17] considers an accurate modeling of the LOS signal component and utilizes the fundamentals on the design of optimal MIMO LOS satellite channels described in [SKL+08].

1.3. Contribution of this Work

1.3.1. Summary

In this work, the potentials and benefits of using the concept of spatial MIMO in fixed satellite networks are investigated. The gains in terms of the channel capacity that can be expected with MIMO are presented. This work provides the fundamental basics to understand the key requirements for maximum-capacity MIMO satellite systems. The results enable the design of multi-antenna satellite systems that best take advantage of a spatial multiplexing gain. This work is the first of three contributions dealing with spatial MIMO over satellite. A second contribution by Thomas Delamotte will apply the basics from this work to investigate the performance of MIMO feeder links in HTS networks [DK19]. The potential of MIMO to reduce the interference in the feeder links [DSSK18] and an increased robustness against rain fades are investigated [DK18]. A third thesis by Kai-Uwe Storek will focus on the multiuser MIMO (MU-MIMO) downlink and develops a novel user grouping algorithm [SK17] taking the design rules from this work into account.

The rest of this thesis is structured as follows:

- In **Chapter 2**, the **system and channel model** is introduced.
- In **Chapter 3**, the calculation of the **MIMO channel capacity** is described, which is used as a metric to reveal the performance gains of a MIMO satellite system compared to a conventional SISO satellite system.
- **Chapter 4** constitutes the main part of this thesis. The **requirements** for a **maximum-capacity MIMO satellite system** are derived. The **basic design rules** and the practical implications on the antenna locations are presented. The performance of an optimized satellite system under realistic conditions is investigated including the impact of the antenna patterns, the satellite movements in the GEO and the atmosphere.
- In **Chapter 5**, a complete **HTS system concept** using **MIMO in the up- and the downlink** is discussed. By applying the design rules from Chapter 4, simulation results show how greatly modern SATCOM systems can take advantage of the spatial MIMO technology.
- This thesis is concluded in **Chapter 6**.

1.3.2. Conference Publications

- R. T. Schwarz, A. Knopp, D. Ogermann, C. A. Hofmann, and B. Lankl, "Optimum-capacity MIMO satellite link for fixed and mobile services," in 2008 International ITG Workshop on Smart Antennas, WSA 2008, 2008, pp. 209–216.
- R. T. Schwarz, A. Knopp, B. Lankl, D. Ogermann, and C. A. Hofmann,

"Optimum-capacity MIMO satellite broadcast system: Conceptual design for LOS channels," 2008 4th Adv. Satell. Mob. Syst. - Proceedings, ASMS 2008, pp. 66–71, Aug. 2008.

- A. Knopp, R. T. Schwarz, D. Ogermann, C. A. Hofmann, and B. Lankl, "Satellite system design examples for maximum mimo spectral efficiency in los channels," in GLOBECOM - IEEE Global Telecommunications Conference, 2008, pp. 2890–2895.
- R. T. Schwarz, A. Knopp, and B. Lankl, "The channel capacity of MIMO satellite links in a fading environment: A probabilistic analysis," in IWSSC'09 - 2009 International Workshop on Satellite and Space Communications - Conference Proceedings, 2009, pp. 78–82.
- R. T. Schwarz, A. Knopp, D. Ogermann, C. A. Hofmann, and B. Lank, "On the prospects of mimo satcom systems: The tradeoff between capacity and practical effort," in 2009 6th International Multi-Conference on Systems, Signals and Devices, SSD 2009, 2009, pp. 1–6.
- A. Knopp, R. T. Schwarz, and B. Lankl, "On the capacity degradation in broadband MIMO satellite downlinks with atmospheric impairments," IEEE Int. Conf. Commun., pp. 1–6, May 2010.
- V. Dantona, R. T. Schwarz, A. Knopp, and B. Lankl, "Uniform circular arrays: The key to optimum channel capacity in mobile MIMO satellite links," ASMS 2010 5th Adv. Satell. Multimed. Syst. Work., pp. 421–428, Sep. 2010.
- R. T. Schwarz, A. Knopp, and B. Lankl, "Performance of an SC-FDE SATCOM system in block-time-invariant orthogonal MIMO channels," GLOBECOM - IEEE Glob. Telecommun. Conf., pp. 1–6, Dec. 2011.
- A. Knopp, R. T. Schwarz, and B. Lankl, "MIMO system implementation with displaced ground antennas for broadband military SATCOM," Proc. - IEEE Mil. Commun. Conf. MILCOM, pp. 2069–2075, Nov. 2011.
- R. T. Schwarz, A. Knopp, and B. Lankl, "SC-FDE V-BLAST system concept for MIMO over satellite with antenna misalignment," Int. Multi-Conference Syst. Signals Devices, SSD 2012 - Summ. Proc., pp. 1–8, Mar. 2012.
- A. Knopp, R. T. Schwarz and B. Lankl, "Secure MIMO SATCOM Transmission," MILCOM 2013 - 2013 IEEE Military Communications Conference, San Diego, CA, 2013, pp. 284-288.
- R. T. Schwarz, S. P. Winter, and A. Knopp, "MIMO application for reduced adjacent satellite interference in SATCOM downlinks," 2014 IEEE Int. Conf. Commun. ICC 2014, pp. 3570–3575, 2014.
- R. T. Schwarz, C. A. Hofmann, K.-U. Storek, and A. Knopp, "On the Prospects of MIMO for Satellite Communications," in Proceedings of the 22th Ka and Broadband Communications Conference, 2016, pp. 1–8.
- C. Hofmann, K.-U. Storek, R. T. Schwarz, and A. Knopp, "Spatial MIMO

over satellite: A proof of concept," in 2016 IEEE International Conference on Communications (ICC), 2016, pp. 1–6.

- R. T. Schwarz, C. A. Hofmann, and A. Knopp, "Results of a MIMO Testbed with Geosynchronous Ku-Band Satellites," 20th Int. ITG Work. Smart Antennas, pp. 93–97, 2016.
- R. T. Schwarz, F. Völk, A. Knopp, C. A. Hofmann and K. Storek, "The multiple-satellite MIMO channel of narrow band vehicular communications at UHF," MILCOM 2017 - 2017 IEEE Military Communications Conference (MILCOM), Baltimore, MD, 2017, pp. 447-452.
- T. Delamotte, R. T. Schwarz, K. Storek and A. Knopp, "MIMO Feeder Links for High Throughput Satellites (Invited Paper)", WSA 2018; 22nd International ITG Workshop on Smart Antennas, Bochum, Germany, 2018, pp. 1-8.
- B. Ramamurthy, R. T. Schwarz, W. G. Cowley, G. Bolding and A. Knopp, "Passive Channel Orthogonality Measurement Technique for MIMO SATCOM," MILCOM 2018 - 2018 IEEE Military Communications Conference (MILCOM), Los Angeles, CA, 2018, pp. 1-6.
- R. T. Schwarz, and A. Knopp, "MIMO Capacity of Co-Located Satellites in Longitude Separation," 2019 IEEE International Conference on Communications (ICC), accepted paper

1.3.3. Journal Publication

- R. T. Schwarz, T. Delamotte, K.-U. Storek, and A. Knopp, "MIMO Applications for Multibeam Satellites," IEEE Trans. Broadcast., pp. 1-18, accepted for publication, 2019.
- C. A. Hofmann, R. T. Schwarz and A. Knopp, "Multisatellite UHF MIMO Channel Measurements," in IEEE Antennas and Wireless Propagation Letters, vol. 16, pp. 2481-2484, 2017.

1.3.4. Patent

- A. Knopp, B. Lankl, and R. Schwarz, "Verfahren und Einrichtung zur MIMO-Datenübertragung mit einer Höhenplattform," Patent file number DE 10 2013 000 903.0, application date 18.01.2013, date of first publication 28.11.2013.

2. Satellite Channel and System Model

2.1. MIMO Satellite System Model

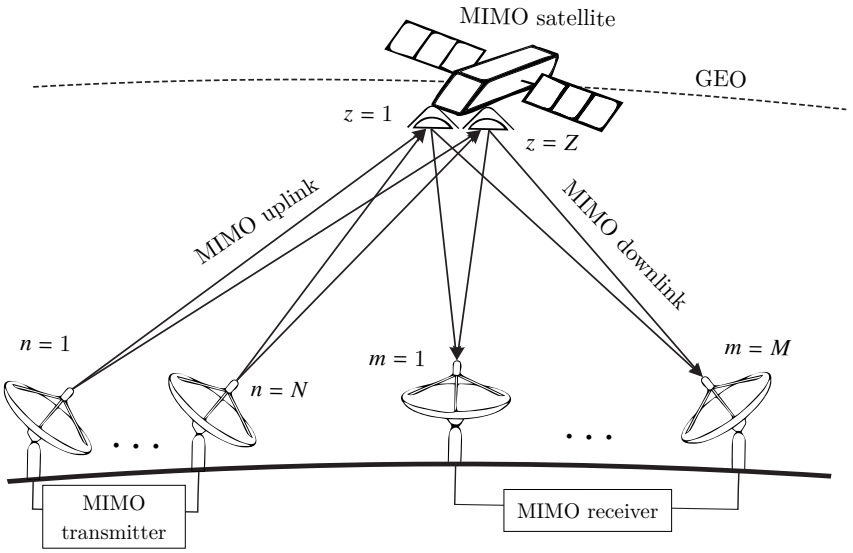

Figure 2.1.: System model comprising a transmitting ground station with N antennas, a MIMO satellite with Z transmit and receive antennas and a receiving ground station with M receive antennas forming an $M \times Z \times N$ MIMO relay system.

The following notation is based on a discrete time representation of signals of the form $x(t = kT_s) = x[k] = x$, with $k \in \mathbb{Z}, -\infty \leq k \leq \infty$. The parameter T_s denotes the sampling period and k is the time instance, which is omitted for the sake of more compact notation.

The considered system model is shown in Figure 2.1. It consists of a transmitting ground station with N transmit antennas, a geostationary MIMO satellite with Z receive and transmit antennas, and a receiving ground station with M receive antennas. The MIMO uplink and downlink channel are denoted by the matrices $\widetilde{\mathbf{H}}_{\mathrm{u}}$ and $\widetilde{\mathbf{H}}_{\mathrm{d}}$, respectively. Their entries will be detailed in Section 2.2. The satellite transfer matrix is denoted by $\mathbf{F}$, which is described in the following. The vector $\mathbf{y} = [y_1, \ldots, y_M]^{\mathrm{T}}$ contains the receive signals y_m, $1 \leq m \leq M$ at the earth station receive antennas in complex baseband notation. In the case of a transparent satellite

payload, the receive signal $\mathbf{y}$ is calculated as

$$\mathbf{y} = \widetilde{\mathbf{H}}_{\mathrm{d}}\mathbf{F} \cdot \left(\widetilde{\mathbf{H}}_{\mathrm{u}}\mathbf{x} + \boldsymbol{\eta}_{\mathrm{u}}\right) + \boldsymbol{\eta}_{\mathrm{d}} = \widetilde{\mathbf{H}}_{\mathrm{d}}\mathbf{F}\widetilde{\mathbf{H}}_{\mathrm{u}}\mathbf{x} + \widetilde{\mathbf{H}}_{\mathrm{d}}\mathbf{F}\boldsymbol{\eta}_{\mathrm{u}} + \boldsymbol{\eta}_{\mathrm{d}}. \tag{2.1}$$

The vector $\mathbf{x} = [x_1, \ldots, x_N]^{\mathrm{T}}$ contains the transmit symbols $x_n, 1 \leq n \leq N$ in complex baseband notation. The data symbols are chosen from the modulation alphabet of an arbitrary constellation $\mathbb{A}$ with the same probability of occurrence for each symbol. The spatial covariance matrix of the transmit signal vector is given by

$$\mathbf{R}_{\mathbf{x}} = \mathrm{E}\left\{\mathbf{x}\mathbf{x}^{\mathrm{H}}\right\} = P_t/N \cdot \mathbf{I}_N, \tag{2.2}$$

where $\mathrm{E}\{.\}$ denotes the expectation operator and $(.)^{\mathrm{H}}$ is the conjugate transpose of a matrix or vector. To ensure a fair comparison between MIMO and SISO systems, the total transmit power P_t on the ground is equal for both systems. Hence, P_t/N denotes the maximum equivalent isotropically radiated power (EIRP) per earth station antenna.

The vectors $\boldsymbol{\eta}_{\mathrm{u}}$ and $\boldsymbol{\eta}_{\mathrm{d}}$ denote, respectively, the additive white Gaussian noise (AWGN) contribution of the uplink and the downlink. They are given by

$$\boldsymbol{\eta}_{\mathrm{u}} = \left[\eta_{\mathrm{u},1}, \ldots, \eta_{\mathrm{u},Z}\right]^{\mathrm{T}}, \text{ and } \boldsymbol{\eta}_{\mathrm{d}} = \left[\eta_{\mathrm{d},1}, \ldots, \eta_{\mathrm{d},M}\right]^{\mathrm{T}}, \text{ respectively.}$$

Here, $\eta_{\mathrm{u},z}, 1 \leq z \leq Z$ and $\eta_{\mathrm{d},m}, 1 \leq m \leq M$ are the AWGN contributions at the z-th satellite receive antenna and the m-th earth station receive antenna, respectively. The complex noise signals are assumed to be independent and identically distributed (i.i.d.) and circular symmetric in both the uplink and the downlink. The spatial covariance matrices of the noise vectors are then given by

$$\mathbf{R}_{\boldsymbol{\eta}_{\mathrm{u}}} = \mathrm{E}\left\{\boldsymbol{\eta}_{\mathrm{u}}\boldsymbol{\eta}_{\mathrm{u}}^{\mathrm{H}}\right\} = \sigma^2_{\boldsymbol{\eta}_{\mathrm{u}}}\mathbf{I}_Z, \text{ and } \mathbf{R}_{\boldsymbol{\eta}_{\mathrm{d}}} = \mathrm{E}\left\{\boldsymbol{\eta}_{\mathrm{d}}\boldsymbol{\eta}_{\mathrm{d}}^{\mathrm{H}}\right\} = \sigma^2_{\boldsymbol{\eta}_{\mathrm{d}}}\mathbf{I}_M,$$

where identical noise power $\sigma^2_{\boldsymbol{\eta}_{\mathrm{u}}}$ at the satellite receive antennas and $\sigma^2_{\boldsymbol{\eta}_{\mathrm{d}}}$ at the earth station receive antennas is assumed.

The covariance matrix of the sum noise at the receiver

$$\boldsymbol{\eta} = \widetilde{\mathbf{H}}_{\mathrm{d}}\mathbf{F}\boldsymbol{\eta}_{\mathrm{u}} + \boldsymbol{\eta}_{\mathrm{d}} \tag{2.3}$$

is given by

$$\mathbf{R}_{\boldsymbol{\eta}} = \mathrm{E}\left\{\boldsymbol{\eta}\boldsymbol{\eta}^{\mathrm{H}}\right\} = \sigma^2_{\boldsymbol{\eta}_{\mathrm{u}}} \cdot \widetilde{\mathbf{H}}_{\mathrm{d}}\mathbf{F}\mathbf{F}^{\mathrm{H}}\widetilde{\mathbf{H}}_{\mathrm{d}}^{\mathrm{H}} + \sigma^2_{\boldsymbol{\eta}_{\mathrm{d}}} \cdot \mathbf{I}_M. \tag{2.4}$$

The matrix $\mathbf{F} \in \mathbb{C}^{Z \times Z}$ models the amplifications and phase shifts of the transparent satellite channels. Assuming no signal processing capabilities in the payload, the satellite act as a naive-amplify-and-forward (NAF) relay and $\mathbf{F}$ is given by a

diagonal matrix

$$\mathbf{F} = \operatorname{diag}\left\{a_{\mathrm{s},1}, \ldots, a_{\mathrm{s},Z}\right\},\ a_{\mathrm{s},z} = \left|a_{\mathrm{s},z}\right| / \sqrt{Z} \cdot \mathrm{e}^{-\mathrm{j}\,\upsilon_{\mathrm{s},z}},\ 1 \leq z \leq Z. \tag{2.5}$$

The parameter $\left|a_{\mathrm{s},z}\right| / \sqrt{Z} \in \mathbb{R}, \left|a_{\mathrm{s},z}\right| / \sqrt{Z} \geq 1, 1 \leq z \leq Z$ denotes the total amplitude gain of the z-th satellite channel, which includes all amplifications and losses of the signals through the channel. Moreover, the channel gains $\left|a_{\mathrm{s},z}\right|^2$ are normalized by the number of satellite channels Z in order to ensure a fair comparison between MIMO and SISO. The sum of all gains is, therefore, equal for both the MIMO satellite system and the SISO satellite system.

Note that this normalization is only used to facilitate a fair comparison between MIMO and SISO in terms of the channel capacity. In practice, the system designer would spend equally equipped satellite channels for each MIMO branch because of economical reasons and market-available hardware. State-of-the-art geostationary communications satellites are already equipped with multiple channels, but they are operated separately (e.g. one channel per beam with non-overlapping coverages). The idea of MIMO is rather to exploit the satellite channels by combining them to form a MIMO space segment while keeping the total mass and power consumption constant. This normalization of the transparent MIMO channels is, therefore, a pessimistic assumption.

In addition, since the available amplifier power per satellite payload is limited, the power constraint

$$\left[P_t / N \cdot \mathbf{F}\widetilde{\mathbf{H}}_{\mathrm{u}}\widetilde{\mathbf{H}}_{\mathrm{u}}^{\mathrm{H}}\mathbf{F}^{\mathrm{H}} + \sigma_{\boldsymbol{\eta}_{\mathrm{u}}}^2 \mathbf{F}\mathbf{F}^{\mathrm{H}}\right]_{z,z} \leq P_{\mathrm{d}}/Z,\ 1 \leq z \leq Z \tag{2.6}$$

is introduced, where P_{d}/Z denotes the maximum EIRP per satellite channel. Similar to the ground segment, also in the space segment the total downlink EIRP P_{d} is normalized by the number of satellite transmit antennas Z because the maximum allowed downlink EIRP is usually restricted by ITU frequency regulations. This normalization ensures that the sum downlink EIRP of the MIMO satellite system cannot exceed that of a SISO satellite system. The parameter $\upsilon_{\mathrm{s},z} \in [-\pi, \pi[, 1 \leq z \leq Z$ denotes the phase shift of the signals due to the transmission delays and the frequency conversions from the uplink to the downlink frequency.

Note that, in this model, the depointing losses of the satellite transmit and receive antennas as well as of the ground antennas are counted to the MIMO channel, and are, therefore, considered in the MIMO channel matrices $\widetilde{\mathbf{H}}_{\mathrm{u}} \in \mathbb{C}^{Z \times N}$ and $\widetilde{\mathbf{H}}_{\mathrm{d}} \in \mathbb{C}^{M \times Z}$. The calculation of their entries are detailed next.

2.2. MIMO Satellite Channel Model

The uplink and downlink MIMO channel transfer matrices are composed of three matrices as follows:

$$\widetilde{\mathbf{H}}_{\mathrm{u}} = \mathbf{G}_{\mathrm{u}} \odot \mathbf{H}_{\mathrm{u}} \cdot \mathbf{D}_{\mathrm{u}}, \text{ and } \widetilde{\mathbf{H}}_{\mathrm{d}} = \mathbf{D}_{\mathrm{d}} \cdot \mathbf{H}_{\mathrm{d}} \odot \mathbf{G}_{\mathrm{d}}. \tag{2.7}$$

The operator $\odot$ denotes the Hadamard product of two matrices. The matrices $\mathbf{G}_{\mathrm{u}} \in \mathbb{R}^{Z\times N}$, $\mathbf{H}_{\mathrm{u}} \in \mathbb{C}^{Z\times N}$, and $\mathbf{D}_{\mathrm{u}} \in \mathbb{C}^{N\times N}$ (respectively, $\mathbf{G}_{\mathrm{d}} \in \mathbb{R}^{M\times Z}$, $\mathbf{H}_{\mathrm{d}} \in \mathbb{C}^{M\times Z}$, and $\mathbf{D}_{\mathrm{d}} \in \mathbb{C}^{M\times M}$) model the antenna gain patterns, the free space wave propagation, and the atmospheric channel impairments of the uplink (downlink), respectively. The modeling approaches of the three parts of the channel are described in the following sections. Note that the same models are used for both the uplink and the downlink. To simplify the mathematical notation, the models are introduced for the downlink. However, all equations are equally valid for the uplink as well by appropriately changing the parameter notation.

2.2.1. Antenna Radiation Pattern

In frequency bands above 10 GHz, high-gain and directive antennas are required to close the link with high throughput. Moreover, narrow main beams with low side lobe levels are a design objective for earth station antennas operating with GEO satellites [Int03] because they effectively suppress interfering signals from and to neighboring satellite systems. Therefore, depointing losses must be considered for the case of imperfect alignment of the transmitting and receiving antennas.

The depointing losses are modeled by $\mathbf{G}_{\mathrm{d}} \in \mathbb{R}^{M\times Z}$ with the elements of $\mathbf{G}_{\mathrm{d}}$ given as

$$[\mathbf{G}_{\mathrm{d}}]_{m,z} = g_{\mathrm{d},mz} = g^{(\mathrm{E})}_{\mathrm{d},mz} \cdot g^{(\mathrm{s})}_{\mathrm{d},mz}. \tag{2.8}$$

The parameters $0 \leq g^{(\mathrm{E})}_{\mathrm{d},mz} \leq 1$ and $0 \leq g^{(\mathrm{s})}_{\mathrm{d},mz} \leq 1$ are the depointing losses from the m-th earth station antenna to the z-th satellite antenna, and from the z-th satellite antenna to the location of the m-th earth station antenna, respectively. Their values can be calculated using a normalized radiation pattern. Assuming a parabolic antenna on the ground, $g^{(\mathrm{E})}_{\mathrm{d},mz}$ can be calculated as [ST12, Section 9.5, p. 390]

$$g^{(\mathrm{E})}_{\mathrm{d},mz} = \frac{(n_{\mathrm{dr}}+1)(1-T_{\mathrm{e}})}{(n_{\mathrm{dr}}+1)(1-T_{\mathrm{e}})+T_{\mathrm{e}}} \cdot \left(2\frac{J_1(u_{mz})}{u_{mz}} + 2^{n_{\mathrm{dr}}+1} n_{\mathrm{dr}}! \frac{T_{\mathrm{e}}}{1-T_{\mathrm{e}}} \frac{J_{n_{\mathrm{dr}}+1}(u_{mz})}{u_{mz}^{n_{\mathrm{dr}}+1}} \right), \tag{2.9}$$

where $J_1(u_{mz})$ and $J_{n_{\mathrm{dr}}+1}(u_{mz})$ are the Bessel functions of first kind and order One

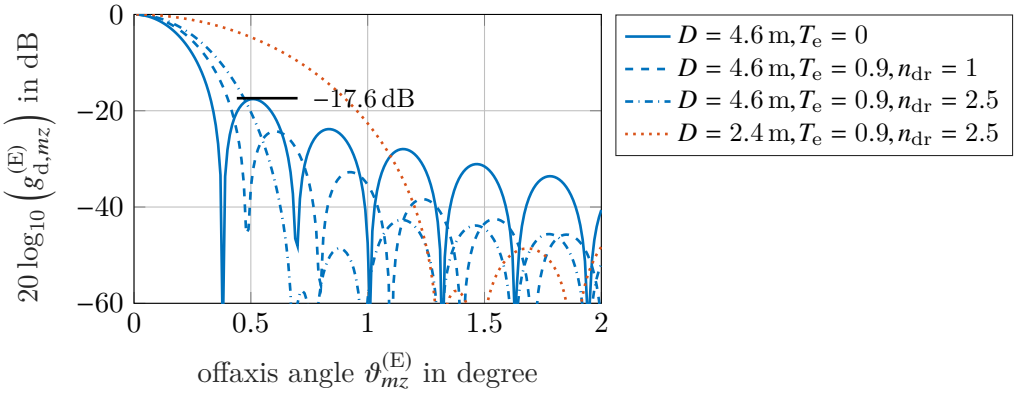

Figure 2.2.: Normalized antenna power pattern at $f = 12\,\mathrm{GHz}$ for various edge taper and field decreasing rates and two different antenna diameter.

and $n_\mathrm{dr} + 1$, respectively. The argument u_{mz} is given as

$$u_{mz} = \pi D/\lambda_\mathrm{d} \cdot \sin \vartheta^{(\mathrm{E})}_{mz},$$

with $\vartheta^{(\mathrm{E})}_{mz}$ being the off-axis angle from point of boresight of the m-th earth station antenna towards the location of the z-th satellite antenna. Parameter D and λ_d are the aperture diameter and the carrier wavelength of the downlink, respectively. Furthermore, T_e denotes the aperture edge taper, which specifies the power of the electric field at the edge of the aperture relative to the power of the electric field at the center of the aperture. If $T_\mathrm{e} = 0$, the amplitude of the electric field is uniformly distributed over the entire aperture. The parameter n_dr denotes the field decreasing rate and controls the rate at which the aperture field decreases with $\vartheta^{(\mathrm{E})}_{mz}$. The effect of T_e and n_dr on the pattern is shown in Figure 2.2.

Two diameter of 4.6 m and 2.4 m have been simulated at a carrier frequency of 12 GHz. The uniform aperture field pattern, i.e. the pattern for $T_\mathrm{e} = 0$, shows the narrowest main beam. Note that for uniform illumination of the reflector, the field decreasing rate n_dr has no effect, and, thus, (2.9) simplifies to $gmz = 2J_1(u_{mz})/u_{mz}$. A higher value of T_e increases the beamwidth of the main lobe and lowers the aperture efficiency but reduces significantly the side lobe level. The same applies for the parameter n_dr. For the same T_e, higher field decreasing rates lead to lower illumination efficiencies and broader main lobes but also to lower sidelobe levels. For $T_\mathrm{e} = 0.9$ and $n_\mathrm{dr} = 2.5$ the mainlobe is almost twice as broad as that for a uniform aperture field. However, the sidelobes are reduced to below the −40 dB level, whereas for the uniform aperture field the first side lobe is only 17.6 dB below the main lobe. Typical values for parabolic reflectors are $T_\mathrm{e} = 0.9$ and $n_\mathrm{dr} = 2.5$ [Col85], which are used in the simulations of this work. The same model is applied

for both the earth station antennas and the satellite antennas.

2.2.2. Free Space LOS Channel Model

Relying on directional antennas, it is assumed that any multipath contributions are suppressed by the radiation patterns [MB09, chapter 5.7.2.6, page 208]. The considered uplink and downlink satellite channel can, therefore, be described using a deterministic LOS model based on the free space wave propagation. Hence $\mathbf{H}_\mathrm{u}$ and $\mathbf{H}_\mathrm{d}$ contain all the $Z \cdot N$ complex channel coefficients of the uplink and the $M \cdot Z$ complex channel coefficients of the downlink, respectively. Using the parameter notation for the downlink, the LOS channel coefficient $h_{\mathrm{d},mz}$ between the z-th satellite transmit antenna and the m-th earth station receive antenna in the equivalent baseband notation is given by

$$h_{\mathrm{d},mz} = a_{\mathrm{d},mz} \cdot \mathrm{e}^{-\mathrm{j}\frac{2\pi}{\lambda_\mathrm{d}} r_{\mathrm{d},mz}} \approx a_\mathrm{d} \cdot \mathrm{e}^{-\mathrm{j}\frac{2\pi}{\lambda_\mathrm{d}} r_{\mathrm{d},mz}}. \tag{2.10}$$

The parameter $\lambda_\mathrm{d} = c_0/f_\mathrm{d}$ denotes the wavelength of the carrier with frequency f_d, and c_0 is the speed of light. The parameter

$$a_{\mathrm{d},mz} = \lambda_\mathrm{d}/\left(4\pi r_{\mathrm{d},mz}\right) \cdot \mathrm{e}^{\mathrm{j}\varphi_\mathrm{d}} \tag{2.11}$$

models the free space gain. The parameter φ_d stands for the common carrier phase and can be assumed to be zero without loss of generality (w.l.o.g.) The parameter $r_{\mathrm{d},mz}$, with $35\,786\,\mathrm{km} \leq r_{\mathrm{d},mz} \leq 41\,679\,\mathrm{km}$ $\forall m, z$, denotes the distance between the z-th satellite transmit antenna and the m-th earth station receive antenna. On the right hand side of (2.10), the approximation

$$a_{\mathrm{d},mz} \approx a_\mathrm{d} = \lambda_\mathrm{d}/(4\pi\bar{r}_\mathrm{d})\,, \text{ with } \bar{r}_\mathrm{d} = 1/(MZ) \cdot \sum_{m=1}^{M}\sum_{z=1}^{Z} r_{\mathrm{d},mz} \tag{2.12}$$

has been applied. This is reasonable because the difference between the path lengths is very small compared to their mean total length. To give an example, assume that one earth station antenna is located at the sub-satellite point while a second earth station antenna has a relative distance of 9° in geographical longitude to the first earth station antenna (corresponds to a distance of approximately 1000 km)! The resulting distances from the earth stations to the satellite are 35 786.1 km for the first receive antenna, and 35 878.5 km for the second receive antenna. Using these values, the relative error can be calculated as $(35\,878.5\,\mathrm{km} - 35\,786.1\,\mathrm{km})/35\,878.5\,\mathrm{km} \approx 2.6 \times 10^{-3}$. The corresponding error in the magnitude of the amplitude is $10\log_{10}(35\,878.5\,\mathrm{km}/35\,786.1\,\mathrm{km}) \approx 0.01\,\mathrm{dB}$, which can be neglected in the following analysis.

It is important to note that ray tracing through the parameter $r_{\mathrm{d},mz}$ has been applied to exactly determine the phase entries of $\mathbf{H}_{\mathrm{d}}$. In fact, the correct modeling of the phase difference among the signals impinging at the receive antennas is the key for the full understanding of MIMO satellite channels [DF99]. The spherical nature of the wave propagation must be taken into account [BOO09], which is ensured in (2.10) using the exact path lengths $r_{\mathrm{d},mz}$ for each LOS ray. Incorporating the signal phase into the modeling and design approach is referred as the spherical wave model (SWM) in the literature and stands in contrast to the plane wave model (PWM), which assumes no relevant phase differences between the entries of $\mathbf{H}_{\mathrm{d}}$ [JI05]. The application of the plane wave model (PWM) has become common practice for large distances between transmitter and receiver and narrow antenna spacing. The PWM assumes that there is no relevant phase difference between impinging waves at two sensors. However, in the shown basic example as well as in many practical situations, the PWM would lead to a severe underestimation of the MIMO channel capacity [JI05]. As shown in the following, the application of the SWM is a fundamental prerequisite to correctly forecast the capacity provided by a MIMO satellite system and to derive the relevant design criteria for its capacity optimization. This will be detailed in the next chapter.

2.2.3. Atmospheric Impairments

2.2.3.1. Relevant Atmospheric Impairments

Any electromagnetic (EM) wave traveling from the earth station to the geostationary satellite and vice-versa must pass through various regions at different altitudes of the atmosphere. Two regions of the atmosphere are of further interest for Earth-to-space paths [All11]:

a) The *troposphere* is the lowest portion of the Earth's atmosphere, which extends from the ground up to approximately 20 km in altitude.

b) The *ionosphere* extends from about 10 km to roughly 400 km and is characterized by various layers that are designated as D, E and F regions.

The effects of the troposphere and the ionosphere on the parameters of the EM waves are strongly dependent on the frequency. While generally ionospheric effects tend to become less significant when the frequency of the wave increases, the impairments of the troposphere become more severe. For frequencies above about 3 GHz the ionosphere is essentially transparent to space communications and the ionospheric impairments for frequencies of 10 GHz or higher become negligible. As the discussion in this work is focused on FSS applications and frequency bands above 10 GHz, it is sufficient to concentrate on the tropospheric impairments.

In these frequency bands, the main radiowave propagation impairments include attenuation effects as well as phase disturbances [All11]. The attenuation distortions comprise gaseous absorption (water vapor and oxygen), cloud and rain attenuation along with scintillations. Among these effects, rain attenuation is the most severe impact factor and can lead to losses of greater than 10 dB, especially in the higher frequency bands such as the Q/V band [SRGdP15]. The other tropospheric attenuation effects can usually be neglected [Ipp08]. In addition to the amplitude distortions, phase disturbances have to be considered, entailed by refraction and random scattering [All11].

2.2.3.2. Modeling Atmospheric Channel Impairments

Any atmospheric impairment can be modeled by an additional amplitude and phase coefficient. Identical amplitude and phase disturbances in the troposphere can be assumed for those LOS paths ending or starting at the same earth station antenna. This assumption is based on the fact that the horizontal separation in the troposphere of two LOS paths is usually less than one centimeter, as the following example shows. Because of $r_{\mathrm{d},m1} \approx r_{\mathrm{d},m2} = r_{\mathrm{d},0}\,\forall m$, the horizontal separation d_{h} of the two rays $r_{\mathrm{d},m1}$ and $r_{\mathrm{d},m2}$ at an altitude of h_{a} can be estimated by

$$d_{\mathrm{h}} \approx h_{\mathrm{a}} \cos^{-1}\left(1 - 0.5 d_{\mathrm{s}}^2 / \left(r_{\mathrm{d},0}\right)^2\right),$$

assuming that $h_{\mathrm{a}} \ll r_{\mathrm{d},0}$. The parameter d_{s} denotes the antenna spacing at the satellite in the geostationary orbit. With an antenna separation of, for example, $d_{\mathrm{s}} = 6\,\mathrm{m}$ on the satellite and a maximum altitude of severe weather influences at $h_{\mathrm{a}} = 20\,\mathrm{km}$, the resulting horizontal separation of the rays $r_{\mathrm{d},m1}$ and $r_{\mathrm{d},m2}$ is $d_{\mathrm{h}} < 0.34\,\mathrm{cm}$. Hence, it is reasonable to assume identical amplitude and phase disturbances in the troposphere for all LOS paths ending or starting at the same earth station antenna. This assumption has been verified through channel measurements. The results are summarized in Section 4.7.

The atmospheric channel impairments can then be modeled by a diagonal matrix

$$\mathbf{D}_{\mathrm{d}} = \mathrm{diag}\left\{\varsigma_{\mathrm{d},1}, \ldots, \varsigma_{\mathrm{d},M}\right\}, \tag{2.13}$$

with $\varsigma_{\mathrm{d},m}$ being the atmospheric impairment for the signals at the m-th earth station antenna. It is calculated as

$$\varsigma_{\mathrm{d},m} = \left|\varsigma_{\mathrm{d},m}\right| \cdot \mathrm{e}^{-\mathrm{j}\,\xi_{\mathrm{d},m}}, \tag{2.14}$$

where $\left|\varsigma_{\mathrm{d},m}\right| \in [0,1]$ and $\xi_{\mathrm{d},m} \in [-\pi, \pi[$ represent the additional amplitude attenuation and the phase shift, respectively.

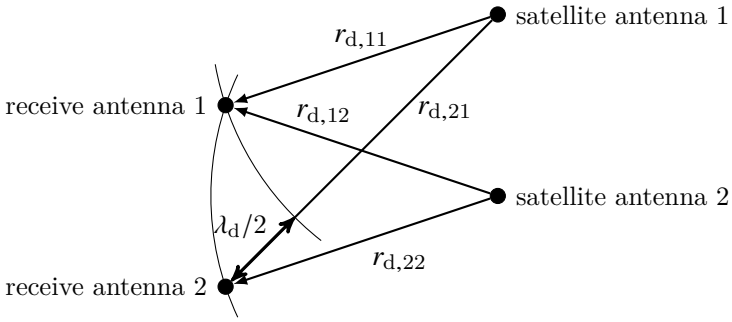

Figure 2.3.: Antenna arrangement according to the basic example.

2.2.4. Summary

As already mentioned, the same models are used for both the MIMO uplink and the MIMO downlink. Hence, equations (2.8) to (2.14) are equally valid by appropriately choosing the uplink parameter notation to calculate the matrix entries of $\mathbf{G}_{\mathrm{u}}$, $\mathbf{H}_{\mathrm{u}}$, and $\mathbf{D}_{\mathrm{u}}$. Applying (2.9), (2.10) and (2.14) to (2.7), the entry on the z-th row and the n-th column of $\widetilde{\mathbf{H}}_{\mathrm{u}}$ and the entry on the m-th row and the z-th column of $\widetilde{\mathbf{H}}_{\mathrm{d}}$ are, therefore, given as

$$\left[\widetilde{\mathbf{H}}_{\mathrm{u}}\right]_{z,n} = g_{\mathrm{u},zn}\left|\varsigma_{\mathrm{u},n}\right| a_{\mathrm{u}} \cdot \mathrm{e}^{-\mathrm{j}\frac{2\pi}{\lambda_{\mathrm{u}}} r_{\mathrm{u},zn}} \cdot \mathrm{e}^{-\mathrm{j}\xi_{\mathrm{u},n}}, \text{ and} \tag{2.15}$$

$$\left[\widetilde{\mathbf{H}}_{\mathrm{d}}\right]_{m,z} = g_{\mathrm{d},mz}\left|\varsigma_{\mathrm{d},m}\right| a_{\mathrm{d}} \cdot \mathrm{e}^{-\mathrm{j}\frac{2\pi}{\lambda_{\mathrm{d}}} r_{\mathrm{d},mz}} \cdot \mathrm{e}^{-\mathrm{j}\xi_{\mathrm{d},m}}, \text{ respectively.} \tag{2.16}$$

The ability of a MIMO system to realize the potential gains depends on the properties of the channel. The channel determines how the multiple transmit signals superimpose at the receive antennas. In the following, a basic example is introduced to illustrate how maximum MIMO gains can be obtained in LOS satellite channels. The example exhibits the ruling design parameters. The fundamental ideas of this example will be extended to a concise mathematical model in Chapter 4.

2.3. Basic Example with Maximum MIMO Gain

Consider a 2×2 downlink in which a single-satellite is the MIMO transmitter, the earth station is the MIMO receiver, and the uplink is neglected. For the sake of simplicity in this example, let the path loss a_{d} be equal to One and assume that $\mathbf{G}_{\mathrm{d}} = \mathbf{1}$ and $\mathbf{D}_{\mathrm{d}} = \mathbf{I}_2$. The receive signal vector is then given by

$$\mathbf{y} = \mathbf{H}_{\mathrm{d}}\mathbf{x} + \boldsymbol{\eta}_{\mathrm{d}},$$

with $\mathbf{x} = [x_1, x_2]^{\mathrm{T}}$ and $\boldsymbol{\eta}_{\mathrm{d}} = \left[\eta_{\mathrm{d},1}, \eta_{\mathrm{d},2}\right]^{\mathrm{T}}$.

Now assume that the first receive antenna is exactly located at the sub-satellite point. The two LOS signals radiated by the first and second satellite antenna propagate along the two paths $r_{\mathrm{d},11}$ and $r_{\mathrm{d},12}$. These paths are equal (see Figure 2.3 for an illustration of the antenna arrangement). As a consequence, the first receive antenna obtains an exact phase coherent sum of the two transmit symbols x_1 and x_2. The phase component of each transmit symbol at the receive antenna is determined by the path lengths related to the wavelength λ_{d}, where $\exp\left\{-\mathrm{j}\,2\pi/\lambda_{\mathrm{d}} \cdot r_{\mathrm{d},11}\right\} = \exp\left\{-\mathrm{j}\,2\pi/\lambda_{\mathrm{d}} \cdot r_{\mathrm{d},12}\right\} = 1$ is assumed w.l.o.g.. The propagation paths between satellite antenna one and two and the second receive antenna instead exhibit a difference in length so that a phase offset of $\exp\{-\mathrm{j}\,\pi\}$ results between the impinging EM waves. To obtain this particular phase difference, the second earth station antenna is displaced from the first earth station antenna accordingly. Assume that $\exp\left\{-\mathrm{j}\,2\pi/\lambda_{\mathrm{d}} \cdot r_{\mathrm{d},21}\right\} = 1$ and $\exp\left\{-\mathrm{j}\,2\pi/\lambda_{\mathrm{d}} \cdot r_{\mathrm{d},22}\right\} = -1$. The receive signals at the respective earth station antennas are then given by

$$\begin{aligned} y_1 &= x_1 + x_2 + \eta_{\mathrm{d},1}, \text{ and} \\ y_2 &= x_1 + \mathrm{e}^{-\mathrm{j}\,\pi} x_2 + \eta_{\mathrm{d},2} = x_1 - x_2 + \eta_{\mathrm{d},2}. \end{aligned} \tag{2.17}$$

It is obvious that two noisy estimates of the transmit symbols can be recovered at the receiver using a simple linear filter of the form $\mathbf{H}_{\mathrm{d}}^{-1}$, i.e.

$$\begin{aligned} \hat{x}_1 &= 1/2\,(y_1 + y_2) = x_1 + 1/2\,\left(\eta_{\mathrm{d},1} + \eta_{\mathrm{d},2}\right) \\ \hat{x}_2 &= 1/2\,(y_1 - y_2) = x_2 + 1/2\,\left(\eta_{\mathrm{d},1} - \eta_{\mathrm{d},2}\right) \end{aligned} \tag{2.18}$$

In this example, the receiver exploits the property of a matrix $\mathbf{H}_{\mathrm{d}}$ having orthogonal column and row vectors. In this case, the receiver is able to perfectly recover the two (noisy) transmit signals in (2.18) without any remaining signal interference. In addition, the inverse of the channel can be computed via the complex conjugate transpose of the channel matrix, which significantly simplifies the necessary calculation steps in a digital receiver. Orthogonal column and row vectors of $\mathbf{H}_{\mathrm{d}}$ are indeed the optimal situation, which will be explained by means of the channel capacity in Chapter 3. As a result, the throughput has been doubled by transmitting two symbols within the same channel. This very basic example indicates that the maximum multiplexing gain in pure LOS channels can be achieved. It has also shown that a minimum spacing of the antenna elements on Earth in relation to the antenna spacing at the satellite is required for maximum MIMO gains. The correct modeling and adjustment of the signal phase is crucial. The phase information of the channel will be used in Chapter 4 to derive practical requirements for the optimal positioning of the MIMO antennas in GEO satellite systems.

3. MIMO Channel Capacity

The channel capacity C_B is defined as the maximum data rate that can be *quasi-error-free* transmitted over the channel [Sha48]. The spectral efficiency C is the channel capacity C_B normalized by the considered system bandwidth B_w and is, therefore, measured in bit/s/Hz. Since a particular system bandwidth is not regarded and, in addition, the MIMO satellite channel for FSS was identified as frequency flat (see Chapter 2), both metrics are used in the same manner for the rest of this thesis. The channel capacity will be used as a metric to assess the feasibility of the MIMO satellite channel for FSS.

3.1. Capacity of a MIMO Satellite System

3.1.1. Naive-Amplify-and-Forward: No Channel State Information at the Satellite

Since the downlink matrix $\widetilde{\mathbf{H}}_\mathrm{d}$ in the system model (2.1) can be composed of arbitrary complex numbers and has not necessarily orthogonal column or row vectors, the total noise term $\boldsymbol{\eta}$ in (2.3) can be spatially correlated resulting in a non-diagonal covariance matrix $\mathbf{R}_{\boldsymbol{\eta}}$. However, by applying the noise whitening matrix $\mathbf{R}_{\boldsymbol{\eta}}^{-1/2}$ to both sides of (2.1), an equivalent system is obtained where the channel matrix is $\mathbf{R}_{\boldsymbol{\eta}}^{-1/2}\widetilde{\mathbf{H}}_\mathrm{d}\mathbf{F}\widetilde{\mathbf{H}}_\mathrm{u}$ and the noise is white Gaussian [TH07]. The instantaneous MIMO channel capacity without channel knowledge at the transmitter and the satellite is then given as [TH07][2]

$$C = \log_2\left(\det\left(\mathbf{I}_N + P_t/N \cdot \left(\mathbf{R}_{\boldsymbol{\eta}}^{-1/2}\widetilde{\mathbf{H}}_\mathrm{d}\mathbf{F}\widetilde{\mathbf{H}}_\mathrm{u}\right)^\mathrm{H}\mathbf{R}_{\boldsymbol{\eta}}^{-1/2}\widetilde{\mathbf{H}}_\mathrm{d}\mathbf{F}\widetilde{\mathbf{H}}_\mathrm{u}\right)\right). \tag{3.1}$$

Without channel state information (CSI) at the transmitter, the available transmit power P_t is equally distributed over all earth station antennas, i.e. the EIRP is equal for all transmit antennas. In addition, without CSI at the satellite, $\mathbf{F}$ is a diagonal weighting matrix with entries $a_{\mathrm{s},z} = a_\mathrm{s}\ \forall z$ on the main-diagonal.[3] This

[2] Note that usually a constant factor 1/2 is considered in front of the logarithm due to the fact that the signal is actually transmitted in two time instances (first time slot for the uplink data transmission, second time slot for the downlink transmission). Since this constant factor has no effect on the optimal design of the MIMO channel and the following analysis, it is ignored for the rest of this work.

[3] Note that the values of a_s are still subject to the downlink power constraint (2.6).

type of satellite payload is referred as NAF relay in the following. Using (2.4) in (3.1) and applying the matrix inverse lemma $(\mathbf{I}-\mathbf{AB})^{-1} = \mathbf{I}+\mathbf{A}(\mathbf{I}-\mathbf{BA})^{-1}\mathbf{B}$ [Lüt96, 3.5.2, p. 29] together with the commutative property of the determinant $\det(\mathbf{I}+\mathbf{AB}) = \det(\mathbf{I}+\mathbf{BA})$, (3.1) can be rewritten as [TH07]

$$C = \log_2\left(\det\left(\mathbf{I}_Z + \frac{P_t/N}{\sigma^2_{\boldsymbol{\eta}_\mathrm{u}}}\widetilde{\mathbf{H}}_\mathrm{u}\widetilde{\mathbf{H}}_\mathrm{u}^\mathrm{H} - \frac{P_t/N}{\sigma^2_{\boldsymbol{\eta}_\mathrm{u}}}\widetilde{\mathbf{H}}_\mathrm{u}\widetilde{\mathbf{H}}_\mathrm{u}^\mathrm{H}\mathbf{S}^{-1}\right)\right), \tag{3.2}$$

with the matrix $\mathbf{S}$ given by $\mathbf{S} = \left(\mathbf{I}_Z + \sigma^2_{\boldsymbol{\eta}_\mathrm{u}}/\sigma^2_{\boldsymbol{\eta}_\mathrm{d}} \cdot \mathbf{F}^\mathrm{H}\widetilde{\mathbf{H}}_\mathrm{d}^\mathrm{H}\widetilde{\mathbf{H}}_\mathrm{d}\mathbf{F}\right)$.

3.1.2. Smart-Amplify-and-Forward: Decomposition Into Parallel Sub-Channels

To illustrate the dependence of the channel capacity on the properties of the uplink and the downlink channel, the MIMO channels $\widetilde{\mathbf{H}}_\mathrm{u}$ and $\widetilde{\mathbf{H}}_\mathrm{d}$ are decomposed into parallel sub-channels, so-called eigenmodes, using their singular value decompositions (SVDs)

$$\widetilde{\mathbf{H}}_\mathrm{u} = \mathbf{U}_\mathrm{u}\boldsymbol{\Gamma}_\mathrm{u}^{1/2}\mathbf{V}_\mathrm{u}^\mathrm{H}, \text{ and } \widetilde{\mathbf{H}}_\mathrm{d} = \mathbf{U}_\mathrm{d}\boldsymbol{\Gamma}_\mathrm{d}^{1/2}\mathbf{V}_\mathrm{d}^\mathrm{H}. \tag{3.3}$$

To simplify notation, the parameters

$$W_\mathrm{u} = \min\{Z,N\},\ W_\mathrm{d} = \min\{M,Z\}, \text{ and } W = \min\{M,Z,N\}, \text{ as well as}$$
$$V_\mathrm{u} = \max\{Z,N\},\ V_\mathrm{d} = \max\{M,Z\}, \text{ and } V = \max\{M,Z,N\}$$

are introduced. The matrices $\mathbf{U}_\mathrm{u} \in \mathbb{C}^{Z\times Z}$ (respectively, $\mathbf{U}_\mathrm{d} \in \mathbb{C}^{M\times M}$) and $\mathbf{V}_\mathrm{u} \in \mathbb{C}^{N\times N}$ ($\mathbf{V}_\mathrm{d} \in \mathbb{C}^{Z\times Z}$) are both unitary. The columns of $\mathbf{U}_\mathrm{u}$ ($\mathbf{U}_\mathrm{d}$) and the columns of $\mathbf{V}_\mathrm{u}$ ($\mathbf{V}_\mathrm{d}$) are called the left-singular vectors and the right-singular vectors, respectively. They constitute an orthonormal basis of the row and the column spaces of the channel matrices. Moreover, $\boldsymbol{\Gamma}_\mathrm{u}^{1/2}$ and $\boldsymbol{\Gamma}_\mathrm{d}^{1/2}$ are rectangular diagonal matrices with W_u non-negative singular values $\sqrt{\gamma_{\mathrm{u},1}} \leq \ldots \leq \sqrt{\gamma_{\mathrm{u},W_\mathrm{u}}}$ of $\widetilde{\mathbf{H}}_\mathrm{u}$ and with W_d non-negative singular values $\sqrt{\gamma_{\mathrm{d},1}} \leq \ldots \leq \sqrt{\gamma_{\mathrm{d},W_\mathrm{d}}}$ of $\widetilde{\mathbf{H}}_\mathrm{d}$ on the main diagonals, respectively. Using these decompositions, and assuming full CSI at the satellite such that the satellite transfer matrix can be of the form

$$\widetilde{\mathbf{F}} = \mathbf{V}_\mathrm{d}\mathbf{F}\mathbf{U}_\mathrm{u}^\mathrm{H}, \tag{3.4}$$

the receive signal vector at the receiving earth station is then given as

$$\tilde{\mathbf{y}} = \boldsymbol{\Gamma}_\mathrm{d}^{1/2}\mathbf{F}\boldsymbol{\Gamma}_\mathrm{u}^{1/2}\tilde{\mathbf{x}} + \boldsymbol{\Gamma}_\mathrm{d}^{1/2}\mathbf{F}\tilde{\boldsymbol{\eta}}_\mathrm{u} + \tilde{\boldsymbol{\eta}}_\mathrm{d}, \tag{3.5}$$

where $\tilde{\mathbf{y}} = \mathbf{U}_{\mathrm{d}}^{\mathrm{H}}\mathbf{y}$, $\tilde{\mathbf{x}} = \mathbf{V}_{\mathrm{u}}^{\mathrm{H}}\mathbf{x}$, $\tilde{\boldsymbol{\eta}}_{\mathrm{u}} = \mathbf{U}_{\mathrm{u}}^{\mathrm{H}}\boldsymbol{\eta}_{\mathrm{u}}$, and $\tilde{\boldsymbol{\eta}}_{\mathrm{d}} = \mathbf{U}_{\mathrm{d}}^{\mathrm{H}}\boldsymbol{\eta}_{\mathrm{d}}$. The MIMO relay system in (2.1) is transformed into W parallel and non-interfering SISO systems. Note that the unitary matrices $\mathbf{V}_{\mathrm{u}}$, $\mathbf{U}_{\mathrm{u}}$ and $\mathbf{U}_{\mathrm{d}}$ do not change the statistics of $\mathbf{x}$, $\boldsymbol{\eta}_{\mathrm{u}}$ and $\boldsymbol{\eta}_{\mathrm{d}}$, respectively, i.e. $\mathrm{E}\left\{\tilde{\mathbf{x}}\tilde{\mathbf{x}}^{\mathrm{H}}\right\} = P_t/N \cdot \mathbf{I}_N$, $\mathrm{E}\left\{\tilde{\boldsymbol{\eta}}_{\mathrm{u}}\tilde{\boldsymbol{\eta}}_{\mathrm{u}}^{\mathrm{H}}\right\} = \sigma_{\boldsymbol{\eta}_{\mathrm{u}}}^2\mathbf{I}_Z$, and $\mathrm{E}\left\{\tilde{\boldsymbol{\eta}}_{\mathrm{d}}\tilde{\boldsymbol{\eta}}_{\mathrm{d}}^{\mathrm{H}}\right\} = \sigma_{\boldsymbol{\eta}_{\mathrm{d}}}^2\mathbf{I}_M$.

The channel capacity of this system in (3.5) is easily calculated by the sum over all parallel sub-channels, i.e.

$$C = \sum_{w=1}^{W} \log_2\left(1 + \frac{P_t/N}{\gamma_{\mathrm{d},w}\left|a_{\mathrm{s},w}\right|^2/Z \cdot \sigma_{\boldsymbol{\eta}_{\mathrm{u}}}^2 + \sigma_{\boldsymbol{\eta}_{\mathrm{d}}}^2} \cdot \gamma_{\mathrm{d},w}\left|a_{\mathrm{s},w}\right|^2/Z \cdot \gamma_{\mathrm{u},w}\right), \tag{3.6}$$

where $\gamma_{\mathrm{u},w}$ and $\gamma_{\mathrm{d},w}$ are the eigenvalues of $\widetilde{\mathbf{H}}_{\mathrm{u}}\widetilde{\mathbf{H}}_{\mathrm{u}}^{\mathrm{H}}$ and $\widetilde{\mathbf{H}}_{\mathrm{d}}\widetilde{\mathbf{H}}_{\mathrm{d}}^{\mathrm{H}}$, respectively. They equal the square of the singular values of $\widetilde{\mathbf{H}}_{\mathrm{u}}$ and $\widetilde{\mathbf{H}}_{\mathrm{d}}$. Since $\widetilde{\mathbf{H}}_{\mathrm{u}}\widetilde{\mathbf{H}}_{\mathrm{u}}^{\mathrm{H}}$ and $\widetilde{\mathbf{H}}_{\mathrm{d}}\widetilde{\mathbf{H}}_{\mathrm{d}}^{\mathrm{H}}$ are positive semi-definite, the eigenvalues are in the range of

$$\begin{aligned}
0 \le \gamma_{\mathrm{u},w} \le \sum_{w=1}^{W_{\mathrm{u}}} \gamma_{\mathrm{u},w} &= \mathrm{tr}\left\{\widetilde{\mathbf{H}}_{\mathrm{u}}\widetilde{\mathbf{H}}_{\mathrm{u}}^{\mathrm{H}}\right\}, 1 \le w \le W_{\mathrm{u}}, \text{ and} \\
0 \le \gamma_{\mathrm{d},w} \le \sum_{w=1}^{W_{\mathrm{d}}} \gamma_{\mathrm{d},w} &= \mathrm{tr}\left\{\widetilde{\mathbf{H}}_{\mathrm{d}}\widetilde{\mathbf{H}}_{\mathrm{d}}^{\mathrm{H}}\right\}, 1 \le w \le W_{\mathrm{d}}, \text{ respectively.}
\end{aligned}$$

The magnitudes of $\gamma_{\mathrm{u},w}$ and of $\gamma_{\mathrm{d},w}$ represent the uplink and downlink channel gains (which are smaller than one) of the w-th equivalent SISO channel and determine directly the receive power. With the introduced channel model in (2.15) and (2.16), it follows that the sums of all channel gains are upper bounded by

$$\begin{aligned}
\mathrm{tr}\left\{\widetilde{\mathbf{H}}_{\mathrm{u}}\widetilde{\mathbf{H}}_{\mathrm{u}}^{\mathrm{H}}\right\} &= |a_{\mathrm{u}}|^2 \sum_{z=1}^{Z}\sum_{n=1}^{N}\left|g_{\mathrm{u},zn}\right|^2\left|\varsigma_{\mathrm{u},n}\right|^2 \le |a_{\mathrm{u}}|^2 ZN = |a_{\mathrm{u}}|^2 W_{\mathrm{u}}V_{\mathrm{u}}, \text{ and} \\
\mathrm{tr}\left\{\widetilde{\mathbf{H}}_{\mathrm{d}}\widetilde{\mathbf{H}}_{\mathrm{d}}^{\mathrm{H}}\right\} &= |a_{\mathrm{d}}|^2 \sum_{m=1}^{M}\sum_{z=1}^{Z}\left|g_{\mathrm{d},mz}\right|^2\left|\varsigma_{\mathrm{d},m}\right|^2 \le |a_{\mathrm{d}}|^2 MZ = |a_{\mathrm{d}}|^2 W_{\mathrm{d}}V_{\mathrm{d}}.
\end{aligned} \tag{3.7}$$

Hence, the values of $\gamma_{\mathrm{u},w}$ and $\gamma_{\mathrm{d},w}$ are constrained by depointing losses and atmospheric attenuations in addition to the free space path losses. Under ideal conditions, all antennas must be perfectly aligned ($\mathbf{G}_{\mathrm{u}} = \mathbf{1}$, and $\mathbf{G}_{\mathrm{d}} = \mathbf{1}$) and the atmosphere shows no additional attenuation ($\mathbf{D}_{\mathrm{u}} = \mathbf{I}_N$, $\mathbf{D}_{\mathrm{d}} = \mathbf{I}_M$). The magnitudes of $\gamma_{\mathrm{u},w}$ and $\gamma_{\mathrm{d},w}$ are then maximized, i.e. equality in (3.7) is achieved.

Recall that CSI of the up- and downlink must be available at the satellite to allow a linear processing in the payload and to decompose the system into W parallel subchannels. This operation can be considered as a matched filter along the singular vectors of the uplink and downlink channel matrices. The relay processing matrix $\widetilde{\mathbf{F}}$ according to (3.4) has been shown to be the optimal matrix which maximizes the

channel capacity for arbitrary $\widetilde{\mathbf{H}}_{\mathrm{u}}$ and $\widetilde{\mathbf{H}}_{\mathrm{d}}$ [TH07]. This type of satellite payload is termed smart-amplify-and-forward (SAF) relay in the following. The multiplication of the receive signals with $\widetilde{\mathbf{F}}$ requires signal processing capabilities in the payloads because $\widetilde{\mathbf{F}}$ is not necessarily a diagonal matrix. The implications on the payload design are later discussed in Section 3.1.3.3.

3.1.3. MIMO Capacity Upper Bound

In the following, the particular channel condition is derived that maximizes (3.6). To this end, (3.6) is rewritten as

$$C = \log_2\left(\prod_{w=1}^{W}\left(1 + \frac{P_t/N}{\gamma_{\mathrm{u},w}^{-1}\sigma_{\boldsymbol{\eta}_{\mathrm{u}}}^2 + \left(\gamma_{\mathrm{u},w}\left|a_{\mathrm{s},w}\right|^2/Z\cdot\gamma_{\mathrm{d},w}\right)^{-1}\sigma_{\boldsymbol{\eta}_{\mathrm{d}}}^2}\right)\right). \tag{3.8}$$

Using the downlink power constraint (2.6), the maximum allowed payload gains are calculated as

$$\left|a_{\mathrm{s},w}\right|^2/Z = P_{\mathrm{d}}/Z\cdot\left(P_t/N\cdot\gamma_{\mathrm{u},w} + \sigma_{\boldsymbol{\eta}_{\mathrm{u}}}^2\right)^{-1},\ \forall w. \tag{3.9}$$

This ensures that the sum EIRP in the downlink does not exceed a certain limit P_{d} while simultaneously the amplification in the payloads is maximized. Using (3.9) in (3.8) it follows for the channel capacity that

$$C = \log_2\left(\prod_{w=1}^{W}\left(1 + \left(\frac{N\sigma_{\boldsymbol{\eta}_{\mathrm{u}}}^2}{P_t\gamma_{\mathrm{u},w}} + \frac{Z\sigma_{\boldsymbol{\eta}_{\mathrm{d}}}^2}{P_{\mathrm{d}}\gamma_{\mathrm{d},w}}\cdot\left(1 + \frac{N\sigma_{\boldsymbol{\eta}_{\mathrm{u}}}^2}{P_t\gamma_{\mathrm{u},w}}\right)\right)^{-1}\right)\right). \tag{3.10}$$

Defining additionally

$$\rho_{\mathrm{u}} = P_t/\sigma_{\boldsymbol{\eta}_{\mathrm{u}}}^2,\ \text{and}\ \rho_{\mathrm{d}} = P_{\mathrm{d}}/\sigma_{\boldsymbol{\eta}_{\mathrm{d}}}^2 \tag{3.11}$$

as the (linear) ratios of the total radiated transmit power P_t and P_{d} to the noise powers per receive antenna of the uplink and the downlink, respectively, the MIMO capacity is calculated as

$$C = \log_2\left(\prod_{w=1}^{W}\left(1 + \left(\frac{N}{\rho_{\mathrm{u}}\gamma_{\mathrm{u},w}} + \frac{Z}{\rho_{\mathrm{d}}\gamma_{\mathrm{d},w}}\cdot\left(1 + \frac{N}{\rho_{\mathrm{u}}\gamma_{\mathrm{u},w}}\right)\right)^{-1}\right)\right). \tag{3.12}$$

Equation (3.12) shows the well-known reciprocal sum of the uplink receive SNR $\rho_{\mathrm{u}}/N\cdot\gamma_{\mathrm{u},w}$ and the downlink receive SNR $\rho_{\mathrm{d}}/Z\cdot\gamma_{\mathrm{d},w}$ of a transparent satellite link. The total receive SNR of the w-th MIMO sub-channel is maximum if both the uplink and the downlink receive SNRs are equal, but it can never be larger than the minimum of both. The third term in (3.12) is a result of the downlink power constraint (3.9). The amplification $\left|a_{\mathrm{s},z}\right|^2/Z$ in the z-th payload is additionally

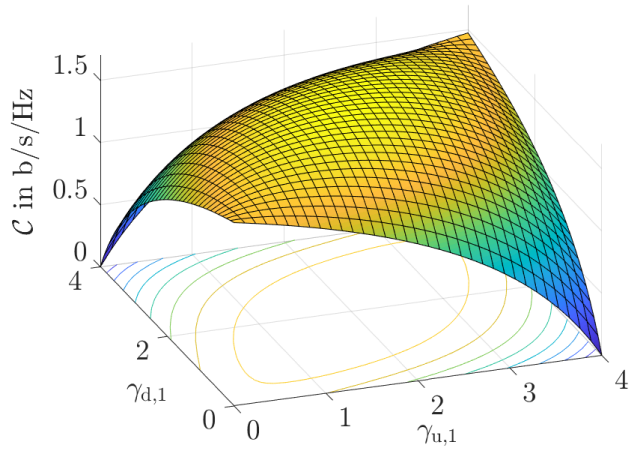

Figure 3.1.: C for the case $M = Z = N = 2$ as a function of the eigenvalues $0 \leq \gamma_{\mathrm{u},1} \leq \gamma_{\mathrm{u},1} + \gamma_{\mathrm{u},2} = 4$ and $0 \leq \gamma_{\mathrm{d},1} \leq \gamma_{\mathrm{d},1} + \gamma_{\mathrm{d},2} = 4$, $\rho_{\mathrm{u}} = \rho_{\mathrm{d}} = 2$

scaled by the uplink noise power $\sigma^2_{\boldsymbol{\eta}_{\mathrm{u}}}$ due to the fact that $\boldsymbol{\eta}_{\mathrm{u}}$ effectively contributes to the downlink EIRP. As a consequence, the downlink SNR is reduced by the factor of $1/\left(1 + N/\left(\rho_{\mathrm{u}}\gamma_{\mathrm{u},w}\right)\right)$. This effect vanishes for large SNRs but it cannot be ignored if ρ_{u} and ρ_{d} are small.

3.1.3.1. Full Multiplexing System: Equal Antenna Numbers

The case $M = Z = N$ is considered first, which is denoted as Full Multiplexing System (FMS) in the following. The FMS constitutes the most economical configuration in terms of required hardware (number of antennas) related to bandwidth efficiency. Since the logarithm is a monotonically increasing function, C is maximized by maximizing the product of the W non-negative terms in (3.12). Maximizing (3.12) is a parametrized optimization problem and can be formulated as

$$\begin{aligned} \max_{\gamma_{\mathrm{u},n},\gamma_{\mathrm{d},n}} \quad & \prod_{n=1}^{N} \left(1 + \left(\frac{N}{\rho_{\mathrm{u}}\gamma_{\mathrm{u},n}} + \frac{N}{\rho_{\mathrm{d}}\gamma_{\mathrm{d},n}} \cdot \left(1 + \frac{N}{\rho_{\mathrm{u}}\gamma_{\mathrm{u},n}}\right)\right)^{-1}\right) \\ \text{s.t.} \quad & 0 \leq \gamma_{\mathrm{u},n} \leq |a_{\mathrm{u}}|^2 N^2 \\ & 0 \leq \gamma_{\mathrm{d},n} \leq |a_{\mathrm{d}}|^2 N^2. \end{aligned} \tag{3.13}$$

To get a first estimate of the location of a maximum, Figure 3.1 shows a surface plot of C based on the parameter setup $M = Z = N = 2$, $0 \leq \gamma_{\mathrm{u},1} \leq \gamma_{\mathrm{u},1} + \gamma_{\mathrm{u},2} = 4$, $0 \leq \gamma_{\mathrm{d},1} \leq \gamma_{\mathrm{d},1} + \gamma_{\mathrm{d},2} = 4$, and $\rho_{\mathrm{u}} = \rho_{\mathrm{d}} = 2$.

The surface shows an apparent maximum at the value pair $\gamma_{\mathrm{u},1} = 2$, $\gamma_{\mathrm{d},1} = 2$. The second eigenvalues of the uplink and downlink must then also be $\gamma_{\mathrm{u},2} = 2$,

and $\gamma_{\mathrm{d},2} = 2$, respectively. A detailed derivation of the maximum of (3.13) is given in Appendix A. The approach is based on solving the gradient vector of (3.13) with respect to the uplink and downlink eigenvalues. The result shows that equal eigenvalues in the uplink and simultaneously equal eigenvalues in the downlink maximizes (3.13).

Since $\sum_{n=1}^{N} \gamma_{\mathrm{u},n} \leq |a_{\mathrm{u}}|^2 N^2$ and $\sum_{n=1}^{N} \gamma_{\mathrm{d},n} \leq |a_{\mathrm{d}}|^2 N^2$, the optimal eigenvalue profile must therefore be $\gamma_{\mathrm{u},n} = \gamma_{\mathrm{u}} \leq N |a_{\mathrm{u}}|^2, \ \forall n$ and $\gamma_{\mathrm{d},n} = \gamma_{\mathrm{d}} \leq N |a_{\mathrm{d}}|^2, \ \forall n$. The maximum channel capacity of the FMS is then given by

$$C_{\mathrm{opt}} = N \log_2 \left(1 + \left(\frac{N}{\rho_{\mathrm{u}} \gamma_{\mathrm{u}}} + \frac{N}{\rho_{\mathrm{d}} \gamma_{\mathrm{d}}} \cdot \left(1 + \frac{N}{\rho_{\mathrm{u}} \gamma_{\mathrm{u}}} \right) \right)^{-1} \right) \tag{3.14a}$$

$$\leq N \log_2 \left(1 + \left(\frac{1}{\rho_{\mathrm{u}} |a_{\mathrm{u}}|^2} + \frac{1}{\rho_{\mathrm{d}} |a_{\mathrm{d}}|^2} \cdot \left(1 + \frac{1}{\rho_{\mathrm{u}} |a_{\mathrm{u}}|^2} \right) \right)^{-1} \right). \tag{3.14b}$$

The value of (3.14b) is only achieved for ideal channel conditions, i.e. perfect alignment of all MIMO antennas and no additional attenuations in the atmosphere. The total SNR at the receiving ground station is then given as

$$\rho_r = \left(\frac{1}{\rho_{\mathrm{u}} |a_{\mathrm{u}}|^2} + \frac{1}{\rho_{\mathrm{d}} |a_{\mathrm{d}}|^2} \cdot \left(1 + \frac{1}{\rho_{\mathrm{u}} |a_{\mathrm{u}}|^2} \right) \right)^{-1}. \tag{3.15}$$

It is equal for each sub-channel because all sub-channels are equally strong.

3.1.3.2. Different Numbers of Antennas in Up- and Downlink

The solution in (3.14) was derived for the FMS, i.e. a system with $M = Z = N$ antennas, which maximizes the multiplexing gain by minimizing the required hardware effort. However, there might be practical scenarios in which unequal numbers of antennas are necessary. A multi-user downlink of an HTS system, for example, usually serves much more users than satellite beams are available. To this end, asymmetric satellite systems in terms of antenna numbers is discussed next. The following systems are defined.

Ground Diversity System: Asymmetric System with $M \times W \times N$ Antennas The number of earth station antennas of the Ground Diversity System (GDS) is larger than the number of satellite antennas, i.e. $W < M, N$. The maximum number of non-zero eigenvalues equals W for both the uplink and the downlink. Therefore, the optimal solution is still achieved for equally strong eigenvalues in the uplink and the downlink. Applying $Z = W$ to (3.7), the optimal eigenvalue profile is $\gamma_{\mathrm{u}} \leq N |a_{\mathrm{u}}|^2, \ \forall w$ and $\gamma_{\mathrm{d}} \leq M |a_{\mathrm{d}}|^2, \ \forall w$. The maximum channel capacity of the

GDS is then bounded by

$$C_{\text{opt}} \leq W \log_2 \left(1 + \left(\frac{1}{\rho_{\text{u}} \left| a_{\text{u}} \right|^2} + \frac{W}{\rho_{\text{d}} M \left| a_{\text{d}} \right|^2} \cdot \left(1 + \frac{1}{\rho_{\text{u}} \left| a_{\text{u}} \right|^2} \right) \right)^{-1} \right). \tag{3.16}$$

As already shown in (3.6), the number of parallel sub-channels and, therefore, the maximum multiplexing gain is limited to $W = \min\{M, Z, N\}$. One or more additional antennas on the ground cannot increase the multiplexing gain. However, an additional earth station receive antenna increases the downlink SNR by a factor of $(1 + 1/M)$, which is a diversity gain. An additional transmit antenna instead has no effect on the uplink SNR because the EIRP is normalized by the number of antennas to ensure a fixed sum EIRP P_t.

Satellite Diversity System: Asymmetric System with $W \times Z \times W$ Antennas In the Satellite Diversity System (SDS) the number of satellite antennas is larger than the number of earth station antennas. The number of transmit and receive antennas on the ground is equal, i.e. $Z > W, M = N$. Since the number of non-zero eigenvalues in the SDS is still the same in the uplink and the downlink, the optimal solution is again equally strong eigenvalues in the up- and downlink. Applying $N = W$ and $M = W$ to (3.7), the maximum channel capacity of the SDS is

$$C_{\text{opt}} \leq W \log_2 \left(1 + \left(\frac{W}{\rho_{\text{u}} Z \left| a_{\text{u}} \right|^2} + \frac{1}{\rho_{\text{d}} \left| a_{\text{d}} \right|^2} \cdot \left(1 + \frac{W}{\rho_{\text{u}} Z \left| a_{\text{u}} \right|^2} \right) \right)^{-1} \right). \tag{3.17}$$

An additional antenna in the space segment increases the uplink SNR by a factor of $(1 + 1/Z)$. The downlink SNR remains constant as the EIRP per satellite transmit antenna has been normalized by Z.

Ground and Satellite Diversity System: Asymmetric System with $M \geq Z > N$ or $M < Z \leq N$ Antennas This system is termed Ground and Satellite Diversity System (GSDS). The number of non-zero eigenvalues differs between the uplink and the downlink ($W_{\text{u}} > W_{\text{d}}$ or $W_{\text{u}} < W_{\text{d}}$). Although theoretically possible, such a scenario has only limited practical relevance, because only the first W non-zero singular values in $\mathbf{\Gamma}_{\text{u}}^{1/2}$ and in $\mathbf{\Gamma}_{\text{d}}^{1/2}$ are exploited. If $M < Z \leq N$, the last $W_{\text{u}} - W$ non-zero singular of the uplink, and if $M \geq Z > N$, the last $W_{\text{d}} - W$ non-zero singular values of the downlink cannot be used. The optimal solution that maximizes (3.12) would be to distribute the channel gains from the $W_{\text{u}} - W$ (respectively, $W_{\text{d}} - W$) unused uplink (downlink) eigenvalues as much as possible to the remaining W eigenvalues of the channel. Although the capacity is slightly increased due to an increased SNR compared to that of W_{u} and W_{d} equally strong eigenvalues, the respective

channel matrix would no longer be composed of orthogonal columns/rows. As a consequence, the W signal streams spatially interfere in the channel and the computational complexity is increased since non-orthogonal matrices must be handled in the receiver. In addition, the optimal relay matrix $\widetilde{\mathbf{F}}$ becomes non-diagonal, which additionally increases the computational effort in the payload as shown next. The preferred solution is, therefore, also in this case to design satellite channels with equally strong eigenvalues in the uplink and the downlink.

3.1.3.3. Summary and Implications on the Payload Design

Combining the results of (3.14), (3.16) and (3.17), the maximum channel capacity of a transparent MIMO satellite system is ultimately bounded by

$$C_{\text{opt}} \leq W \log_2 \left(1 + \left(\frac{N}{\rho_{\text{u}} V_{\text{u}} \left| a_{\text{u}} \right|^2} + \frac{Z}{\rho_{\text{d}} V_{\text{d}} \left| a_{\text{d}} \right|^2} \cdot \left(1 + \frac{N}{\rho_{\text{u}} V_{\text{u}} \left| a_{\text{u}} \right|^2} \right) \right)^{-1} \right). \tag{3.18}$$

Equation (3.18) constitutes the capacity upper bound of an $M \times Z \times N$ transparent satellite system where both the up- and downlink channels have W non-zero eigenvalues. As long as W eigenvalues of the uplink *and* W eigenvalues of the downlink are equal, the channel capacity is maximized according to (3.18), and $\widetilde{\mathbf{H}}_{\text{u}}$ as well as $\widetilde{\mathbf{H}}_{\text{d}}$ are called *optimal MIMO channels*. For the GDS (respectively, the SDS), all row (column) vectors of $\widetilde{\mathbf{H}}_{\text{u}}$, and all column (row) vectors of $\widetilde{\mathbf{H}}_{\text{d}}$ are then pairwise orthogonal and have equal norm. In the case of the FMS ($Z = N$ and $M = Z$), $\widetilde{\mathbf{H}}_{\text{u}}$ and $\widetilde{\mathbf{H}}_{\text{d}}$ are scaled unitary matrices having orthogonal row *and* column vectors, i.e. $\widetilde{\mathbf{H}}_{\text{u}} \widetilde{\mathbf{H}}_{\text{u}}^{\text{H}} = \widetilde{\mathbf{H}}_{\text{u}}^{\text{H}} \widetilde{\mathbf{H}}_{\text{u}} = N \left| a_{\text{u}} \right|^2 \mathbf{I}_N$ and $\widetilde{\mathbf{H}}_{\text{d}} \widetilde{\mathbf{H}}_{\text{d}}^{\text{H}} = \widetilde{\mathbf{H}}_{\text{d}}^{\text{H}} \widetilde{\mathbf{H}}_{\text{d}} = M \left| a_{\text{d}} \right|^2 \mathbf{I}_M$.

Note that for an FMS and for a GDS, the optimal relay matrix $\widetilde{\mathbf{F}}$ defined in (3.4) simplifies to the diagonal matrix $\mathbf{F}$ if $\widetilde{\mathbf{H}}_{\text{u}}$ has orthogonal row vectors and $\widetilde{\mathbf{H}}_{\text{d}}$ has orthogonal column vectors. In this case, $\mathbf{V}_{\text{d}}$ and $\mathbf{U}_{\text{u}}$ can then be both identity matrices because we get $\widetilde{\mathbf{H}}_{\text{u}} \widetilde{\mathbf{H}}_{\text{u}}^{\text{H}} = \mathbf{\Gamma}_{\text{u}}$ and $\widetilde{\mathbf{H}}_{\text{d}}^{\text{H}} \widetilde{\mathbf{H}}_{\text{d}} = \mathbf{\Gamma}_{\text{d}}$. The capacity of an optimal naive-amplify-and-forward (NAF) satellite system equals then the capacity of optimal smart-amplify-and-forward (SAF) satellite system. The computational effort in the payload is reduced. This benefit cannot be used by the SDS because orthogonal row and column spaces of $\widetilde{\mathbf{H}}_{\text{u}}$ and $\widetilde{\mathbf{H}}_{\text{d}}$, respectively, can only be achieved if the number of satellite antennas Z is equal or less than the number of ground station antennas N and M. If $Z > N$ or $Z > M$, signal processing capabilities must be available in the space segment to achieve the channel capacity in (3.6), irrespective of the orthogonality of the rows of $\widetilde{\mathbf{H}}_{\text{u}}$ and the columns of $\widetilde{\mathbf{H}}_{\text{d}}$.

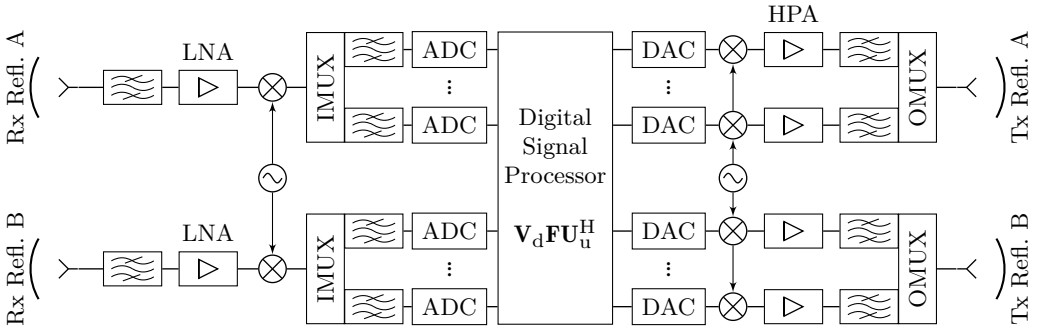

Figure 3.2.: Block diagram of a Low-Level Matched Filter (LLMF) digital transparent payload implementing the smart-amplify-and-forward (SAF) relay concept (example with $Z = 2$ MIMO branches).

The property of equal norm of all rows in $\widetilde{\mathbf{H}}_\mathrm{u}$ and all columns in $\widetilde{\mathbf{H}}_\mathrm{d}$ can always be achieved in an optimal LOS satellite channel since all the coefficients have nearly identical magnitude, but it can be lost if weather impairments and depointing losses are introduced.[4] Even with optimized pure LOS channels providing (on average) equally strong eigenvalues, occasional fades of the signal amplitudes due to weather effects cannot be avoided. The implementation of a digital signal processor (DSP) in the payload is, therefore, generally advised so that $\mathbf{V}_\mathrm{d}$ and $\mathbf{U}_\mathrm{u}^\mathrm{H}$ can be adapted and always optimal MIMO relaying according to (3.4) is achieved.

The necessary CSI can be obtained using existing channel sounding methods. One solution consists in the transmission of training signals like the constant amplitude zero autocorrelation (CAZAC) sequence [BC02]. Applying the method as described in [HSSK16], the phase and amplitude information of the channel coefficients can then be estimated via a cyclic cross-correlation of the receive signal with the known training sequence. Based on this information, the matrices $\mathbf{V}_\mathrm{d}$ and $\mathbf{U}_\mathrm{u}^\mathrm{H}$ can be computed (e.g. in a central processing unit on the ground) and transmitted to the satellite. Since the tropospheric attenuation changes slowly, the update rate of $\mathbf{V}_\mathrm{d}$ and $\mathbf{U}_\mathrm{u}^\mathrm{H}$ can be low (multiple seconds or even minutes). Obtaining this CSI to realize modem features such as Uplink Power Control (UPC) is already common practice. As long as the pure LOS up- and downlink channels are optimal, the additional effort (computational complexity, update rate of CSI) to compensate weather effects and antenna depointing is manageable.

A proposal of a MIMO payload is provided in Figure 3.2 showing the main building blocks with $Z = 2$ receive and transmit antennas. The core component is an

[4] The degrading effect of antenna depointing and weather impairments on the optimal MIMO capacity will be discussed in the next chapter.

on-board DSP[5] that allows matrix operations on wideband signals to implement the SAF relay concept, i.e. the optimal relaying matrix $\widetilde{\mathbf{F}}$ according to (3.4) [TH07]. After the input section, the signals are down-converted to an Intermediate Frequency (IF) and channelized through the Input Multiplexer (IMUX) section. The analog-to-digital converters (ADCs) and digital-to-analog converters (DACs) perform direct sampling and conversion from IF to baseband. In the analog part of the transmitting chain the signals are converted from the IF to the downlink frequency, amplified and combined through the Output Multiplexer (OMUX) section.

In the DSP the receive signals are first matched to the left singular vectors of the uplink matrix $\widetilde{\mathbf{H}}_\mathrm{u}$, weighted through the diagonal matrix $\mathbf{F}$, and then matched to the right singular vectors of $\widetilde{\mathbf{H}}_\mathrm{d}$ before the analog signals are amplified through the high power amplifiers (HPAs). This type of payload is called Low-Level Matched Filter (LLMF) payload because the matching of the transmit signals to $\widetilde{\mathbf{H}}_\mathrm{d}$ is performed prior to amplification. Note that the multiplication of the signals with $\mathbf{U}_\mathrm{u}^\mathrm{H}$ and $\mathbf{V}_\mathrm{d}$ potentially increases the peak-to-average power ratio (PAPR), an issue which is known and subject of current research for MIMO systems relaying on precoding [GYW16, MSD18].

As already briefly introduced in the basic example in Section 2.3, the benefit of optimal MIMO channels emphasizes again the significance of the channel properties to the design of a MIMO satellite system. Here, it has been shown in addition that a proper MIMO satellite channel significantly reduces the complexity and necessary computational effort in the system, not only in the satellite. An optimal MIMO satellite channel requires particular antenna spacings. From a physical point of view, *channel orthogonality* leads to superimposed receive signals that can be perfectly resolved without residual interference at the receiver. The condition to obtain such satellite channels will be derived in Chapter 4.

3.1.4. MIMO Capacity Lower Bound

Consider now the example where all receive signals at each receive antenna in the uplink and the downlink are nearly phase aligned, i.e. the PWM can be applied. All path lengths are approximately equal and a simple example of the channel matrices in this case is $\widetilde{\mathbf{H}}_\mathrm{u} \approx a_\mathrm{u} \left[\begin{smallmatrix} 1 & 1 \\ 1 & 1 \end{smallmatrix}\right]$ and $\widetilde{\mathbf{H}}_\mathrm{d} \approx a_\mathrm{d} \left[\begin{smallmatrix} 1 & 1 \\ 1 & 1 \end{smallmatrix}\right]$. The received signals are equal and cannot be distinguished by the receiver. This is the so-called "keyhole channel" [JI05], which provides only one sub-channel. All eigenvalues are zero except for one that is $\gamma_{\mathrm{u},1} = \mathrm{tr}\left\{\widetilde{\mathbf{H}}_\mathrm{u}\widetilde{\mathbf{H}}_\mathrm{u}^\mathrm{H}\right\} \leq W_\mathrm{u}V_\mathrm{u}\,|a_\mathrm{u}|^2$ for the uplink and $\gamma_{\mathrm{d},1} = \mathrm{tr}\left\{\widetilde{\mathbf{H}}_\mathrm{d}\widetilde{\mathbf{H}}_\mathrm{d}^\mathrm{H}\right\} \leq$

[5] Radiation tolerant on-board processors based on Field Programmable Gate Arrays (FPGAs) or Application-Specific Integrated Circuits (ASICs) are market-available [HGF+17]. DSPs constitute the state-of-the-art in modern HTSs to realize Digital Transparent Payloads (DTPs) performing signal processing on the physical layer, such as filtering, channelization and routing, predistortion, etc.

$W_\mathrm{d} V_\mathrm{d} |a_\mathrm{d}|^2$ for the downlink. The keyhole capacity constitutes the lower bound for MIMO systems at a given SNR and is given for the pure LOS channel by

$$C_\mathrm{key} = \log_2 \left(1 + \left(\frac{N}{V_\mathrm{u} W_\mathrm{u} |a_\mathrm{u}|^2 \rho_\mathrm{u}} + \frac{Z}{V_\mathrm{d} W_\mathrm{d} |a_\mathrm{d}|^2 \rho_\mathrm{d}} \left(1 + \frac{N}{V_\mathrm{u} W_\mathrm{u} |a_\mathrm{u}|^2 \rho_\mathrm{u}} \right) \right)^{-1} \right). \quad (3.19)$$

It is interesting to note that system proposals relying on closely separated user terminals (UTs) might simplify the precoding in the gateways of a MU-MIMO scenario as discussed in [CCO15, JVPN17, GVCTM17]. However, this essentially means (almost) equal channel vectors among the users and the capacity of this system can never exceed the lower bound in (3.19). The keyhole capacity will be used for comparison purposes in the following.

3.2. Capacity of a SISO Satellite System

The channel capacity of a SISO system is given by

$$C_\mathrm{SISO} = \log_2 \left(1 + \left(|a_\mathrm{u}|^{-2} \rho_\mathrm{u}^{-1} + |a_\mathrm{d}|^{-2} \rho_\mathrm{d}^{-1} \left(1 + |a_\mathrm{u}|^{-2} \rho_\mathrm{u}^{-1} \right) \right)^{-1} \right), \quad (3.20)$$

if again the ideal pure LOS channel is assumed and depointing losses and weather effects are neglected. Comparing (3.14b) with the capacity of a SISO system, the potentials of a MIMO system in terms of a W times multiplexing gain becomes obvious. Note again that for this comparison the radiated power per transmit antenna has been scaled by the number of transmit antennas. Thus the total transmit power in the uplink and the downlink remain equal for both the SISO and the MIMO satellite system. In other words, the MIMO capacity gain comes with no additional costs in terms of transmit power and/or bandwidth.

Note that the keyhole capacity in (3.19) is still higher than the capacity of an equivalent SISO system as defined in (3.20). In fact, even though no multiplexing gain is achieved in (3.19), at least an SNR gain of $V_\mathrm{u} W_\mathrm{u} / N$ in the uplink and $V_\mathrm{d} W_\mathrm{d} / Z$ in the downlink is obtained.

3.3. Comparison

In Figure 3.3, the boundaries of the MIMO capacity of satellite systems with two, three and five antennas are compared to the SISO capacity. The x-axis shows the uplink receive SNR in decibel. All curves represent the optimal case of perfectly aligned antennas (no depointing losses) without atmospheric attenuations. The curves show the advantage of a MIMO system compared to a SISO system. The slope of C_opt is determined by $W = \min\{M, Z, N\}$. One or more additional receive

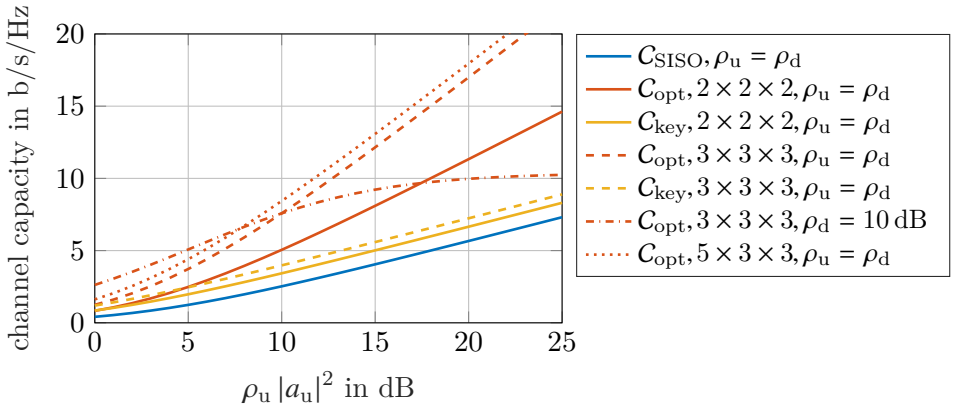

Figure 3.3.: Boundaries of the MIMO channel capacity in comparison to a SISO channel.

antenna(s) increase the downlink SNR, but the multiplexing gain remains equal (compare red dashed with red dotted curve). The slope of C_{key} equals that of C_{SISO}, even for higher antenna numbers. However, the SNR advantage of C_{key} over C_{SISO} can be clearly observed.

3.4. Summary of the Key Results

The key results of this chapter are summarized as follows:

- The upper MIMO capacity bound C_{opt} and the lower MIMO capacity bound C_{key} of a transparent MIMO satellite system are given by (3.18) and (3.19), respectively.
- The upper bound is achieved if all the eigenvalues of the uplink channel *and* all the eigenvalues of the downlink channel are equal. In this case, the uplink and downlink channels are called *optimal MIMO channels*.
- The maximum multiplexing gain is limited to $W = \min\{M, Z, N\}$, i.e. the minimum of the number of the ground antennas and the satellite antennas.
- The optimal FMS maximizes the multiplexing gain by minimizing the number of necessary antennas. The GDS and the SDS provide an additional diversity gain (SNR increase) at the cost of one or more additional antennas.
- In the case of an optimal up- and downlink channel with orthogonal rows in $\widetilde{\mathbf{H}}_u$ and orthogonal columns in $\widetilde{\mathbf{H}}_d$, no signal processing is necessary in the payload to achieve C_{opt}. The complexity reduces to a NAF architecture, an advantage that can only be used by the FMS and the GDS.
- If the signals are faded differently among the ground antennas, SAF relaying must be implemented using (3.4) to achieve C according to (3.6). In other words, $\widetilde{\mathbf{F}}$ constitutes the optimal relay matrix for arbitrary $\widetilde{\mathbf{H}}_u$ and $\widetilde{\mathbf{H}}_d$.

4. Capacity Performance of MIMO FSS Systems

It has been shown that the properties of the MIMO channel determine the achievable channel capacity. Only if both the uplink and the downlink channel are optimal (i.e. the channel matrices have equally strong singular values), the satellite system can take advantage of the maximum MIMO capacity gain. In this chapter, the requirements to obtain such an optimal MIMO satellite channel will be derived. To this end, the existing contributions from terrestrial LOS MIMO applications (see the review again provided in Section 1.2.2) will be extended to the satellite channel. It has already been indicated in Section 2.3 that the locations of the MIMO antennas are the key and particular attention must be paid to the signal phase of the LOS component. The main contribution in this chapter is an analytic formula that allows to optimally place the earth station antennas in relation to the satellite antennas such that the maximum number of parallel sub-channels is achieved (Section 4.3).

Since the uplink and the downlink channel matrices are mutually independent both must be optimized separately. The discussion starts with the downlink in Section 4.1. It will then be shown in Section 4.2 that the result can also be used to derive optimal MIMO uplinks. The implications on the positioning of the antennas are discussed in Sections 4.4 and 4.5. The achievable capacity gains under realistic conditions including the impact of satellite motion in the GEO and the impact of tropospheric disturbances are analyzed in Sections 4.6 and 4.7, respectively.

The focus will be on the FMS and the GDS, i.e. the number of ground station antennas equal or exceed the number of satellite antennas. From a practical point of view, this constitutes the most relevant case because the available space onboard a satellite (or orbital slots in the GEO) is much more restricted compared to the number of antennas that can be deployed on Earth.

4.1. Optimal MIMO Downlink Channel

4.1.1. General Criterion

As shown in Chapter 3, the MIMO downlink channel is optimal with respect to the maximum multiplexing gain if all column vectors in case of $M \geq Z$ of the channel

matrix $\widetilde{\mathbf{H}}_{\mathrm{d}}$ are pairwise orthogonal. This requirement can be formulated as[6]

$$\mathbf{h}_{\mathrm{c},k}^{\mathrm{H}}\mathbf{h}_{\mathrm{c},l} = 0,\ k,l \in \{1,\ldots,Z\},\ k > l,\ \text{if } M \geq Z, \tag{4.1}$$

where $\mathbf{h}_{\mathrm{c},k}$ denotes the k-th column vector of $\widetilde{\mathbf{H}}$.

Using (2.16) in (4.1), it follows that

$$|a|^2 \sum_{m=1}^{M} |\varsigma_m|^2 g_{mk} g_{ml} \mathrm{e}^{-\mathrm{j}\frac{2\pi}{\lambda}(r_{ml}-r_{mk})} = 0,\ k,l \in \{1,\ldots,Z\}, k > l. \tag{4.2}$$

Here, $r_{ml} - r_{mk}$ is the difference between the propagation paths from the m-th earth station antenna to the l-th satellite antenna and from the m-th earth station antenna to the k-th satellite antenna, respectively. An appropriate choice of the various distances between the transmit and receive antennas is the key to satisfy (4.2). In addition, the different weights of each of the M complex numbers in (4.2) must be regarded, which is determined by the atmospheric attenuation and the antenna depointing losses. While the free-space loss $|a|^2$ is equal for each of the M numbers in (4.2), different depointing losses and varying atmospheric attenuation lead to different absolute values (see also the discussion in Section 3.1.3.3 again).

Whereas the distances between the transmit and receive antennas as well as the antenna pointing are fixed parameters that can be controlled by the system designer, the atmospheric attenuation is random and will change over time. At this stage, it is, therefore, reasonable to assume that all antennas are perfectly aligned. Furthermore, consider the case of ideal "clear sky" conditions first such that $\widetilde{\mathbf{H}} = \mathbf{H}$ according to (2.10). The effect of antenna depointing and atmospheric disturbances will later be addressed in Sections 4.5 and 4.7, respectively. It follows that now

$$\sum_{m=1}^{M} \mathrm{e}^{-\mathrm{j}\frac{2\pi}{\lambda}(r_{ml}-r_{mk})} = 0,\ k,l \in \{1,\ldots,M\},\ k > l, \tag{4.3}$$

must be satisfied. To find a solution for (4.3), first consider the following condition:

$$\sum_{m=1}^{M} \mathrm{e}^{-\mathrm{j}\beta(m+\kappa)} = 0,\ \beta \in \mathbb{R} \setminus \{0\},\ \kappa \in \mathbb{R}. \tag{4.4}$$

The sum in (4.4) corresponds to the sum of M terms of a geometric series and can

[6] To simplify the notation in this section, the subscript d to indicate that the parameter corresponds to the downlink will be omitted.

be written as

$$\sum_{m=1}^{M} p \cdot q^m = p \cdot q \cdot \frac{1-q^M}{1-q} = 0,\ p = \mathrm{e}^{-\mathrm{j}\beta\kappa},\ q = \mathrm{e}^{-\mathrm{j}\beta}. \tag{4.5}$$

The condition (4.4) is satisfied if $1 = \mathrm{e}^{-\mathrm{j}\beta M}$ and $1 \neq \mathrm{e}^{-\mathrm{j}\beta}$. The solution that fulfills both constraints is

$$\beta = 2\pi v/M,\ v \in \mathbb{Z},\ \text{with}\ v \nmid M, \tag{4.6}$$

where $v \nmid M$ means v must not be a multiple of M. Using the substitution $\frac{2\pi}{\lambda}(r_{ml} - r_{mk}) = \beta(m+\kappa)$ in (4.4), we obtain

$$(r_{ml} - r_{mk}) = \lambda v_{kl}(m + \kappa_{kl})/M, \tag{4.7}$$

with $k,l \in \{1,\ldots,Z\}, k > l, v_{kl} \in \mathbb{Z}, v_{kl} \nmid M$ and $\kappa_{kl} \in \mathbb{R}$. Note that v_{kl} and κ_{kl} can be different for different value pairs of (k,l) because the M complex numbers in (4.3) for one particular set of (k,l) are independent of any other value pair (k',l').

Eq. (4.7) is the very general condition to obtain an optimal MIMO satellite channel with arbitrary antenna number under ideal LOS conditions. Particular differences between the individual path lengths are required so that (4.7) is satisfied. The other two system parameters are the number of antennas M and the carrier wavelength λ. As already discussed in Chapter 2, the plane wave assumption to model the wave propagation would ultimately fail since all path lengths are identical in the PWM. Note that no particular constraints with respect to the geometrical arrangement of the antennas on ground and in orbit have been assumed. Condition (4.7) does not necessarily require any particular array geometry. In order to derive practical constraints for the design of an optimal MIMO satellite link, the number of possible solutions in (4.7) is now limited as follows.

4.1.2. Downlink Channels with Two Satellite Antennas

One possibility to find a more convenient solution for (4.7) is to limit the number of the satellite antennas to two. As a consequence, the number of maximum parallel sub-channels of $\mathbf{H}$ is also limited to $W = \min\{M,Z\} = 2$. Thus, at most two out of theoretically $V = \max\{M,Z\}$ singular values of $\mathbf{H}$ are different from zero. The following derivation for $M \times 2$ satellite links has first been published in [SKO+08] starting the era of MIMO SATCOM. While it was only limited applicable to existing systems, it paved the way for a bunch of MIMO-based applications, be it in the uplink (e.g. the concept of smart gateways [DSSK18, DK18]) or in the downlink (e.g. the MU-MIMO concept [SK17]).

Since $Z = 2$, the matrix $\mathbf{H}^{\mathrm{H}}\mathbf{H}$ is a 2×2 matrix consisting of the entries $\left[\mathbf{H}^{\mathrm{H}}\mathbf{H}\right]_{1,1} =$

$\left[\mathbf{H}^{\mathrm{H}}\mathbf{H}\right]_{2,2} = |a|^2 M$ on its main diagonal. The first sub-diagonal entries are

$$\left[\mathbf{H}^{\mathrm{H}}\mathbf{H}\right]_{1,2} = \left[\mathbf{H}^{\mathrm{H}}\mathbf{H}\right]_{2,1}^{*} = |a|^2 \sum_{m=1}^{M} \exp\left\{-\mathrm{j}\, 2\pi/\lambda \cdot (r_{m2} - r_{m1})\right\},$$

which are required to be zero. In this case, the two eigenvalues of $\mathbf{H}^{\mathrm{H}}\mathbf{H}$ are $\gamma_1 = \gamma_2 = |a|^2 M$. The eigenvalues are obtained through an eigenvalue decomposition of $\mathbf{H}^{\mathrm{H}}\mathbf{H}$. Thus, the equation $\det\left(\mathbf{H}^{\mathrm{H}}\mathbf{H} - \gamma \mathbf{I}_Z\right) = 0$ has to be solved which leads to the second order polynomial

$$\gamma^2 - 2\,|a|^2 M\gamma + |a|^4 M^2 - |a|^4 \cdot \sum_{k=1}^{M}\sum_{l=1}^{M} \exp\left\{-\mathrm{j}\,\frac{2\pi}{\lambda}\left(r_{k2} - r_{k1} - (r_{l2} - r_{l1})\right)\right\} = 0, \quad (4.8)$$

and the solution

$$\gamma_{1/2} = |a|^2 M \pm |a|^2 \cdot \left(\sum_{k=1}^{M}\sum_{l=1}^{M} \exp\left\{-\mathrm{j}\,\frac{2\pi}{\lambda}\left(r_{k2} - r_{k1} - (r_{l2} - r_{l1})\right)\right\}\right)^{1/2}. \quad (4.9)$$

Recall that the MIMO channel is optimal if the two eigenvalues are equal, i.e. $\gamma_{1/2} = |a|^2 M$. Hence, the necessary condition can be expressed by

$$\sum_{k=1}^{M}\sum_{l=1}^{M} \exp\left\{-\mathrm{j}\,\frac{2\pi}{\lambda}\left(r_{k2} - r_{k1} - (r_{l2} - r_{l1})\right)\right\} = \sum_{k=1}^{M}\sum_{l=1}^{M} [\mathbf{E}]_{k,l} \stackrel{!}{=} 0. \quad (4.10)$$

Equation (4.10) describes M^2 unit complex numbers forming a matrix $\mathbf{E}$ with the following properties:

1. The main diagonal entries of $\mathbf{E}$ are 1, as in this case $k = l$.
2. $\mathbf{E}$ is Hermitian, i.e. $[\mathbf{E}]_{k,l} = [\mathbf{E}]_{l,k}^{*}$, for $k \neq l$.

For the location of these complex numbers on the unit circle, the following statements are true:

1. $[\mathbf{E}]_{k,k} = 1,\ k = 1, \ldots, M$, i.e. M out of M^2 unit complex numbers are real-valued.
2. In order to satisfy (4.10) the arguments of the remaining $M^2 - M$ unit complex numbers are the optimization parameters.

A possible arrangement of the M^2 unit complex numbers, which fulfills the condition in (4.10), is described next and illustrated for the case $M = 3$ in Figure 4.1a. Essentially, the M complex numbers forming the main diagonal of $\mathbf{E}$ are identical and equal to one. The remaining complex numbers can be equally distributed on the unit circle in M tuples of M complex numbers. Two neighboring tuples are then separated by a phase angle of $2\pi/M$ as illustrated in Figure 4.1a. Note that

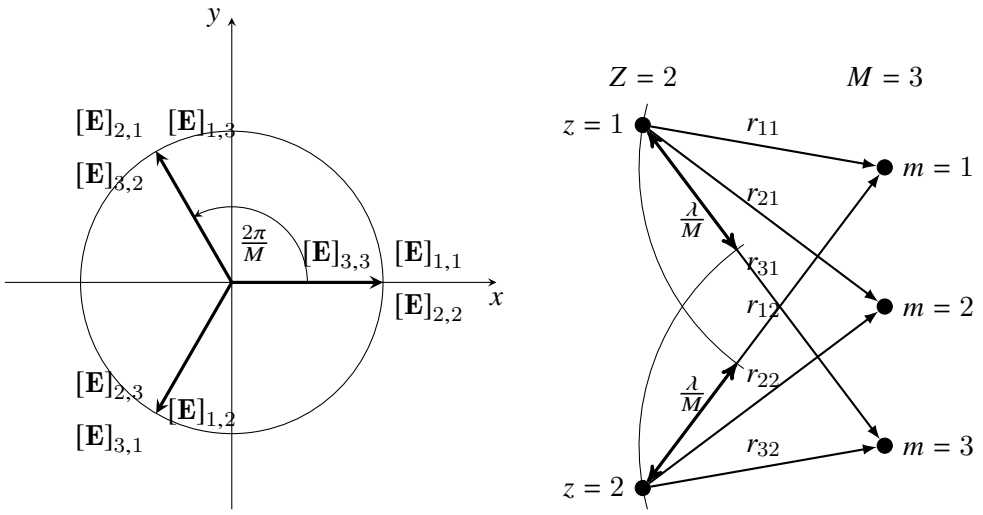

(a) Optimal phasor placement

(b) Optimal ULA configuration

Figure 4.1.: Example of an optimal distribution of the unit complex numbers in matrix $\mathbf{E}$ on the unit circle, which satisfies (4.11), and the corresponding practical solution of an optimal antenna arrangement for $M = 3$ and $Z = 2$.

for $M = 2$ and for $M = 3$ this equidistant placement of the M tuples constitutes the only possible solution that satisfies (4.10). To give an example, if $M = 2$, the unit complex numbers must be $[\mathbf{E}]_{2,1} = [\mathbf{E}]_{1,2} = -1$ because $[\mathbf{E}]_{1,1} = [\mathbf{E}]_{2,2} = 1$ and, therefore, the phase angle between both tuples has to be always $2\pi/2 = \pi$. For $M \geq 4$ the equidistant placement of the M tuples of complex numbers constitutes only one possible solution and still unlimited possibilities exist that fulfill (4.10). Following the example of Figure 4.1a showing the equal distribution of all M tuples across the unit circle, the location of the unit complex numbers on the unit circle is described by

$$\arg\left\{[\mathbf{E}]_{k,l}\right\} = v \cdot (k-l) \cdot 2\pi/M, \text{ with } k,l \in \{1,\ldots,M\},\ k > l,\ v \in \mathbb{Z},\ v \nmid M. \quad (4.11)$$

Since $\mathbf{E}$ is Hermitian, it is sufficient to consider $k > l$ because $k < l$ is equivalent and leads to the same solution. The simplification $k > l$ has already been added to (4.11). The parameter $v \in \mathbb{Z}$ is an integer and provides a further degree of freedom to place the complex numbers on the unit circle. In the example of Figure 4.1a, $v = 1$ has been chosen and, therefore, the unit complex numbers $[\mathbf{E}]_{1,3}$, $[\mathbf{E}]_{2,1}$, and $[\mathbf{E}]_{3,2}$ are all located in the second quadrant. The value $v = 2$ would also lead to a possible solution. In this case the unit complex numbers $[\mathbf{E}]_{1,3}$, $[\mathbf{E}]_{2,1}$, and $[\mathbf{E}]_{3,2}$, which are located in the second quadrant, would change their location with the unit complex numbers in the third quadrant. Note that $v = 3$ would not lead to a valid

solution because in this case all the unit complex numbers would be equal to One. In other words, v must not be a multiple of the number of earth station antennas M. This restriction is indicated by $v \nmid M$, which means that v is indivisible by M. The value of $v = M + 1 = 4$ would again lead to a valid solution. In general, all the values of $v = n \cdot M + 1, n \in \mathbb{Z}$ represent the periodicity of a valid solution in 2π.

Recall that, except for the case $M = 2$ and $M = 3$, this arrangement of the unit complex numbers is *one* possible solution only, which fulfills condition (4.10). In general, there exists an infinite number of solutions. Based on the example arrangement in Figure 4.1a and applying (4.10) in (4.11), it follows as a further generalization that

$$|r_{k2} - r_{k1} - (r_{l2} - r_{l1})| = v \cdot (k - l) \cdot \lambda / M, \tag{4.12}$$

with $k, l \in \{1, \ldots, M\}$, $k > l$, $v \in \mathbb{Z}^+$, $v \nmid M, M \geq Z = 2$. This equation allows for the calculation of a MIMO antenna setup with $Z = 2$ antennas at the transmitter and a theoretically unlimited number of M antennas at the receiver. If (4.12) is fulfilled, the eigenvalues γ_1 and γ_2 are equal, i.e. $\gamma_1 = \gamma_2 = |a|^2 M$, and $\mathbf{H}^{\mathrm{H}}\mathbf{H}$ becomes a scaled unitary matrix. In this case the desired phase angle relations within the channel matrix are obtained and, as stated before, the MIMO capacity becomes maximal.

One application example of (4.12) in the two-dimensional space is shown in Figure 4.1b for the case $M = 3$ and $v = 1$, which exactly matches the placement of the unit complex numbers on the unit circle of Figure 4.1a. The three antenna elements on the right side of Figure 4.1b are arranged within a uniform linear array (ULA), which means that all neighboring antennas have equidistant spacing and are placed on a virtual line. The antenna arrangement and the resulting path lengths in this example are such that

$$r_{11} = r_{32},\ r_{21} = r_{22}, \text{ and } r_{31} = r_{12}.$$

For $v = 1$, it follows for the differences between the path lengths:

$$\begin{aligned}
r_{k2} - r_{k1} - (r_{l2} - r_{l1}) &= 0 && \text{for } k = l,\ k, l \in \{1 \ldots M\} \\
r_{k2} - r_{k1} - (r_{l2} - r_{l1}) &= -\frac{\lambda}{M} && \text{for } k = 2,\ l = 1, \text{ and } k = 3,\ l = 2 \\
r_{k2} - r_{k1} - (r_{l2} - r_{l1}) &= -2\frac{\lambda}{M} && \text{for } k = 3,\ l = 1 \\
r_{k2} - r_{k1} - (r_{l2} - r_{l1}) &= \frac{\lambda}{M} && \text{for } k = 1,\ l = 2, \text{ and } k = 2,\ l = 3
\end{aligned}$$

$$r_{k2} - r_{k1} - (r_{l2} - r_{l1}) = 2\frac{\lambda}{M} \qquad \text{for } k = 1,\ l = 3$$

Note that the antenna arrangement in Figure 4.1b is just one example that fulfills (4.12). Theoretically unlimited solutions of antenna arrangements are still possible.

If a 2×2 MIMO link is considered, condition (4.12) simplifies to

$$|r_{22} - r_{21} - (r_{12} - r_{11})| = v \cdot \lambda/2,\ v \in \mathbb{Z}^+,\ v \nmid 2. \tag{4.13}$$

In many practically relevant applications, the 2×2 MIMO satellite link is a basic design foundation.

4.1.3. Downlink Channels with Arbitrary Numbers of Antennas

If more than two antennas are considered at both sides of the link, an assumption must be made with respect to the antenna arrangement in order to find a practical solution to (4.7) and to further simplify (4.12). One possibility is to assume a linear antenna array on the satellite (like it is already the case in current antenna accommodations, e.g. the design of the KA-SAT [FTA+16]) as well as on the ground. If the antennas are assumed to be arranged as ULAs at both sides of a MIMO channel, the introduced limitation of $Z = 2$ satellite antennas can be relaxed. In this case, (4.12) can be simplified to achieve the result reported in [SN06] for short range terrestrial MIMO networks.

If additionally a large distance between the transmitter and receiver compared to the array dimensions is assumed[7], it is revealed through geometrical analysis that

$$(r_{ml} - r_{mk}) - (r_{m+1l} - r_{m+1k}) \approx \tau,\ \forall m \in \{1, \ldots, M-1\}, k, l \in \{1, \ldots, Z\}, k > l, \tag{4.14}$$

where τ is any fixed value in $\mathbb{R}$. Since the array elements at both link ends are uniformly distributed, the following approximation is also valid:

$$(r_{ml} - r_{mk}) \approx (k - l)(r_{m2} - r_{m1}), m \in \{1, \ldots, M\}, k, l \in \{1, \ldots, Z\}. \tag{4.15}$$

The two relations (4.14) and (4.15) can be graphically illustrated by means of the unit complex numbers defined in (4.3) because any periodicity between the path length differences directly relates to the phase of the complex unit numbers. To this end, the unit complex numbers from (4.3) are graphically illustrated in Figure 4.2. In this example $Z = 4$ transmit antennas and $M = 4$ receive antennas are arranged as ULA forming a 4×4 MIMO system[8]. Therefore, the figure shows $Z \cdot Z = 16$

[7] This is a valid assumption for GEO applications since the Earth-to-space distance is at least 35 786.1 km, while the array dimensions are assumed to be not larger than several tens of km.

[8] The aim of Figure 4.2 is to illustrate the location of the unit complex numbers from (4.3) on

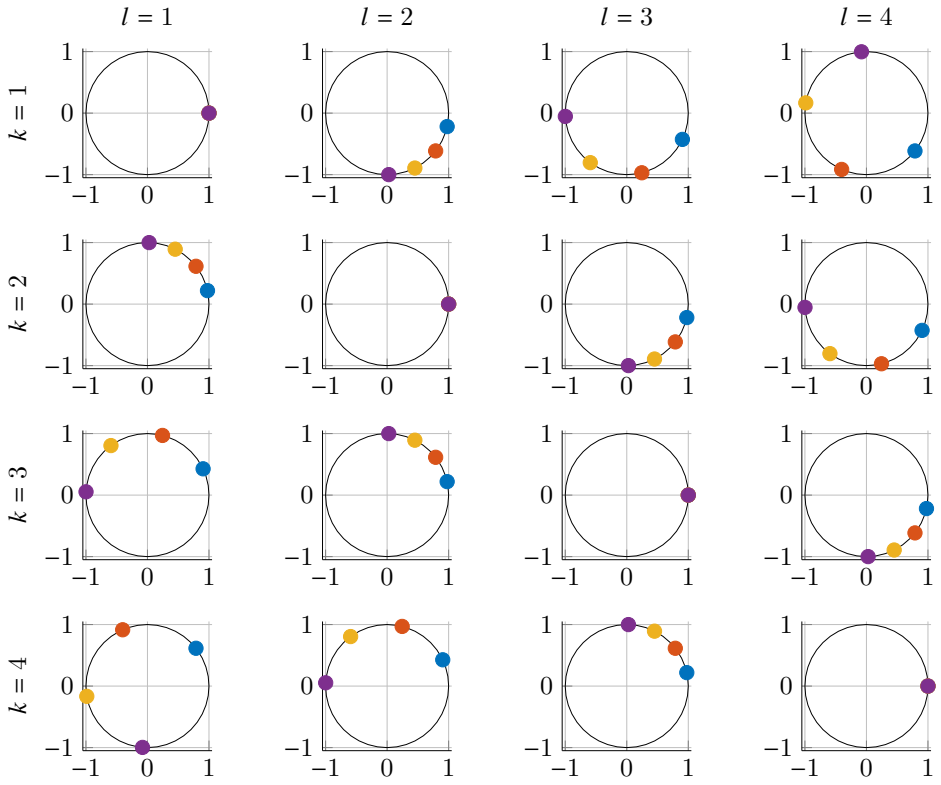

Figure 4.2.: Graphical illustration of the unit complex numbers from (4.3) and their respective location on the unit circle for the case of ULA antenna arrangements at both link ends; example for the case $Z = 4$ and $M = 4$.

unit circles. Each unit circle contains $M = 4$ unit complex numbers. To give an example, the lower left unit circle is associated to the case $k = 4$ and $l = 1$ and shows the $m = 1,\ldots,M = 4$ unit complex numbers derived from (4.3) for this particular parameter set k,l. The unit complex numbers that correspond to the m-th receive antenna have identical color. In particular, the unit complex numbers for $m = 1$ are blue, for $m = 2$ are red, for $m = 3$ are yellow and for $m = 4$ are purple for all $k,l \in \{1,\ldots,4\}$.

It is clear from (4.3) that all unit complex numbers are real for $k = l$, which is also the case in Figure 4.2. The angular distance between neighboring unit complex numbers in one unit circle (i.e. the unit complex numbers for one parameter set (k,l)) are indeed almost identical. This is expressed by (4.14). Furthermore, the phase advance of the unit complex numbers between neighboring subplots with fixed m is also virtually constant (in the example of Figure 4.2 approximately $\pi/2$). This

the unit circle when ULAs are applied. The detailed parameter setup (e.g. frequency, antenna displacement, transmitter-receiver distance, etc.) to obtain this plot has no relevance.

relation is expressed by (4.15). Thus, (4.14) and (4.15) hold for all combinations of the indices k,l,m with $k > l$, and we can set w.l.o.g. $k = 2$, $l = 1$ and $m = 1$. Using (4.7) in (4.14) finally yields

$$|(r_{21} - r_{11}) - (r_{22} - r_{12})| \approx v\lambda/M,\ v \in \mathbb{Z}^+,\ v \nmid M, M \geq Z. \tag{4.16}$$

This result has first been published in [SKO+08] in 2008 for MIMO SATCOM applications. Although the derivation has been slightly different and was limited to $Z = 2$ satellite antennas, (4.16) tackles the solution presented in [SKO+08]. It satisfies (4.3) under the constraint that ULA geometries are used at both link ends. Moreover, the result remains valid for $M < Z$ by replacing M with Z on the right hand side of the equation. Thus, the result in (4.16) can be generalized to arbitrary antenna numbers on Earth and in orbit by using again the definition $V = \max\{M, Z\}$.

For the sake of compact notation, let denote by

$$r_{\text{diff}} = |(r_{21} - r_{11}) - (r_{22} - r_{12})| \tag{4.17}$$

the actual difference between the four path lengths r_{11}, r_{12}, r_{21} and r_{22}. With (4.16), it follows that

$$r_{\text{diff}} \approx v \cdot \lambda/V,\ v \in \mathbb{Z}^+,\ v \nmid V. \tag{4.18}$$

must be fulfilled so that an optimal antenna arrangement is obtained.

Note again that the derived results in (4.18) for a MIMO system with arbitrary antenna numbers as well as in (4.12) for an $M \times 2$ system assume uniform linear array antenna configurations. Without this precondition on the equidistant antenna displacement, a closed form solution of the general criterion in (4.3) is not possible. An assessment of the approximation error in (4.18) is provided in Section B.1, showing that (4.18) holds with negligible loss of accuracy for all relevant MIMO satellite application scenarios.

4.1.4. Required Positioning Accuracy and Capacity Degradation

The degradation of the optimal capacity C_{opt} is now analyzed if (4.18) is not exactly fulfilled. To this end, the relative deviation of the actual antenna arrangement r_{diff} from the optimal arrangement λ/V is defined as

$$\varepsilon_{r_{\text{diff}}} = \frac{r_{\text{diff}} - v \cdot \lambda/V}{\lambda/V}. \tag{4.19}$$

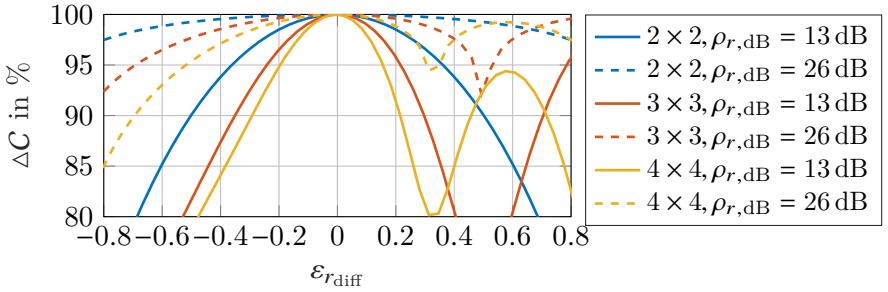

(a) Wide view on y- and x-axis.

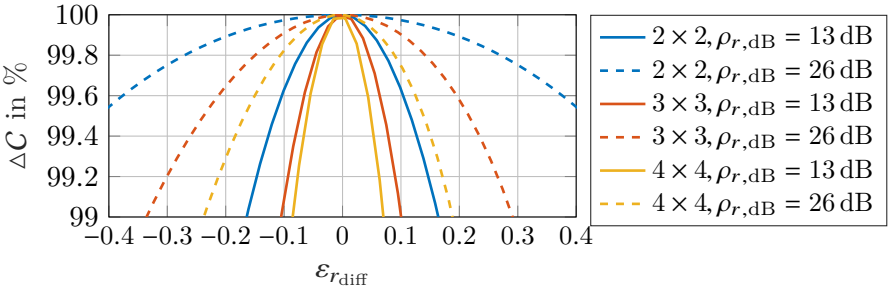

(b) Zoomed view on y- and x-axis.

Figure 4.3.: Capacity degradation relative to its optimum value $\triangle C$ as a function of the deviation from the optimal antenna arrangement $\varepsilon_{r_{\text{diff}}}$.

Its value is zero if the antennas are optimally placed for a specific value of v. It can be positive or negative, depending on the actual difference between the path lengths r_{diff}. For a fixed value of v, the deviation $\varepsilon_{r_{\text{diff}}}$ can be larger than One meaning that the actual antenna arrangement r_{diff} can be multiples of λ/V.

The capacity relative to its optimum value is defined by

$$\triangle C = C/C_{\text{opt}}. \tag{4.20}$$

The relative capacity $\triangle C$ of the downlink is shown in Figure 4.3 as a function of the parameter $\varepsilon_{r_{\text{diff}}}$. The uplink is neglected. The receive SNR in decibel is then given by $\rho_{r,\text{dB}} = 10\log_{10}\left(\rho\,|a|^2\right)$, which is shown in the legend of Figure 4.3. The curves apply for $v = 1$. The point $\varepsilon_{r_{\text{diff}}} = 0$ refers therefore to the first capacity optimum.

As expected, the higher the deviation of $\varepsilon_{r_{\text{diff}}}$ from zero, the higher is the capacity degradation. As the number of singular values increases with the number of antennas, the variation of the singular values is increased for the same value of $\varepsilon_{r_{\text{diff}}}$. The slopes of the curves are steeper if more antennas are considered and, hence, a higher positioning accuracy is required. Moreover, due to the decreased slope of the logarithm for large values, a higher SNR reduces the sensitivity of the capacity with respect to deviations from the optimal antenna arrangement.

Furthermore, C oscillates for $\varepsilon_{r_{\text{diff}}} > 0$ (red and yellow curves in Figure 4.3a) because the optimal antenna arrangement is periodic, which is described by the parameter v. In addition, the curves for $V > 2$ antennas show local maxima (e.g. the yellow curve at approximately $\varepsilon_{r_{\text{diff}}} = 0.6$) and are slightly asymmetric around $\varepsilon_{r_{\text{diff}}} = 0$ because for $V > 2$ the channel provides more than two eigenvalues. As a consequence, the possibilities of a particular eigenvalue profile are increased. This leads to a local maxima if, for example, three out of four eigenvalues are equal.

The measure $\varepsilon_{r_{\text{diff}}}$ as defined in (4.19) along with its relation to a specific capacity degradation $\triangle C$ will be used to analyze the required positioning accuracy and to assess the capacity degradation if the antennas are not optimally placed.

4.2. Optimal MIMO Uplink and Downlink

4.2.1. Optimal MIMO Uplink Channel

To achieve the maximum channel capacity according to (3.18), the antenna arrangement of both the uplink *and* the downlink must be optimized. The derived solutions in (4.12) and (4.18) can equally be applied to find an optimal antenna arrangement in the uplink because they only depend on the path lengths between the antennas and the wavelength of the carrier. Therefore, applying the uplink parameter notation to (4.18), it follows that

$$\left|\left(r_{\text{u},21} - r_{\text{u},11}\right) - \left(r_{\text{u},22} - r_{\text{u},12}\right)\right| \approx v \cdot \lambda_{\text{u}}/V_{\text{u}},\ v \in \mathbb{Z}^{+},\ v \nmid V_{\text{u}}, \tag{4.21}$$

must be fulfilled to obtained an optimal antenna arrangement in the uplink. If the differences between the path lengths satisfy (4.18) for an $M \times Z$ downlink and (4.21) for a $Z \times N$ uplink, the MIMO LOS channel matrices $\mathbf{H}_{\text{d}}$ and $\mathbf{H}_{\text{u}}$ have equally strong singular values. If, in addition, the antennas in up- and downlink are perfectly aligned and the atmosphere has no additional attenuation, the maximum channel capacity according to (3.18) is achieved.

4.2.2. Return Link and Non-Zero System Bandwidth

The carrier frequency differs between uplink and downlink. An optimal arrangement can be found for a particular λ_{u} in the uplink and λ_{d} in the downlink. This antenna arrangement is then optimal for one direction of transmission, e.g. the forward link between two sites. If the same MIMO satellite system shall be used to establish a return link, the antenna arrangement is no longer optimal.

Moreover, satellite systems utilize a certain portion of the frequency spectrum, for example a bandwidth of 500 MHz in the downlink ranging from 19.7 GHz to 20.2 GHz. Since the antenna arrangement can only be optimized for one particular

carrier frequency $f_\mathrm{u} = c_0/\lambda_\mathrm{u}$ (respectively, $f_\mathrm{d} = c_0/\lambda_\mathrm{d}$), a degradation of C_opt is expected if the system is operated at different frequencies than f_u (f_d).

The relative deviation from the optimal value can be calculated by

$$\varepsilon_{r_\mathrm{diff}} = \left(v\frac{c_0}{fV} - v\frac{c_0}{(f+\triangle f)V} \right) \cdot \frac{(f+\triangle f)V}{c_0} = v \cdot \triangle f/f, \tag{4.22}$$

where $\triangle f$ denotes the frequency separation from the carrier frequency f which the satellite system has been optimized for. The deviation $\varepsilon_{r_\mathrm{diff}}$ is linear with respect to $\triangle f$ having a slope of v/f. The higher f, the higher frequency separations $\triangle f$ to f are possible for the same $\varepsilon_{r_\mathrm{diff}}$.

For example, consider a 2×2 uplink with $f_\mathrm{d} = 30\,\mathrm{GHz}$ and a required frequency range of 29 GHz to 31 GHz. Using (4.22) it follows that $\varepsilon_{r_\mathrm{diff}} = \pm 0.033$. With the curves of Figure 4.3b, the capacity loss is less than 0.05 % of C_opt at an SNR of 13 dB. In the return direction, this 2×2 MIMO uplink shall support additionally carrier frequencies of 20 GHz (Ka-band downlink). Thus, $\triangle f = -10\,\mathrm{GHz}$ and it follows that $\varepsilon_{r_\mathrm{diff}} = -0.33$. Using the curves of Figure 4.3a (blue solid line) a capacity loss of about 4 % of C_opt must be accepted.

A small degradation of C_opt must be considered in future satellite designs since the MIMO satellite system cannot be optimized for all carrier frequencies that must be supported. The total amount of capacity loss compared to the linear increase of C_opt with respect to C_SISO remain low. Simulation results in Chapter 5 of an HTS scenario utilizing up to 4 GHz of bandwidth will later show that still a huge data rate advantage compared to the state-of-the-art is achieved.

4.3. Derivation of the Optimal Antenna Positions

The objective of this section is to derive an analytical equation that calculates the optimal locations of the MIMO antennas of a GEO satellite link. To this end, the path lengths $r_{\mathrm{u},zn}$ and $r_{\mathrm{d},mz}$ of the up- and downlink, respectively, must be calculated, which are determined by the geographical locations of the antennas on Earth and in space. A set of geometrical design parameters is introduced first that exactly defines the geographical locations of the ground and satellite antennas. The same model is used for uplink and downlink. The distinction in the notation between uplink and downlink is, therefore, omitted in this section.

4.3.1. Analytical Description of the Antenna Positions

All the required parameters are illustrated in Figure 4.4. To analytically describe the antenna positions on Earth and in orbit an Earth-centered Earth-fixed (ECEF) reference frame [MB09, chapter 2.1.6] is used. The x-axis and the y-axis lie in the

Table 4.1.: Definition of the required parameters to analytically describe the geographical positions of the MIMO antennas.

Parameter	**Value/range**	**Explanation**
Earth station parameters:		
ϕ_{E}	$-81.3° \leq \phi_{\mathrm{E}} \leq 81.3°$	latitude of earth station at center of ULA
θ_{E}	$-180° \leq \theta_{\mathrm{E}} \leq 180°$	longitude of earth station at center of ULA
δ_{E}	$-180° \leq \delta_{\mathrm{E}} \leq 180°$	orientation angle of earth station ULA
d_{E}	–	antenna element spacing of earth station ULA
$d_{\mathrm{E},m}$	–	distance of m-th antenna from center of earth station ULA
Satellite parameters:		
$R_{\oplus}$	6378.1 km	mean equatorial radius
$r_{\min}$	35 786.1 km	GEO satellite altitude above equator
R_o	42 164.2 km	GEO radius, measured from earth center
θ_{s}	$-180° \leq \theta_{\mathrm{s}} \leq 180°$	orbit position (center) of the satellite ULA
$\triangle\theta_{\mathrm{s}}$	–	antenna spacing (orbital distance) of satellite ULA in degree
δ_{s}	$-90° \leq \delta_{\mathrm{s}} \leq 90°$	orientation of satellite ULA
d_{s}	–	antenna spacing of satellite ULA in meter
$d_{\mathrm{s},z}$	–	distance of z-th satellite antenna from center of satellite ULA

equatorial plane with the x-axis in the direction of the Greenwich Meridian. The y-axis has an angle of 90° to the x-axis, and the z-axis is perpendicular to the x- and the y-axis in the direction from South to North in order to form a right-handed coordinate system with the Earth's center of mass in its origin. W.l.o.g. the angular values of the geographical longitudes are positive in the case where the position is in the eastern hemisphere, i.e. right hand from the Greenwich Meridian, and they are negative in the case where the location is in the western hemisphere, i.e. left hand from the Greenwich Meridian. In addition to the graphical illustration in Figure 4.4, in Table 4.1 a short explanation of each parameter and its respective value or its valid range of values are indicated for easy reference.

4.3.1.1. Earth Station Antenna Positions

The M earth station antennas are arranged within a uniform linear array (ULA) having an inter-antenna distance of d_{E}. For the sake of simplicity the distance between the Earth's center and any point on its surface is set equal to the mean equatorial radius $R_{\oplus} = 6378.1\,\mathrm{km}$. Since the distance between the earth station

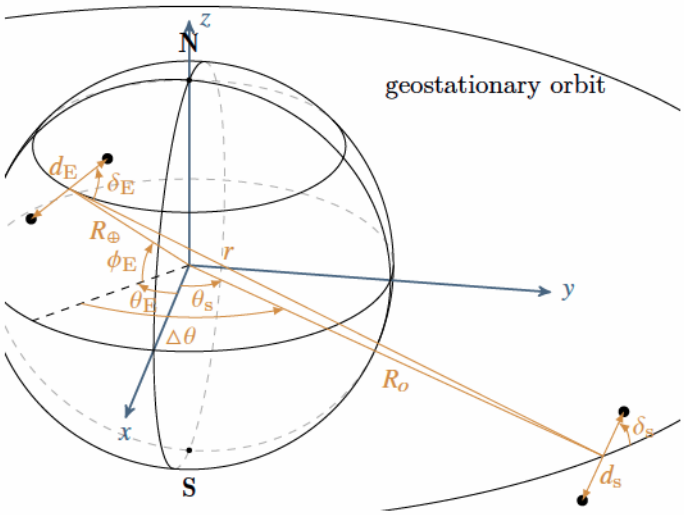

Figure 4.4.: Definition of geographical parameters in an ECEF reference frame to mathematically describe the antenna positions.

antennas d_E is small compared to $R_\oplus$, the Earth curvature is neglected. As shown later in Section 4.3.3, this simplification is reasonable and has a negligible impact on the optimal design of the MIMO satellite link. The geographical latitude ϕ_E and the geographical longitude θ_E specify the center of the ULA. The orientation δ_E characterizes the angle between the east-west direction and the antenna array. For example, if $\delta_E = 90°$, the earth station ULA is oriented in the north-south direction, i.e. all antennas are located at the same geographical longitude. If $\delta_E = 0°$, the antennas are oriented in the east-west direction, i.e. all earth station antennas are located at the same geographical latitude. This set of parameters fully defines the position of the ground antennas. The positioning vector $\mathbf{a}_{E,m} = \left[x_{E,m}, y_{E,m}, z_{E,m}\right]^T$ of the m-th earth station antenna in three-dimensional Cartesian coordinates is given by

$$\mathbf{a}_{E,m} = \begin{bmatrix} R_\oplus \cos\phi_E \cos\theta_E - d_{E,m} \cdot (\sin\theta_E \cos\delta_E + \sin\phi_E \cos\theta_E \sin\delta_E) \\ R_\oplus \cos\phi_E \sin\theta_E + d_{E,m} \cdot (\cos\theta_E \cos\delta_E - \sin\phi_E \sin\theta_E \sin\delta_E) \\ R_\oplus \sin\phi_E + d_{E,m} \cdot \cos\phi_E \sin\delta_E \end{bmatrix}, \tag{4.23}$$

with $m \in \{1, \ldots, M\}$. The parameter

$$d_{E,m} = d_E \cdot (m - 1/2 - M/2),\ m \in \{1, \ldots, M\} \tag{4.24}$$

defines the distance between the center of the earth station ULA and the m-th antenna. Note that $d_{E,m} \leq 0$ for $m \leq M/2$.

4.3.1.2. Satellite Antenna Positions

At the satellite, the Z antennas are arranged as a uniform linear array (ULA). It is assumed that the imaginary line of the ULA is perpendicular towards the satellite's yaw axis. Therefore, the satellite ULA lies in the roll-pitch plane of the satellite and can be rotated normal to the yaw axis which is described by the orientation angle δ_s. To simplify the mathematical description, an ideal geostationary Kepler orbit and no orbit perturbations are assumed first. As a consequence, the eccentricity and the inclination of the satellite are negligible small, and the yaw axis points ideally towards the center of the Earth. The impact of satellite movements as a result of non-ideal geostationary orbits will be analyzed later in Section 4.6. Denoting θ_s as the longitude of the center of the antenna array, d_s as the inter-antenna spacing, and δ_s as the orientation of the linear array with respect to the equatorial plane, the position of the z-th satellite antenna in three-dimensional Cartesian coordinates is given as

$$\mathbf{a}_{\mathrm{s},z} = \begin{bmatrix} x_{\mathrm{s},z} \\ y_{\mathrm{s},z} \\ z_{\mathrm{s},z} \end{bmatrix} = \begin{bmatrix} R_o \cos\theta_\mathrm{s} - d_{\mathrm{s},z} \sin\theta_\mathrm{s} \cos\delta_\mathrm{s} \\ R_o \sin\theta_\mathrm{s} + d_{\mathrm{s},z} \cos\theta_\mathrm{s} \cos\delta_\mathrm{s} \\ d_{\mathrm{s},z} \sin\delta_\mathrm{s} \end{bmatrix},\ z \in \{1,\ldots,Z\}\,. \tag{4.25}$$

The parameter $R_o = 42\,164.2\,\mathrm{km}$ is the ideal GEO radius. Similar to (4.24), the parameter

$$d_{\mathrm{s},z} = d_\mathrm{s} \cdot (z - 1/2 - Z/2),\ z \in \{1,\ldots,Z\} \tag{4.26}$$

defines the distance between the center of the ULA in the orbit and the z-th satellite antenna. Recall that $d_{\mathrm{s},z} \leq 0$ for $z \leq Z/2$.

4.3.2. Calculation of the Optimal Antenna Locations

Using the mathematical description of the antenna positions in (4.23) and in (4.25), the distances between the antenna pairs can now be analytically expressed as follows. The path length r_{mz} is defined as the distance between the position vectors $\mathbf{a}_{\mathrm{E},m}$ and $\mathbf{a}_{\mathrm{s},z}$, i.e.

$$r_{mz} = \left\| \mathbf{a}_{\mathrm{E},m} - \mathbf{a}_{\mathrm{s},z} \right\|, \tag{4.27}$$

where $\|.\|$ abbreviates the Euclidean distance and, thus, delivers the geometrical length of a vector in Cartesian coordinates. The Euclidean distance leads to

$$r_{mz} = \left[\left(x_{\mathrm{E},m} - x_{\mathrm{s},z}\right)^2 + \left(y_{\mathrm{E},m} - y_{\mathrm{s},z}\right)^2 + \left(z_{\mathrm{E},m} - z_{\mathrm{s},z}\right)^2 \right]^{1/2}, \tag{4.28}$$

where the three square terms in (4.28) are given by

$$\left(x_{\mathrm{E},m} - x_{\mathrm{s},z}\right)^2 = \Big(R_\oplus \cos\phi_\mathrm{E} \cos\theta_\mathrm{E} - d_{\mathrm{E},m} \sin\theta_\mathrm{E} \cos\delta_\mathrm{E} - d_{\mathrm{E},m} \sin\phi_\mathrm{E} \cos\theta_\mathrm{E} \sin\delta_\mathrm{E} - R_o \cos\theta_\mathrm{s} + d_{\mathrm{s},z} \sin\theta_\mathrm{s} \cos\delta_\mathrm{s}\Big)^2, \tag{4.29}$$

$$\left(y_{\mathrm{E},m} - y_{\mathrm{s},z}\right)^2 = \Big(R_\oplus \cos\phi_\mathrm{E} \sin\theta_\mathrm{E} + d_{\mathrm{E},m} \cos\theta_\mathrm{E} \cos\delta_\mathrm{E} - d_{\mathrm{E},m} \sin\phi_\mathrm{E} \sin\theta_\mathrm{E} \sin\delta_\mathrm{E} - R_o \sin\theta_\mathrm{s} - d_{\mathrm{s},z} \cos\theta_\mathrm{s} \cos\delta_\mathrm{s}\Big)^2, \text{ and} \tag{4.30}$$

$$\left(z_{\mathrm{E},m} - z_{\mathrm{s},z}\right)^2 = \left(R_\oplus \sin\phi_\mathrm{E} + d_{\mathrm{E},m} \cos\phi_\mathrm{E} \sin\delta_\mathrm{E} - d_{\mathrm{s},z} \sin\delta_\mathrm{s}\right)^2. \tag{4.31}$$

Applying the binomial expansion of $(a+b+c+d+e)^2$ in (4.29) and in (4.30), and of $(a+b+c)^2$ in (4.31), and using additionally the trigonometrical theorems $\sin^2 x + \cos^2 x = 1$, $\sin x \cos y - \cos x \sin y = \sin(x-y)$, and $\cos x \cos y + \sin x \sin y = \cos(x-y)$, the distance r_{mz} is then given by

$$r_{mz} = \left(r^2 + 2d_{\mathrm{E},m} R_o \alpha - 2R_\oplus d_{\mathrm{s},z} \beta + 2d_{\mathrm{E},m} d_{\mathrm{s},z} \psi + d_{\mathrm{E},m}^2 + d_{\mathrm{s},z}^2\right)^{1/2} \tag{4.32}$$

$$= r \cdot (1 + \Delta_{mz})^{1/2}. \tag{4.33}$$

In (4.33) the substitution

$$\Delta_{mz} = \left(2d_{\mathrm{E},m} R_o \alpha - 2d_{\mathrm{s},z} R_\oplus \beta + 2d_{\mathrm{E},m} d_{\mathrm{s},z} \psi + d_{\mathrm{E},m}^2 + d_{\mathrm{s},z}^2\right) / r^2 \tag{4.34}$$

is introduced. The parameter

$$r = \left(R_o^2 + R_\oplus^2 - 2R_o R_\oplus \cos\phi_\mathrm{E} \cos\triangle\theta\right)^{1/2} = r_{\min} \cdot \triangle r \tag{4.35}$$

denotes the geometrical distance between the center of the earth station ULA and the center of the satellite ULA, where $r_{\min} = R_o - R_\oplus = 35\,786.1$ km is the minimum satellite-to-Earth distance, which is obtained when the earth station is directly at the sub-satellite point. The parameter

$$\triangle r = (1.42 - 0.42 \cos\phi_\mathrm{E} \cos\triangle\theta)^{1/2}, \triangle r \in [1, 1.16] \tag{4.36}$$

describes the relative increase of the satellite-to-earth station distance depending on the geographical latitude ϕ_E and the parameter $\triangle\theta$. The given value range of $\triangle r$ results from $81.3° \geq |\phi_\mathrm{E}|, |\triangle\theta|$ which considers the fact that the visibility of the GEO arc is limited to elevation angles that are larger or equal to Zero. The parameter $\triangle\theta = (\theta_\mathrm{E} - \theta_\mathrm{s})$ denotes the relative longitude of the center of the earth station ULA with respect to the orbit position of the satellite ULA. Furthermore, for the sake of a compact notation in (4.33), the following substitutions have been

introduced:

$$\alpha = \cos\delta_{\mathrm{E}} \sin\triangle\theta + \sin\phi_{\mathrm{E}} \sin\delta_{\mathrm{E}} \cos\triangle\theta, \tag{4.37}$$

$$\beta = \cos\phi_{\mathrm{E}} \cos\delta_{\mathrm{s}} \sin\triangle\theta + \sin\phi_{\mathrm{E}} \sin\delta_{\mathrm{s}}, \text{ and} \tag{4.38}$$

$$\psi = \sin\phi_{\mathrm{E}} \sin\delta_{\mathrm{E}} \cos\delta_{\mathrm{s}} \sin\triangle\theta - \cos\delta_{\mathrm{E}} \cos\delta_{\mathrm{s}} \cos\triangle\theta - \cos\phi_{\mathrm{E}} \sin\delta_{\mathrm{E}} \sin\delta_{\mathrm{s}}. \tag{4.39}$$

In order to obtain a convenient analytical expression of the left side of (4.18), the square root $(1+\Delta_{mz})^{1/2}$ in (4.33) needs to be solved. One possibility is to approximate the square term $(1+\Delta_{mz})^{1/2}$ by a Taylor polynomial derived around $\Delta_{mz} = 0$. Denoting $P_{mz}^{(K)}$ the K-th order Taylor polynomial of r_{mz}, the differences between the path lengths in (4.18) can be approximated by

$$r_{\mathrm{diff}} = \left|\left(P_{21}^{(K)} - P_{11}^{(K)}\right) - \left(P_{22}^{(K)} - P_{12}^{(K)}\right) + \triangle R^{(K)}\right| \approx \left|\left(P_{21}^{(K)} - P_{11}^{(K)}\right) - \left(P_{22}^{(K)} - P_{12}^{(K)}\right)\right|.$$

The parameter $\triangle R^{(K)} = \left(R_{21}^{(K)} - R_{11}^{(K)}\right) - \left(R_{22}^{(K)} - R_{12}^{(K)}\right)$ denotes the total remainder due to the Taylor series approximation, and $R_{mz}^{(K)}$ is the remainder such that $r_{mz} = P_{mz}^{(K)} + R_{mz}^{(K)}$. To keep the total approximation error below a certain threshold, a minimum number of K partial sums of the Taylor series must be considered. Simulation results will later show that $K = 2$ is sufficient and provides the necessary accuracy for all practically relevant cases. Approximating r_{mz} by its second order Taylor polynomial results in[9]

$$r_{mz} \approx P_{mz}^{(2)} = r \cdot \left(1 + \frac{1}{2}\Delta_{mz} - \frac{1}{8}\Delta_{mz}^2\right). \tag{4.40}$$

The difference between the path-lengths r_{mz} in (4.18) is then given by

$$r_{\mathrm{diff}} = \left|\left(P_{21}^{(2)} - P_{11}^{(2)}\right) - \left(P_{22}^{(2)} - P_{12}^{(2)}\right) + \triangle R^{(2)}\right| \tag{4.41}$$

$$\approx \left|\left(P_{21}^{(2)} - P_{11}^{(2)}\right) - \left(P_{22}^{(2)} - P_{12}^{(2)}\right)\right| \tag{4.42}$$

$$= r \cdot \left|\frac{\Delta_{21}}{2} - \frac{\Delta_{21}^2}{8} - \frac{\Delta_{11}}{2} + \frac{\Delta_{11}^2}{8} - \left(\frac{\Delta_{22}}{2} - \frac{\Delta_{22}^2}{8} - \frac{\Delta_{12}}{2} + \frac{\Delta_{12}^2}{8}\right)\right| \tag{4.43}$$

$$\approx \frac{d_{\mathrm{E}} d_{\mathrm{s}}}{r} \left|\psi + R_{\oplus} R_o \alpha\beta / r^2 - 1/8 \left(d_{\mathrm{E}}^2 + d_{\mathrm{s}}^2\right) \psi / r^2\right| \tag{4.44}$$

$$\approx \frac{d_{\mathrm{E}} d_{\mathrm{s}}}{r} \left|\psi + R_{\oplus} R_o \alpha\beta / r^2\right| = \frac{d_{\mathrm{E}} d_{\mathrm{s}}}{r_{\min}} \left|\psi / \triangle r + 0.21 \cdot \alpha\beta / \triangle r^3\right|. \tag{4.45}$$

The full expression of (4.43) as well as the intermediate calculation steps to get

[9] The detailed derivation including a full expression of the second order Taylor polynomial is given in Appendix C.1

from (4.43) to (4.44) are given in Appendix C.2. Using now (4.45) in (4.18) finally results in the desired analytical solution for the **O**ptimal **P**ositioning of the MIMO **A**ntennas (OPA) on Earth and in orbit:

$$d_{\mathrm{E}} d_{\mathrm{s}} / r_{\min} \cdot \left| \psi / \triangle r + 0.21 \cdot \alpha\beta / \triangle r^3 \right| \approx v \cdot \lambda / V, \; v \in \mathbb{Z}^+, \; v \nmid V. \tag{4.46}$$

The left part of (4.46) is a function of the introduced geographical design parameters, which clearly define the location of the MIMO antennas on Earth and in orbit. This formula allows to calculate the optimal geographical locations of the ground antennas in relation to the satellite antennas in the GEO. To summarize the derivation of the OPA, the following steps have been performed:

1. The necessary phase relations in the channel matrix **H** have been identified that lead to orthogonal row/column vectors (eq. (4.3)).

2. The required phase relations were then translated into particular differences between the lengths of the LOS propagation paths (eq. (4.7)).

3. Assuming uniform linear antenna arrays, a solution for the optimal difference between the LOS path lengths have been derived (eq. (4.18) and (4.21)).

4. A model to describe the antenna positions on Earth and in the GEO has been introduced based on conventional geographical location parameters.

5. This model has been linked to the difference between the path lengths resulting in (4.46) that calculates the optimal antenna positions.

If the antennas in the uplink and downlink are placed such that the OPA criteria in (4.46) is fulfilled, the resulting MIMO LOS satellite channels $\mathbf{H}_{\mathrm{u}}$ and $\mathbf{H}_{\mathrm{d}}$ provide the maximum channel capacity C_{opt}.

4.3.3. Assessment of Approximation Errors and Simplifications

4.3.3.1. Simplifications in Equation (4.45)

To express the differences between the path lengths r_{diff} as a function of geographical parameters, multiple approximations from (4.41) to the result in (4.45) have been applied. A thorough analysis of the approximation error is provided in Appendix B.2, showing the accuracy to be sufficient for all practically relevant cases.

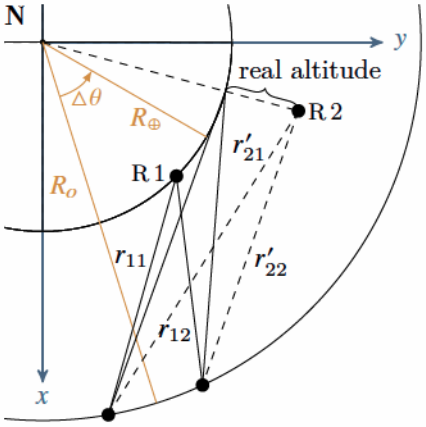

Figure 4.5.: Two-dimensional top-view illustrating different ground antenna altitudes (dimensions are not to scale)

4.3.3.2. Non-Spherical Earth

An ideal spherical Earth with mean equatorial radius $R_\oplus = 6378.1\,\text{km}$ has been assumed in (4.35) to calculate the distances between ground antennas and satellite array. With an oblateness of 1/298.257 [NIM97], the radius of the Earth at the Poles is approximately 6356.8 km, which differs from the mean equatorial radius by $\triangle R_\oplus = 21.4\,\text{km}$. The relative deviation $\varepsilon_{r_{\text{diff}}}$ because of this error becomes maximum for an earth station array at the sub-satellite point because in this case $r = r_{\min} = 35\,786.1\,\text{km}$. The maximum deviation $\varepsilon_{r_{\text{diff}}}$ from the optimal geometry is then calculated as

$$\varepsilon_{r_{\text{diff}}} = \frac{d_{\text{E}}^{(\text{opt})} d_{\text{s}}^{(\text{opt})} a_{rf}/(r_{\min} - \triangle R_\oplus) - \lambda/V}{\lambda/V} = \left(\frac{1}{1 - \triangle R_\oplus/r} - 1\right) = 6 \times 10^{-4},$$

which is sufficiently small and can be neglected.

4.3.3.3. Different Altitudes of Ground Antennas

The introduced model in Section 4.3.1 does not consider different altitudes between the earth station antennas. Whereas this is a valid simplification if the antennas are closely spaced, the altitudes can significantly deviate if the antennas are several tens of kilometers apart.

Figure 4.5 illustrates this effect. Receive antenna R 2 is elevated with respect to receive antenna R 1. The actual difference between the path lengths is given by

$$r_{\text{diff}} + \triangle r_{\text{diff}} = |(r_{21} - r_{22}) + (r_{12} - r_{11})| + (r'_{21} - r'_{22}) - (r_{21} - r_{22}),$$

where $\triangle r_{\text{diff}} = \left(r'_{21} - r'_{22}\right) - (r_{21} - r_{22})$ denotes the deviation between $(r_{21} - r_{22})$, which is based on the theoretical model, and the term $\left(r'_{21} - r'_{22}\right)$ that accounts for real local terrain at the location of R 2. The deviation from the optimal antenna array geometry is calculated as

$$\varepsilon_{r_{\text{diff}}} = \frac{r_{\text{diff}} + \triangle r_{\text{diff}} - v \cdot \lambda/V}{\lambda/V} = v \frac{\triangle r_{\text{diff}}}{\lambda/V}.$$

The value of $\triangle r_{\text{diff}}$ depends on the geometry between the satellite and the ground antennas. If the earth station array is at the sub-satellite point ($\triangle\theta = \phi_{\text{E}} = 0°$), an elevation of R 2 results in a shift of this antenna along the transmitter-receiver direction. Both r_{21} and r_{22} are similarly affected and $(r_{21} - r_{22})$ remain approximately constant. Thus, $\triangle r_{\text{diff}}$ is approximately zero and huge differential altitudes between the antennas are possible without a significant effect on C.

If the relative longitude $\triangle\theta$ is high and all MIMO antennas are in the equatorial plane ($\delta_{\text{E}} = \delta_{\text{s}} = 0°$ and $\phi_{\text{E}} = 0°$ as illustrated in Figure 4.5), the value of $\triangle r_{\text{diff}}$ becomes significant. Consider a pessimistic scenario with $\triangle\theta = 70°$ (results in an elevation angle of only 11°) and an altitude difference of 3 km between R 1 and R 2. A numerical calculation of the difference $\triangle r_{\text{diff}}$ results in $\triangle r_{\text{diff}} = 0.215\,\text{mm}$. Assuming $V = 2$, $v = 1$ and a comparably high carrier frequency of $f = 60\,\text{GHz}$, it follows for $\varepsilon_{r_{\text{diff}}}$ that

$$\varepsilon_{r_{\text{diff}}} = v \cdot 0.215\,\text{mm}/(\lambda/V) = 0.086.$$

Using the value of $\varepsilon_{r_{\text{diff}}} = 0.086$ in Figure 4.3b, C_{opt} is degraded by approximately 0.3 % (blue solid curve), i.e. still 99.7 % of C_{opt} is achieved. The simplification in the model to specify the antenna locations on Earth is therefore a valid assumption. Even with worst case parameter assumptions, the capacity degradation is very small and (4.46) provides reliable results.

4.4. Implications on the Positioning of the MIMO Antennas

4.4.1. Minimum Required Antenna Spacing

The two key parameters of the solution in (4.46) are the antenna spacings d_{E} on Earth and d_{s} in orbit. The spacing required is linearly proportional to the transmitter-receiver distance r and the wavelength, i.e. $d_{\text{s}} d_{\text{E}} \propto r\lambda$. Since $r = r_{\min} \cdot \triangle r \geq 35\,786.1\,\text{km}$, relatively large antenna spacings $d_{\text{s}} d_{\text{E}}$ are required to satisfy (4.46). The smallest array dimensions are generally obtained if both antenna arrays are in broadside and the earth station is at the sub-satellite point. In this case, we have $|\psi/\triangle r| = 1$, $\alpha = \beta = 0$, and $r = r_{\min}$. If we set $v = 1$, the minimum spacing of

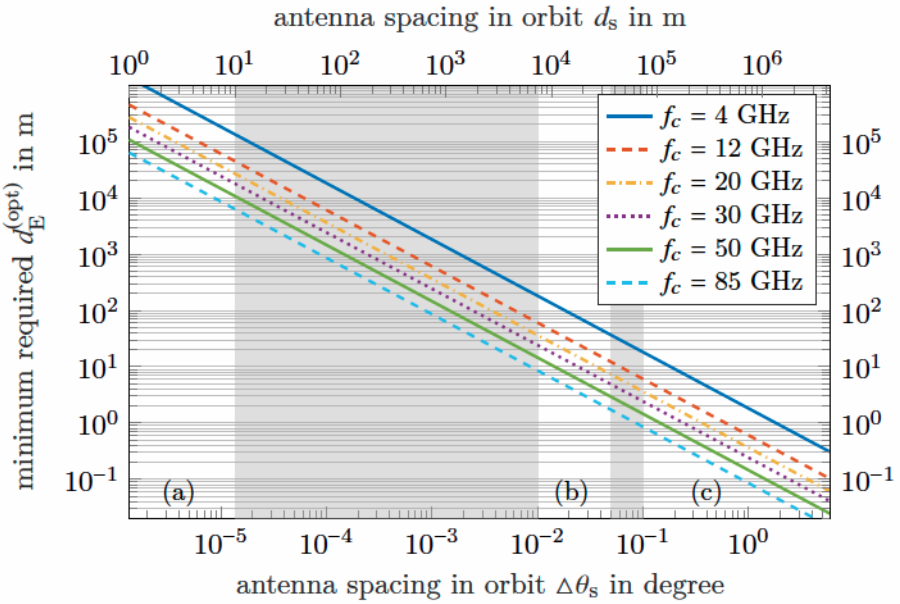

Figure 4.6.: Smallest optimal antenna spacing $d_E^{(opt)}$ versus antenna spacing in orbit, white areas indicate useful ranges related to the categories: (a) single-satellite applications, (b) co-located satellites applications, (c) multiple-satellites applications (see Section 4.4.2).

the earth station array becomes $d_E^{(opt)} = r_{min}\lambda/(V d_s)$. Smaller values of this spacing lead to severe spatial interference because the receive array is no longer capable to spatially resolve each transmit antenna. The transmit signals can no longer be distinguished at the receiver and the MIMO channel converges to the *keyhole channel* with $\mathbf{H} \approx a \left[\begin{smallmatrix} 1 & 1 \\ 1 & 1 \end{smallmatrix}\right]$. A similar limit is also known as the Rayleigh criterion describing the resolution limit of optical systems [Ray79].

Figure 4.6 shows the relation between d_E and the antenna spacing in orbit for different carrier frequencies. Since a wide range of values is provided, the curves are shown in double-logarithmic scale. For large antenna separations in orbit, it is convenient to define the orbital separation

$$\Delta\theta_s = 2 \cdot \sin^{-1}(0.5 \cdot d_s/R_o) \approx d_s/R_o, \tag{4.47}$$

which is given in degrees on the lower x-axis. The applied approximation of the form $\sin x \approx x$ is valid as long as the angles $\Delta\theta_s$ remain small. Assuming a satellite spacing not larger than $\Delta\theta_s = 5°$, the relative approximation error is below 0.032 %. The upper x-axis in Figure 4.6 shows d_s in meters. The values are valid for $M = Z = 2$, but can easily be scaled to higher antenna numbers using the relation $d_E \propto 1/V$. Since $|\psi| = 1$ and $\alpha = \beta = 0$, the antenna arrays are in broadside orientation, i.e.

$\delta_E = 0°$, and $\triangle\theta = 0°$.

4.4.2. Definition of MIMO SATCOM Categories

As indicated by the shaded areas in Figure 4.6, it is proposed to classify MIMO SATCOM systems into three basic categories. For each category, a particular range of antenna spacing in orbit is basically feasible as follows:

(a) Single-Satellite Application: All MIMO antenna elements are on a single-satellite and the useful antenna spacing is in the range of some centimeters up to some meter, for example $1\,\text{m} \leq d_s \leq 10\,\text{m}$.

(b) Co-located Satellites Application: Multiple satellites occupy a single orbital slot. Each satellite has one MIMO antenna element. A sufficient minimum separation between the spacecrafts must be ensured to account for inaccuracies of the tracking system and the thrusters [Soo94]. The upper bound is the station-keeping window, which is typically ±0.05° in longitude. Practically feasible antenna spacings are in the range of $0.01° \leq \triangle\theta_s \leq 0.05°$ (or equivalently $7\,\text{km} \leq d_s \leq 40\,\text{km}$). Applications of this category are very similar to the single-satellite case but at increased complexity since additional requirements with respect to co-location strategies are necessary [SK19].

(c) Multiple-Satellites Application: Multiple satellites with one MIMO antenna each are located at different orbit positions resulting in a spacing of $\triangle\theta_s \geq 0.1°$. If the orbital spacing is too large, a significant loss in SNR will be obtained due to the use of directional antennas. Simulation results will later show that satellite spacings of more than 1.5° are not of interest for FSS applications. As a general remark, this category of applications requires non-directional antennas at the ground segment because directional antennas cannot point at different orbital slots at the same time. As a promising application, UHF SATCOM has been proposed in [RCB16]. Moreover, measurements of the UHF MIMO satellite channel reported in [HSK17, SVK+17] have shown that the channel capacity can be significantly increased.

With respect to the required geometrical arrangement, Figure 4.6 emphasizes which spacings of the earth station antennas are minimal required depending on the MIMO SATCOM category considered. For example, in the single-satellite case, the minimum antenna spacing on Earth is approximately between 10 km and 100 km. Smaller antenna spacings d_E require larger spacings in the orbit leading to co-located satellite applications or to multiple-satellite applications. Note that larger but still optimal values for d_E can be obtained if $v > 1, v \nmid V$, is chosen, because the optimal antenna spacing scales with $v\lambda/V$, $v \nmid V$.

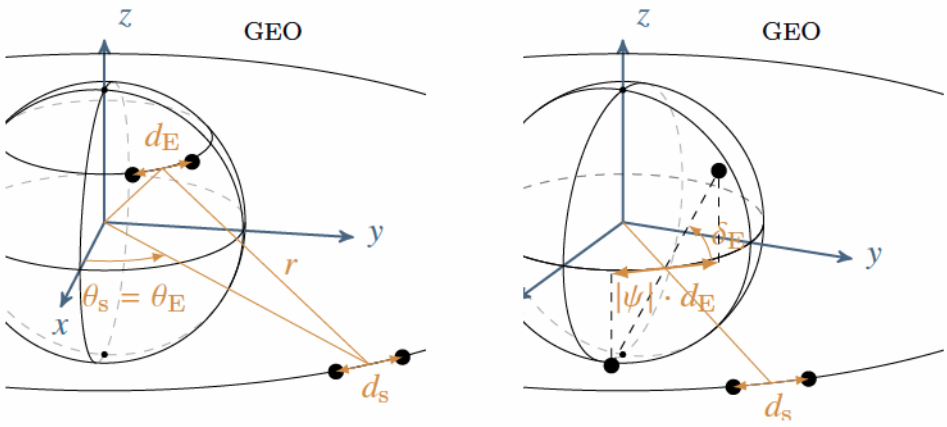

(a) *Broadside orientation* between antenna array.

(b) Illustration of *relevant antenna spacing* on earth as seen from satellite array.

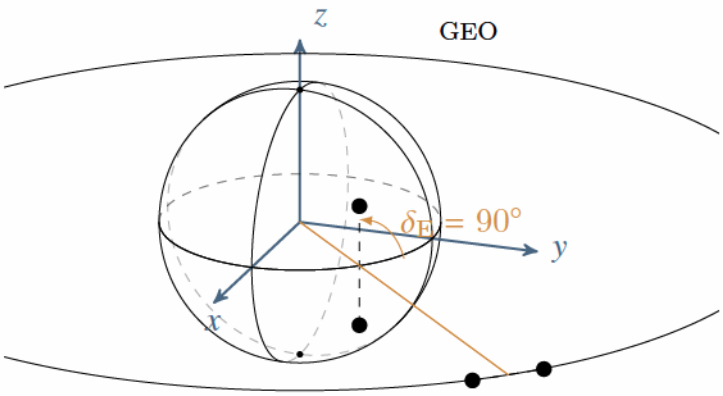

(c) *Keyhole orientation* between antenna arrays.

Figure 4.7.: Illustration of different antenna array configurations.

4.4.3. Relevant Antenna Spacing and Array Reduction Factor

The term

$$a_{rf} = \left|\psi/\Delta r + 0.21\alpha\beta/\Delta r^3\right| \in [0, +1] \tag{4.48}$$

in (4.46) can be interpreted as an *array reduction factor* because it reduces the effective antenna spacing d_E and d_s, depending on the parameters δ_s, δ_E, $\Delta\theta$ and ϕ_E. This parameter controls the orientation of the ULAs with respect to each other in the three-dimensional space. If the earth station ULA and the satellite ULA are not in broadside and the earth station ULA is not at the sub-satellite point, then $\left|\psi/\Delta r + 0.21\alpha\beta/\Delta r^3\right| < 1$, and the antenna spacings have to be increased accordingly to still satisfy (4.46). The earth station ULA and the satellite ULA are in broadside if the relative longitude $\Delta\theta$ and the orientation angles δ_E, δ_s are zero (see Figure 4.7a). If, in addition, the earth station ULA is at the sub-satellite point, then

$\triangle r = 1$ and the parameter a_{rf} is equal to One.

The ability of the receiving array to spatially resolve the signals from each transmit antenna is determined by the antenna spacings specified in the broadside of both arrays. Figure 4.7b provides a graphical illustration of $a_{rf} \in [0, +1]$. In this example, the earth station array is at the sub-satellite point ($\phi_{\mathrm{E}} = \triangle\theta = 0°$, tilted by 45°, and the satellite antennas are located in the equatorial plane ($\delta_{\mathrm{s}} = 0°$). The relevant antenna spacing, as seen from the satellite array, is then $d_{\mathrm{E}} \cdot \left|\psi/\triangle r + 0.21\alpha\beta/\triangle r^3\right| = d_{\mathrm{E}} \cdot |\psi| = d_{\mathrm{E}} \cdot \cos 45°$, which is smaller than the actual antenna spacing d_{E}. Since the two satellite antennas are located in the equatorial plane, this two-antenna linear array can only resolve the earth station antennas with respect to the east-west direction. The separation of the ground antennas in the north-south direction is "invisible" for the satellite array.

The worst antenna array configuration is the *keyhole orientation* (Figure 4.7c). In this case, no relevant spacing between the earth station antennas can be observed from the satellite array (and vice-versa) because the earth station array is rotated by 90° with respect to the equatorial plane. Hence, $a_{rf} = 0$ because $\alpha = \beta = \psi = 0$. No phase difference between the impinging signals at the receive antennas is observed because the propagation paths are all equal, i.e. $r_{11} = r_{12}$ and $r_{21} = r_{22}$. Condition (4.46) can no longer be satisfied and theoretically an unlimited antenna spacing would be required.

The actual required antenna spacing between the earth station antennas and the satellite antennas strongly depends on the orientation of the arrays with respect to each other. If the arrays are not in broadside, the relevant spacing is reduced by a_{rf}. To compensate this reduction, either the antenna spacing on Earth or in orbit need to be increased in order to still satisfy (4.46). This required adjustment is shown in Figure 4.8 with respect to d_{E}. The curves represent the graphical example of Figure 4.7b (earth station ULA is rotated by δ_{E}, $\delta_{\mathrm{s}} = \phi_{\mathrm{E}} = \triangle\theta = 0°$ are fixed, earth station ULA located at sub-satellite point). For both curves $\alpha = \beta = 0$ is assumed and, thus, the *array reduction factor* becomes $a_{rf} = \left|\psi/\triangle r + 0.21\alpha\beta/\triangle r^3\right| = |\psi/\triangle r|$, as shown on the upper x-axis.

The lower x-axis shows values of $0 \leq \delta \leq 80°$, because for $\delta_{\mathrm{E}} \to 90°$ all curves tend to infinity since $a_{rf} \to 0$. In this case a keyhole array configuration is obtained and the required antenna spacing becomes infinity. For angles around 0°, comparably large angular ranges of δ_{E} are allowed for which the optimal spacing d_{E} remains approximately constant. This is due to the fact that the increment of d_{E} relates to the cosine of the respective angles. Taking the blue curve for $d_{\mathrm{s}} = 6\,\mathrm{m}$ as an example and assuming $\delta_{\mathrm{E}} = 30°$, the optimal d_{E} has to be increased only by about 7 km compared to the minimum value of 50 km at $\delta_{\mathrm{E}} = 0°$ because $1/|\psi| \cdot d_{\mathrm{E}} = 1/0.87 \cdot 50\,\mathrm{km} = 57\,\mathrm{km}$. The rotation of $\delta_{\mathrm{E}} = 30°$ results in a significant displacement of the earth station antennas by 12.5 km to the North and to the South. If the antenna

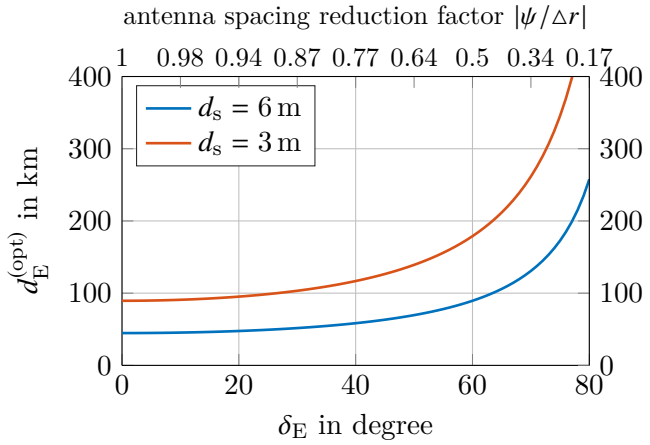

Figure 4.8.: Optimal antenna spacing $d_E^{(opt)}$ according to (4.46) as a function of δ_E, $M = Z = 2$, $v = 1$, $\delta_s = \phi_E = 0°$ and $f = 20\,\text{GHz}$.

spacings in orbit are small, large displacements of the earth station antennas in the range of several kilometers are possible without the need to adapt the optimal antenna array geometry.

4.4.4. Displacement of the Antenna Arrays

4.4.4.1. Different Locations of the Ground Antenna Array

Once an optimal antenna spacing has been found, huge displacements of the ground antenna array are possible without significant degradations of C_{opt}. Any displacement of the array with respect to θ_E and ϕ_E lead to a variation of a_{rf}, as defined in (4.48). Denoting this variation by $\triangle a_{rf}$, the parameter $\varepsilon_{r_{\text{diff}}}$ is given by

$$\varepsilon_{r_{\text{diff}}} = \frac{v d_E^{(opt)} d_s^{(opt)} / r_{\min} \cdot (a_{rf} + \triangle a_{rf}) - v \cdot \lambda/V}{\lambda/V} = v \frac{\triangle a_{rf}}{a_{rf}}. \tag{4.49}$$

Simulation results of $|\varepsilon_{r_{\text{diff}}}|$ shown as equal contour lines are provided in Figure 4.9. The earth station array is displaced in longitude and latitude from the optimal values θ_E and ϕ_E while the orientation δ_E of the array is fixed.

If $a_{rf} = 1$ (Figure 4.9a), a shift of ±10° in longitude, for example, results in a very small value of only $|\varepsilon_{r_{\text{diff}}}| = 3 \times 10^{-2}$. With respect to movements in the North-South direction, the deviation $\varepsilon_{r_{\text{diff}}}$ is even less sensitive because the antennas are all aligned in East-West direction. Whereas movements from East to West affect the *relevant antenna spacing*, movements from North to South increase $r = r_{\min} \cdot \triangle r$ only. Recall that $a_{rf} = f(\triangle r)$ according to (4.48), where $\triangle r$, defined in (4.36), denotes the increase of the minimum distance $r_{\min}$ if the earth station array is not

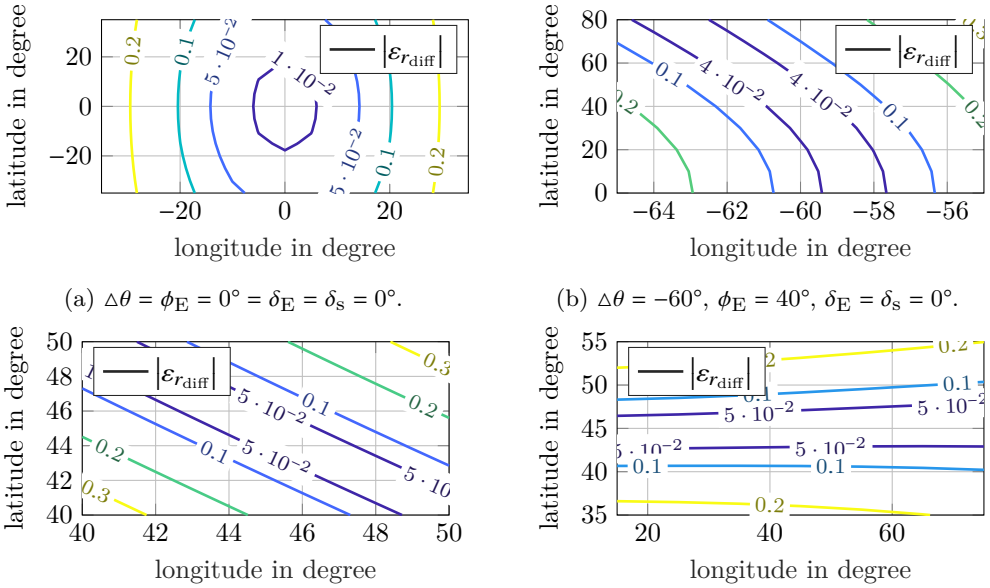

(a) $\triangle\theta = \phi_{\text{E}} = 0° = \delta_{\text{E}} = \delta_{\text{s}} = 0°$.

(b) $\triangle\theta = -60°$, $\phi_{\text{E}} = 40°$, $\delta_{\text{E}} = \delta_{\text{s}} = 0°$.

(c) $\triangle\theta = \phi_{\text{E}} = \delta_{\text{E}} = \delta_{\text{s}} = 45°$.

(d) $\triangle\theta = \phi_{\text{E}} = 45°$, $\delta_{\text{E}} = \delta_{\text{s}} = 90°$.

Figure 4.9.: Deviation $\varepsilon_{r_{\text{diff}}}$ from the optimal antenna arrangement due to displacements of the ground antenna array in longitude and latitude (optimal parameter setup is given in the caption, resulting in $a_{rf} = 1$ (a), $a_{rf} = 0.4$ (b), $a_{rf} = 0.3$ (c), and $a_{rf} = 0.6$ (d)).

at the sub-satellite point. Similar results are observed in Figure 4.9d for the case of North-to-South aligned antenna arrays ($\delta_{\text{E}} = \delta_{\text{s}} = 90°$).

The gradient of $\varepsilon_{r_{\text{diff}}}$ is increased if the relative difference in longitude and the latitude is increased (Figure 4.9b and 4.9c). However, a shift of ±2° in longitude (equivalent to ±160 km at 45° N latitude) is still possible for $|\varepsilon_{r_{\text{diff}}}| \leq 0.1$. The reason for the generally small values of $|\varepsilon_{r_{\text{diff}}}|$ is that a_{rf} varies with the cosine of the angles ϕ_{E} and θ_{E}. An increase or decrease of ϕ_{E} or θ_{E} by 2° only slightly changes the value of a_{rf} and, therefore, of $\triangle a_{rf}$. The slope of the cosine function is maximum for an angle of 45°. Hence, $\varepsilon_{r_{\text{diff}}}$ is most sensitive if the earth station array has been optimized for a geographical position at $\triangle\theta = \phi_{\text{E}} = 45°$ (see Figure 4.9c). Taking the value of $|\varepsilon_{r_{\text{diff}}}| = 0.1$ into Figure 4.3b (blue solid curve), the optimal capacity is only degraded by 0.4 %, i.e. $\triangle C = 0.996$ is still achieved.

In all cases, huge displacements of the earth station array in longitude and latitude in the range of several tens of kilometers are possible and still close-to-optimal capacity values can be obtained. This provides a high flexibility in the choice of the final location of the earth station array, which can be used to consider practical constraints such as the local terrain or the borders of a country that prevent to exactly place the antennas at its optimal location.

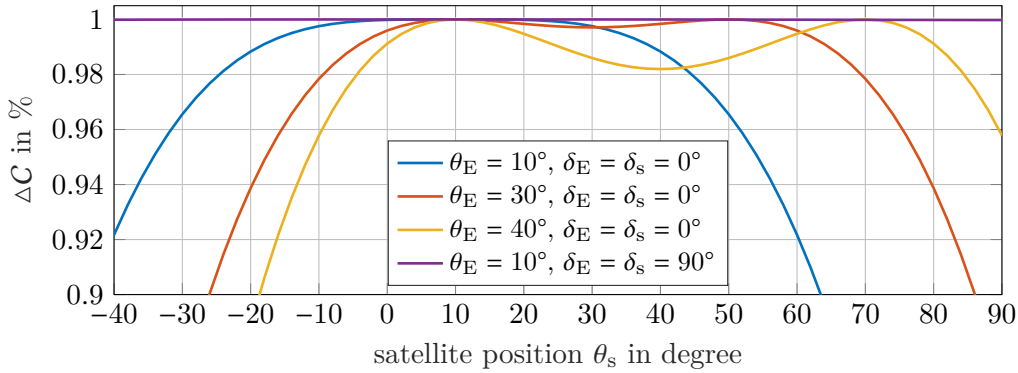

Figure 4.10.: Capacity degradation due to satellite movements to a new orbital position (initial orbit position at $\theta_s = 10°$).

4.4.4.2. Changing the Orbit Position of the Satellite

Once a MIMO ground station has been installed, the operator might be interested in using different orbital locations with the same ground antenna installation. If the MIMO satellite changes the orbit position, the relative longitude $\triangle\theta$ deviates from its initial value which the system has been optimized for. The resulting deviation $\varepsilon_{r_{\text{diff}}}$ from the optimal antenna arrangement can again be analyzed by means of (4.49) because a variation of $\triangle\theta$ only affects a_{rf}.

As already discussed in Figure 4.9, the actual deviation of $\varepsilon_{r_{\text{diff}}}$ from zero and, as a consequence, the capacity degradation $\triangle C$ strongly depend on the initial parameter configuration. The results of $\triangle C$ versus satellite movements are shown in Figure 4.10. All curves apply to a 2×2 MIMO satellite link at a receive SNR of $\rho_{r,\text{dB}} = 13\,\text{dB}$. Two generally different cases are considered as follows:

Case 1: $\delta_s = \delta_E = 0°$. The capacity degrades because the *relevant antenna spacing* reduces if the satellite is moved from its nominal orbit position at $\theta_s = 10°$. The severity of the degradation depends on the relative longitude $\triangle\theta$ at which the antenna arrangement has been optimized. If $\triangle\theta = 0°$ (blue curve), $\triangle C$ is only slightly reduced when the satellite is moved and a huge part of the geostationary arc can be used (e.g. ±40° around the initial orbital location while $\triangle C \geq 97\,\%$). If the initial relative longitude differs from zero, the usable geostationary arc can be further increased, e.g. between $-15° \leq \theta_s \leq 75°$ (red curve) and between $-10° \leq \theta_s \leq 90°$ (yellow curve) while $\triangle C \geq 96\,\%$.

Case 2: $\delta_s = \delta_E = 90°$. In this case, the entire visible geostationary arc can be used without a significant capacity degradation (purple curve) because the *relevant antenna spacing* does not change. Assuming the antennas can be oriented from North to South on the earth deck of the satellite ($\delta_s = 90°$), this con-

figuration provides the highest flexibility with regard to later changes of the orbit position.

A very large part of the GEO arc can generally be used without a significant capacity degradation. Once an optimal ground antenna setup has been implemented, it can be used for a wide range of satellite positions. This is an important result as the presented MIMO approach does not impose a flexibility disadvantage to the system.

4.5. Channel Capacity versus Antenna Spacing

A deviation from the optimal antenna spacing $d_{\mathrm{E}}^{(\mathrm{opt})}$ on the ground directly affects the *relevant antenna spacing*. From condition (4.46) it is already clear that a variation of $d_{\mathrm{E}}^{(\mathrm{opt})}$ by $\triangle d_{\mathrm{E}}$ linearly increases or decreases r_{diff}. The sensitivity of the channel capacity with respect to such deviations strongly depends on the minimum spacing $d_{\mathrm{E}}^{(\mathrm{opt})}$ on the ground. The relative error in the optimal antenna array geometry derived around the smallest optimal spacing $d_{\mathrm{E}}^{(\mathrm{opt})}$ is calculated as

$$\varepsilon_{r_{\mathrm{diff}}} = \frac{v\left(d_{\mathrm{E}}^{(\mathrm{opt})} + \triangle d_{\mathrm{E}}\right) d_{\mathrm{s}}^{(\mathrm{opt})}/r_{\min} \cdot a_{rf} - v \cdot \lambda/V}{\lambda/V} = v\frac{\triangle d_{\mathrm{E}}}{d_{\mathrm{E}}^{(\mathrm{opt})}}, \tag{4.50}$$

with $\triangle d_{\mathrm{E}}$ being the deviation from the optimal antenna spacing on the ground. Hence, the smaller the optimal spacing on the ground for $v = 1$, the larger is $\varepsilon_{r_{\mathrm{diff}}}$ for the same displacement $\triangle d_{\mathrm{E}}$.

4.5.1. Capacity Analysis Assuming Isotropic Antennas

To analyze the effect of varying the antenna spacing on C_{opt}, let first consider the case of ideally isotropic antennas. This way, any variation of C can be solely dedicated to phase variations in $\mathbf{H}$ and are not combined with amplitude variations as a result of depointing from directional antenna patterns. The latter will later be discussed in Section 4.5.3.

4.5.1.1. Single-Satellite with Two Antennas

To show the degradation of the MIMO capacity if the ground antennas are not optimally spaced, simulation results of C as a function of d_{E} are shown in Fig. 4.11. The curves apply to a 2×2 downlink at a Ka-band carrier frequency of 20 GHz. The antenna arrays are in broadside and the earth station ULA is at the sub-satellite point, i.e. $\delta_{\mathrm{E}} = \delta_{\mathrm{s}} = \phi_{\mathrm{E}} = \triangle\theta = 0°$. A fixed receive SNR of $\rho_{r,\mathrm{dB}} = 13\,\mathrm{dB}$ is assumed.

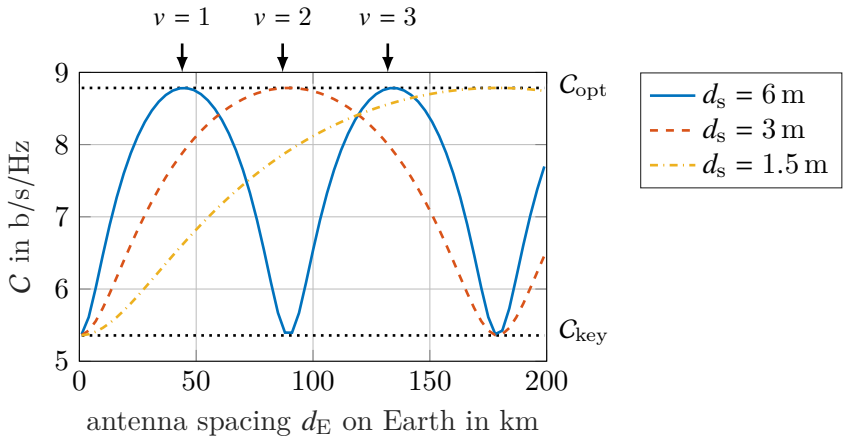

Figure 4.11.: Channel capacity as a function of earth station antenna spacing d_E for various antenna spacing d_s on the satellite (single-satellite application).

All curves show the expected periodic behavior. Each capacity maximum corresponds to one particular value of ν. For example, the first and second maxima of the blue solid curve at approximately 44.8 km and 134.4 km correspond to $\nu = 1$ and $\nu = 3$, respectively. The keyhole capacity is obtained for $\nu = 2$ at 89.6 km because in this case ν is a multiple of $V = 2$. A large deviation of the optimal spacing $d_E^{(opt)}$ on Earth is possible without a significant loss of C_{opt}. The curves reveal that for small antenna spacings in orbit and large spacings on the ground very large deviations even in the kilometer-range are possible and still close-to-maximum capacity values are obtained.

4.5.1.2. Two Satellites at Different Orbit Positions

In Figure 4.12 the situation is now reversed and the channel capacity is computed for the case of a large spacing in orbit and a small spacing $d_E^{(opt)}$ on the ground. Different satellite spacings of 1°, 2° and 3° are considered.

Since the spacing in orbit is much larger compared to the single-satellite case, the minimum required spacing on Earth is now in the decimeter range (see Figure 4.6 again). The first capacity maximum for the curve of $\triangle\theta_s = 3°$ is achieved for approximately $d_E^{(opt)} = 21$ cm. As a consequence, the required positioning accuracy on the ground must be increased, and the antennas must now be positioned within a few centimeters. Taking the blue curve for $\triangle\theta_s = 3°$ as an example, only about $\triangle d_E = \pm 8$ cm around the optimal spacing are now allowed in order to still achieve approximately 95 % of C_{opt}.

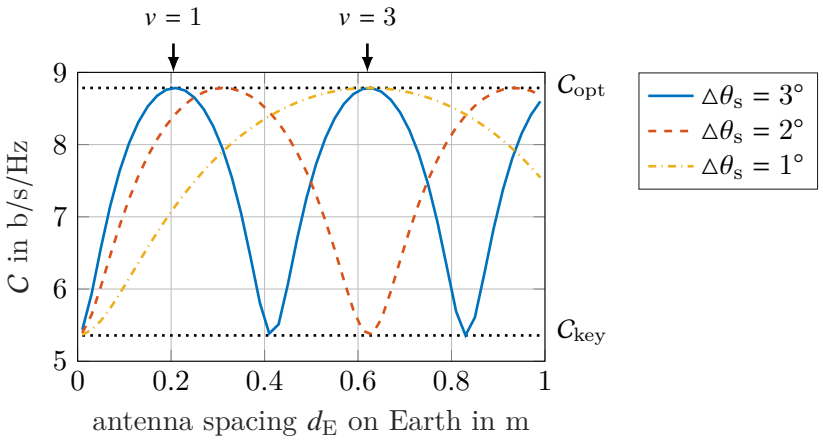

Figure 4.12.: Channel capacity as a function of earth station antenna spacing d_E for various orbital spacings $\Delta\theta_s$ between two MIMO satellites (multiple-satellites application).

4.5.1.3. Single-Satellite with More than two Antennas

Simulation results of $\Delta C = C/C_{opt}$ for different antenna numbers at each link end are provided in Figure 4.13. A 2×2 MIMO satellite downlink is now compared to a MIMO link with three, four and five antennas at each side. Moreover, the normalized eigenvalues $\gamma_w/|a|^2$ of the 4×4 MIMO link are additionally provided in the lower part of the figure. A fixed satellite antenna spacing of $d_s = 2.5\,\text{m}$ is assumed for all considered cases. The remaining simulation parameters are equal to those of Figure 4.11. The shown values of the parameter v and its location on the x-axis correspond to the 4×4 MIMO link. In particular, $vd_E = 1 \cdot 54\,\text{km}$ and $vd_E = 3 \cdot 54\,\text{km} = 162\,\text{km}$ are optimal spacings. $v = 2$ and $v = 4$ are no valid integers because two and four are both a multiple of $V = 4$. For $v = 2$ a local minimum is obtained and $v = 4$ results in the keyhole capacity.

Only the spacing $d_E = 215\,\text{km}$ (and multiples of this spacing) results in the exact keyhole channel capacity C_{key} for all curves. At this spacing, the differences between the path lengths r_{diff} in (4.17) equals the carrier wavelength λ because $v = V$, e.g. $v = 4$ in the case of the 4×4 MIMO satellite link.

While for a 2×2 MIMO channel the capacity oscillates exactly between C_{key} and C_{opt}, additional local capacity maxima and minima are observed for MIMO systems with more than two antennas at each side. Again, to obtain the global extrema of the MIMO capacity, a distinct eigenvalue profile is required. Only if all eigenvalues of $\mathbf{H}\mathbf{H}^H$ are equal, i.e. $\gamma_w = V|a|^2, 1 \leq w \leq W$, the optimum capacity C_{opt} is obtained. In contrast, all eigenvalues have to be zero except of one which is then given by $\gamma = MZ|a|^2$ in order to achieve the keyhole capacity C_{key}.

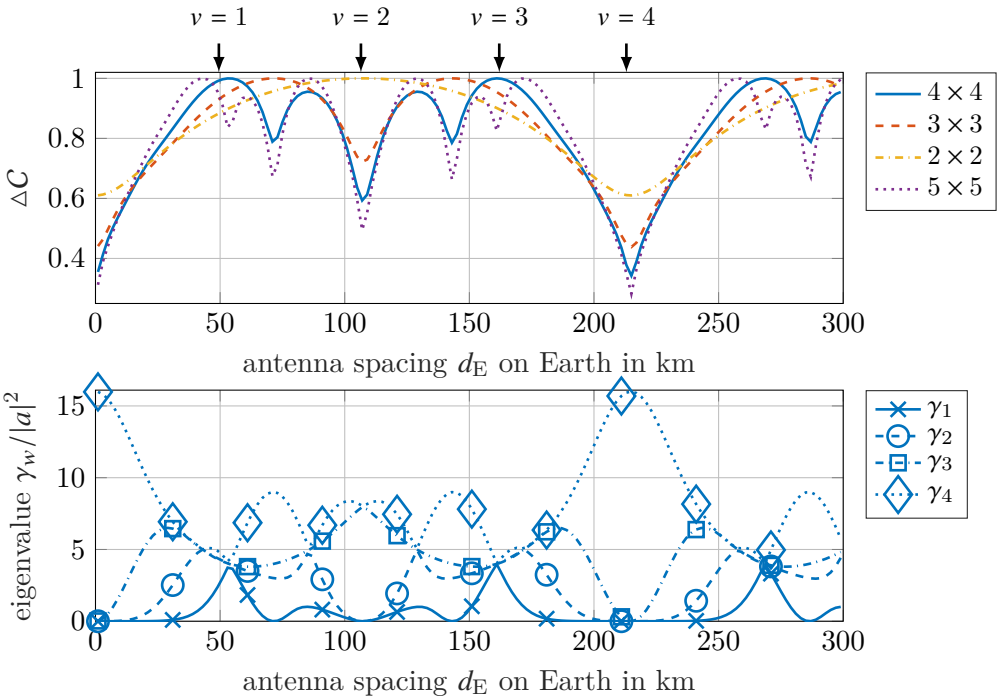

Figure 4.13.: Normalized capacity $\triangle C$ versus antenna spacing d_E for various numbers of antennas (upper sub-plot), and the four normalized eigenvalues $\gamma_w/|a|^2$ corresponding to the 4×4 MIMO channel (lower sub-plot).

This can be verified by comparing the relative capacity $\triangle C$ of the 4×4 channel with its eigenvalue profile in the lower part of Figure 4.13. While C_{opt} occurs multiple times for $M = Z > 2$ between $0\,\text{km} < d_E \leq 215\,\text{km}$, the keyhole capacity occurs only once at 215 km. The reason is that for $W > 2$ the MIMO channel provides more than two eigenvalues, and the possibilities to form a particular eigenvalue profile are increased. Consider the 4×4 channel at $vd_E = 2\cdot54\,\text{km}$ as an example. Two out of four eigenvalues γ_w are zero while $\gamma_3 = \gamma_4 = 8\cdot|a|^2$, which results in a local capacity minimum. A local capacity maximum is achieved at approximately $d_E = 87\,\text{km}$. At this spacing three out of four eigenvalues are equal, i.e. $\gamma_2 = \gamma_3 = \gamma_4 = 5\cdot|a|^2$, whereas $\gamma_1 = 1$.

This can be exploited in the system design where, for example, the antenna locations are constrained by local terrain so that the exact optimal position cannot be used. It can be seen as a further degree of freedom for the design of a MIMO satellite system with more than two antennas, in which close-to-maximum capacities are sufficient. However, it has to be emphasized that, if one out of W eigenvalues is zero, the spatial multiplexing gain is reduced to $W-1$ instead of W for an orthogonal MIMO channel. Since the sum of all eigenvalues is fixed, the magnitudes of the

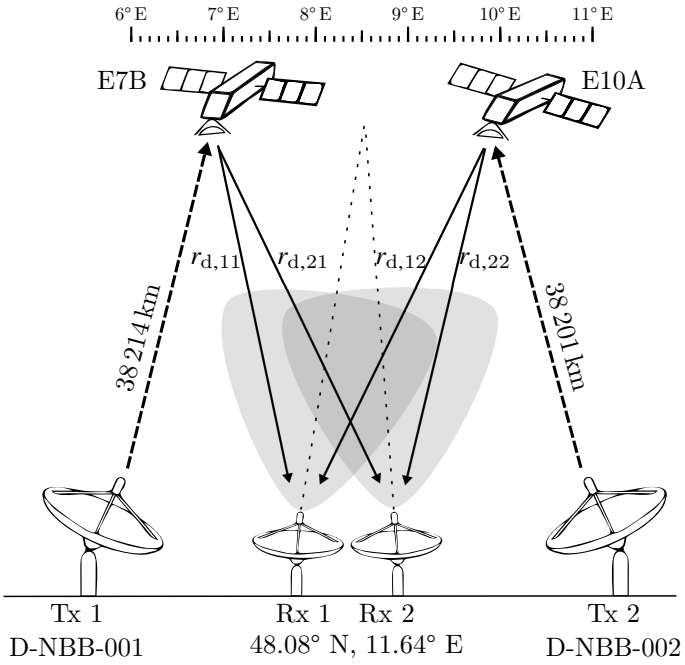

Figure 4.14.: Setup of the MIMO satellite measurement system comprising two uplink terminals Tx 1 and Tx 2, two receive terminals Rx 1 and Rx 2, and two GEO satellites at different orbital locations [HSSK16].

remaining $W - 1$ non-zero eigenvalues are increased resulting in an increased SNR at the receiver.

Although the sensitivity against ground antenna mispositioning is slightly increased for MIMO arrays with more than two antennas, large deviations from the optimal antenna location are still possible. Taking the blue curve in Figure 4.13 again as an example, $\triangle d_{\mathrm{E}} = \pm 10\,\mathrm{km}$ around the optimal spacing of 54 km are possible and approximately 95 % of C_{opt} can still be achieved.

4.5.2. Verification through Channel Measurements

To confirm the theoretical results on the optimal positioning of the MIMO antennas, a real MIMO satellite measurement campaign has been conducted. The measurement setup, the channel estimation approach and the results are thoroughly described in [HSSK16, SHK16]. The key results are repeated here again.

Since a single-satellite with two antennas, overlapping coverages in up- and downlink, the same frequency bands and polarizations is not yet available, a special setup has been developed comprising two existing satellites working in the same frequency band. In particular, the two satellites “EUTELSAT 7B” (E7B) and “EUTELSAT 10A” (E10A) have been used, which have a small frequency range in common, pro-

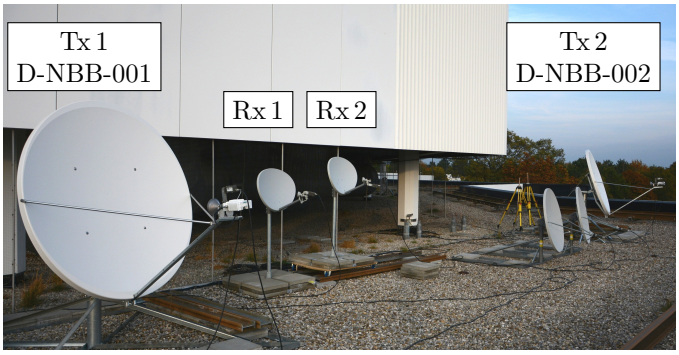

Figure 4.15.: Antenna farm showing the transmit and receive antennas of the MIMO satellite measurement system (Rx 2 is moveable on a bar).

vide an overlapping downlink coverage, use identical polarization, and are only 3° apart (see Figure 4.14). To realize a real MIMO downlink, small receive antennas with a wide main lobe were used so that both satellites can be received simultaneously while the receive antennas point directly between E7B and E10A. The antenna separation on the ground between Rx 1 and Rx 2 were adjustable (see Figure 4.15) so that the influence of the antenna geometry on the channel capacity can be verified.

To distinguish between the effect of the amplitude and of the phase on the channel capacity, and in order to identify which property of the channel matrix is responsible for a potential capacity degradation, two normalizations of the 2×2 channel matrix $\widetilde{\mathbf{H}}$ are introduced as follows:

$$\mathbf{H}_{\text{fro}} = 2\frac{\widetilde{\mathbf{H}}}{\left\|\widetilde{\mathbf{H}}\right\|_F}, \text{ and } [\mathbf{H}_{\text{norm}}]_{m,n} = \frac{h_{mn}}{|h_{mn}|} \tag{4.51}$$

where $\left\|\widetilde{\mathbf{H}}\right\|_F$ denotes the Frobenius norm of matrix $\widetilde{\mathbf{H}}$. The first normalization is physically exact in amplitude and phase. The relative differences between the amplitudes in $\widetilde{\mathbf{H}}$ remain unchanged and any potential amplitude imbalance from the measurements can be identified. The second normalization reduces the channel matrix to its phase entries and neglect all amplitudes. All potential pointing inaccuracies or even slightly different payload gains are vanished, and the calculated capacity purely depends on the path lengths between the satellite transmit antennas and the ground terminal receive antennas.

The 2×2 MIMO downlink satellite channel was measured for different receive antenna separations. By moving the receive antenna Rx 2 on the bar, the antenna spacing d_{E} has been adjusted in steps of 1 cm. At each position the channel $\hat{\mathbf{H}}$ was measured and the estimated channel capacity $\hat{C}$ using one of the normalizations of

Table 4.2.: Parameters of the MIMO downlink measurement system.

Parameter	**Value**
Carrier frequency	$f_\mathrm{d} = 12.5\,\mathrm{GHz}$
Orbit position E7B	$\theta_{\mathrm{s},1} = 7°$
Orbit position E10A	$\theta_{\mathrm{s},2} = 10°$
Latitude earth station ULA	$\phi_\mathrm{E} = 48.0796°$
Longitude earth station ULA	$\theta_\mathrm{E} = 11.6378°$
Earth station ULA orientation	$\delta_\mathrm{E} \approx -20°$

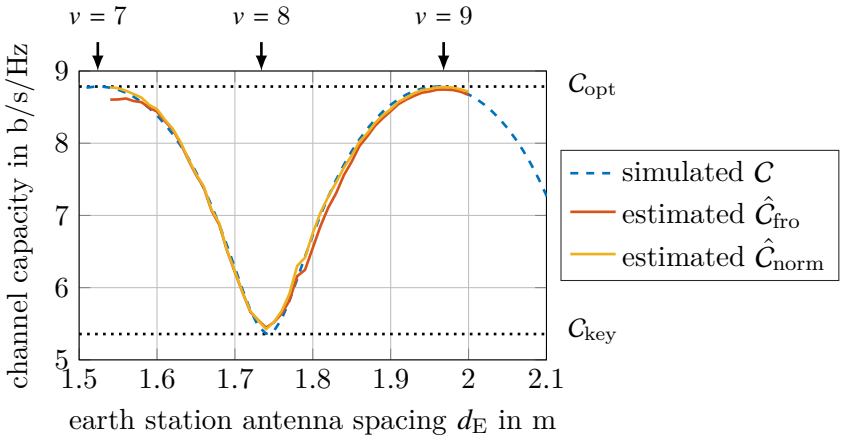

Figure 4.16.: Capacity estimation of the measured MIMO satellite channel and comparison with simulation results, assumed $\rho_{r,\mathrm{dB}}$ of 13 dB.

$\hat{\mathbf{H}}$, i.e. $\hat{\mathbf{H}}_\mathrm{fro}$ or $\hat{\mathbf{H}}_\mathrm{norm}$ according to (4.51) were calculated.

To compare the measurement results with the theoretical prediction, C has also been calculated based on the normalized 2×2 LOS channel according to (4.51) by applying the exact geographical data of the antenna positions (see Table 4.2). Using these parameters in (4.46) and solving for d_E, the optimal spacing of the receive antennas is $d_\mathrm{E}^{(\mathrm{opt})} = 21.8\,\mathrm{cm}$. Since $V = 2$, odd multiples of this spacing on Earth result in an optimal MIMO channel and we expect for such spacings to obtain a capacity maximum.

The capacity results are shown in Figure 4.16. The theoretical prediction of C is compared to the estimate $\hat{C}_\mathrm{fro}$ and $\hat{C}_\mathrm{norm}$. For all three curves an SNR of $\rho_{r,\mathrm{dB}} = 10\log_{10}(\rho_r) = 13\,\mathrm{dB}$ has been assumed.

First of all, the measurement results match very well with the theoretical simulations. All curves show the expected periodicity. Since the smallest spacing at which the capacity becomes maximal was calculated as $d_\mathrm{E}^{(\mathrm{opt})} = 21.8\,\mathrm{cm}$, the first and second maximum shown in the figure correspond to $\nu = 7$ and $\nu = 9$ and are found at $7 \cdot d_\mathrm{E}^{(\mathrm{opt})} = 1.53\,\mathrm{m}$ and $9 \cdot d_\mathrm{E}^{(\mathrm{opt})} = 1.96\,\mathrm{m}$, respectively. The keyhole channel

is obtained at a spacing of $8 \cdot d_{\mathrm{E}}^{(\mathrm{opt})} = 1.74\,\mathrm{m}$. The measured locations of the capacity maxima and minima as a function of the antenna spacing excellently match the theoretical predictions.

Comparing $\hat{C}_{\mathrm{fro}}$ with C, however, a slight degradation can be observed with respect to the maximum capacity at the point $d_{\mathrm{E}} \approx 1.55\,\mathrm{m}$. The reason for the small degradation of $\hat{C}_{\mathrm{fro}}$ with respect to the maximum is a slightly degraded link budget. At a spacing of $d_{\mathrm{E}} \approx 1.55\,\mathrm{m}$ the moveable receive antenna Rx 2 experienced a slightly higher depointing. This can be verified by comparing $\hat{C}_{\mathrm{fro}}$ with $\hat{C}_{\mathrm{norm}}$. Since the small imbalance of the link budget between the MIMO paths during the measurements is now eliminated, the slight degradation with respect to the maximum capacity has vanished. Thus, the misalignment of Rx 2 pointing not exactly at 8.5° East has been identified as the main error source for the measurement of the optimal MIMO channel[10].

Moreover, the keyhole capacity of $\hat{C}_{\mathrm{fro}}$ and of $\hat{C}_{\mathrm{norm}}$ compared to C at the point $d_{\mathrm{E}} = 1.74\,\mathrm{m}$ is a bit increased. An error analysis provided in [HSSK16] with respect to AWGN and phase noise have shown that presumably the phase noise in the measurement chain is responsible for this slightly increased capacity estimation. This effect is constraint by the measurement system. It does not lead to a correction of the theoretical model on the optimal positioning of the MIMO antennas as derived in Section 4.3. As a matter of fact, the curves in Figure 4.16 prove the predicted dependence of the channel capacity on the arrangement of the antennas.

4.5.3. Capacity Gains Considering Directional Radiation Patterns

The achievable capacity gains are now analyzed when taking the antenna patterns additionally into account. The use of directional antennas in FSS scenarios leads to further constraints in the positioning of the antennas. It turns out that especially the feasibility of multiple MIMO satellites is limited if the orbital spacings between the satellites are not sufficiently small to limit the depointing loss.

4.5.3.1. Single-Satellite Scenario

In single-satellite applications it is reasonable to assume that all the earth station antennas exactly point to the MIMO satellite. Thus, no depointing from ground-to-space needs to be considered and it follows $g_{\mathrm{d},zm}^{(\mathrm{E})} = 1, \forall\, z,m$. From space-to-ground, the coverage of a satellite antenna is usually limited to a particular geographical area, depending on the frequency band and the size of the antenna aperture. The

[10] Since no beacon at 8.5° East were available, it could not exactly guaranteed that the receive antennas perfectly point in between the two satellites at all times. Because of the movement of Rx 2 on a rail in order to adjust the antenna spacing d_{E}, small inaccuracies and variations in pointing during the measurements are unavoidable.

limited coverage of high gain satellite antennas results in an additional design constrain for the positioning of the earth station antennas. Note that this constrain does not originate from the MIMO technology itself. The receiving antenna(s) must basically *see* the transmitting antenna(s) and vice-versa, in order to achieve a sufficient link budget and to close the link with high throughput. This requirement is likewise important for conventional SISO systems as for MIMO systems.

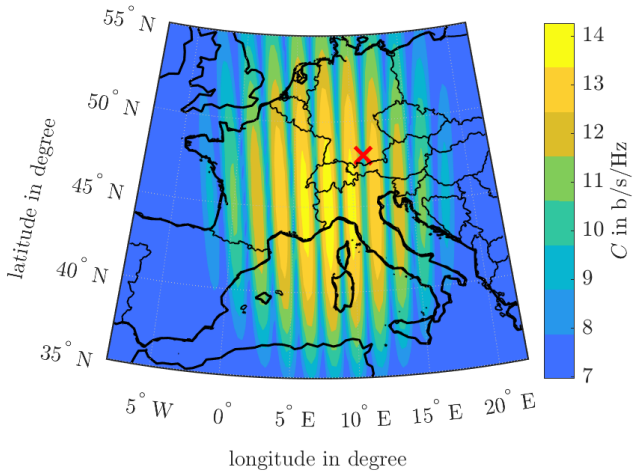

Figure 4.17.: Two-dimensional capacity contour of a 2×2 MIMO satellite scenario over the map of Europe.

In Figure 4.17, the capacity is shown as a surface plot on the map[11]. The following parameters have been used: The two satellite antennas with 1.8 m in diameter are located at $\theta_s = 10°\,\mathrm{E}$ having a spacing of $d_s = 6\,\mathrm{m}$ in the equatorial plane ($\delta_s = 0°$). They point to 45° N, 8° E.At the center of coverage (CoC), a receive SNR of $\rho_{r,\mathrm{dB}} = 23\,\mathrm{dB}$ at 12 GHz is achieved. The first ground station antenna is fixed at 48° N, 11° E (marked by a red cross in Figure 4.17). The second ground station antenna has been moved across the map and C was calculated for each location.

The oscillation between C_{opt} and C_{key} is again observed, which confirms the one-dimensional results from Figure 4.11 and Figure 4.13. The capacity is sensitive for antenna movements in the East-West direction while from the North to the South huge distances are possible without a significant variation of C. The reason is again that the satellite ULA is oriented in the East-West direction and, therefore, ground antenna movements from North to South are *invisible* by the satellite array. High capacity values (yellow color) are only obtained in areas at which the antenna arrangement is optimal in the sense of (4.46) *and* the depointing from the satellite antennas is sufficiently small. The best position for the second antenna would be

[11] Country borders have been created using Matlab source code that is © 2015, by Chad Greene.

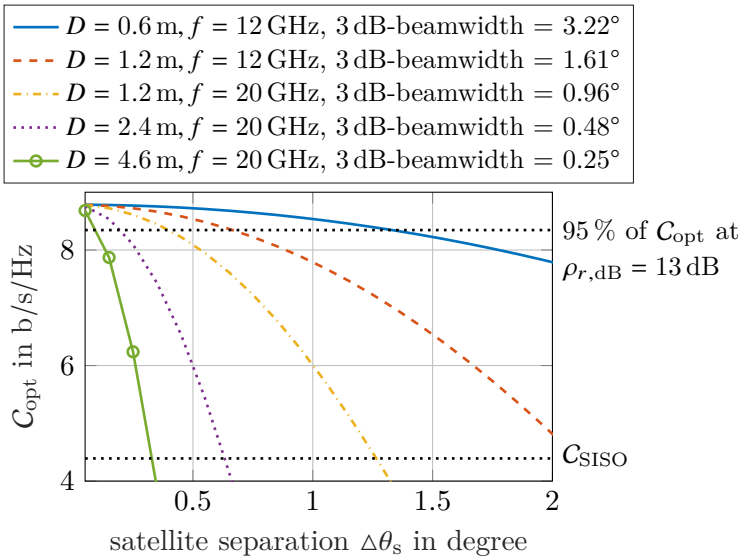

Figure 4.18.: C_{opt} as a function of $\triangle\theta_{\text{s}}$ of two MIMO satellites for various earth station antenna diameter and carrier frequencies.

in this example somewhere between southwest of France and northeast of Italy.

4.5.3.2. Two Satellites at Different Orbit Locations

In the case of multiple satellites at different orbital positions a depointing from Earth-to-space must be considered. Simulation results of C as a function of the orbital spacing $\triangle\theta_{\text{s}}$ between two satellites are shown in Figure 4.18. From space-to-Earth no depointing is assumed, i.e. $g^{(\text{s})}_{\text{d},mz} = 1,\ \forall m, z$. The results apply to a 2×2 MIMO downlink in which the two earth station antennas directly point in between the two satellites. The earth station array is located at 48° N and the relative longitude is $\triangle\theta = 0°$. The depointing loss from one earth station antenna is, therefore, equal to both satellites. Various antenna diameters and carrier frequencies are compared. The curves are based on an equal receive SNR of 13 dB at the point of boresight. The capacity maximum at $\triangle\theta_{\text{s}} = 0.01°$ is therefore equal for all curves, irrespective of the considered antenna size and frequency. In all cases an optimal antenna arrangement according to (4.46) is assumed. For increasing $\triangle\theta_{\text{s}}$, d_{E} is decreased accordingly such that $\varepsilon_{r_{\text{diff}}} = 0$ is always ensured. Hence, the y-axis shows C_{opt} according to (3.18) and the capacity decrease is purely dedicated to a reduced link budget. The results are compared to C_{SISO} according to (3.20).

As expected, the larger the antenna aperture and the higher the carrier frequency, the higher is the capacity loss for increasing $\triangle\theta_{\text{s}}$. Moderate capacity losses are only observed for antennas that have a sufficiently wide main beam. Two examples are

the 60 cm dish, a typical dish size that is installed on roof tops of housholds, and the 1.2 m antenna. The 5 % loss of C_{opt} is shown as a horizontal line. Taking this value as a lower limit, the satellite spacings must not exceed approximately 1.4° and 0.7° in the case of a 60 cm dish or a 1.2 m dish, respectively. In the Ka-band the main lobes are narrower and even 0.5° satellite spacing is too large for a 1.2 m antenna to stay above the 5 % loss of C_{opt}.

If the spacing of the satellites in orbit is too large and the antenna's main beam is too narrow, the depointing loss of the ground station antennas becomes the dominating factor. This limits the achievable MIMO capacity in the multiple-satellites scenario, even if the antennas are optimally arranged. From the simulation results it is concluded that satellite spacings of more than 1.5° are not of relevance for FSS.

Apart from the capacity loss due to depointing, the issue of ASI in the transmit mode of the ground antennas additionally constrain the practicability of this category of MIMO satellite applications. Neighboring satellite(s) in between the two MIMO satellites may suffer from interference from the ground or produce interference into the ground terminals that directly point to the adjacent satellite. This must be considered in the design of a multiple-satellites application and, in fact, further constrains the feasibility of multiple satellites at different orbital slots for FSS applications.

In contrast to FSS, this category of applications is perfectly suited for mobile satellite applications with non-directional antennas at the ground segment. Note that the land mobile satellite channel significantly differs from the channel for FSS because multipath and various shadowing-states of the LOS component must be considered [FVCC+01]. One promising application example is UHF SATCOM, as it has been proposed in [RCB16]. The applied user terminals are easy to deploy and have broad beamwwidths so that precise pointing to the satellite is not required. The terminals are able to operate with any UHF satellite that is visible in the geostationary arc. The frequency of the radiowaves is sufficiently low such that the radiowaves penetrate into buildings and foliage. This makes UHF SATCOM perfectly suited for military mobile applications and has turned UHF communications to be the workhorse of every military mission. A severe drawback is the very low spectral efficiency since the frequency spectrum cannot be reused. Strict frequency coordination is necessary to avoid the interference with UHF satellites from other constellations. The MIMO approach seems to be a very promising solution since the idea is based on a full frequency reuse and the gain requires sufficient interference from the involved antennas [RCB16]. Measurements of the UHF MIMO satellite channel reported in [HSK17, SVK+17] have shown that the channel capacity can be significantly increased. However, the UHF band is not in the scope of this work and this applications scenario is, therefore, no longer considered here.

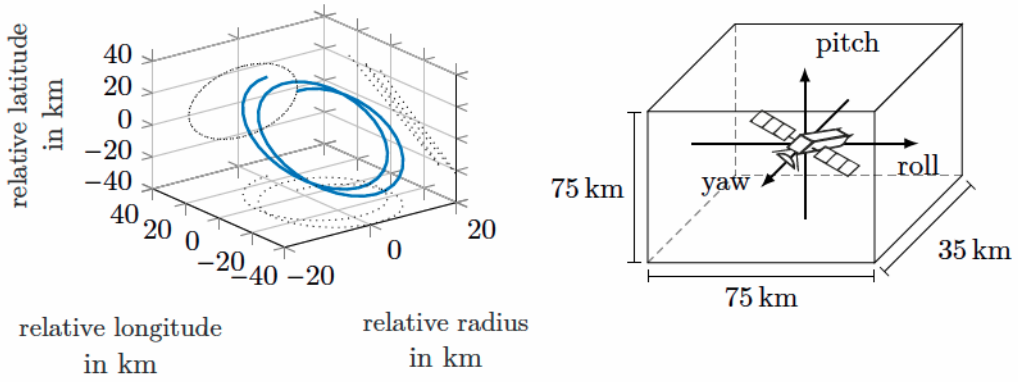

(a) Satellite motion over two sidereal days (eccentricity 3×10^{-4}, inclination 0.03°, increased semi-major axis by 1 km).

(b) Typical dimensions of a station-keeping box with yaw, roll and pitch axes of the satellite [MB09].

Figure 4.19.: Range of satellite motion in the station-keeping box.

4.6. Impact of Satellite Movements

4.6.1. Range of Motion in the Station-Keeping Box

In practice it is impossible to place a satellite exactly in an ideal geostationary orbit and to keep the satellite fixed in this orbit due to inaccuracies in the thrusters, uncertainties in the tracking system and orbit perturbations. As a result, the inclination and the eccentricity are no longer zero, even if they are very small, and the satellite follows not exactly a circular orbit with a constant ideal radius of R_o = 42 164.2 km. These small deviations from the exact Kepler orbit cause an apparent movement of the spacecraft around its ideal position (see Figure 4.19a). As a result of a non-zero inclination and a non-zero eccentricity the longitude, the latitude and the orbit radius of the satellite oscillate as a function of time (also known as libration). In addition, a small deviation from the ideal semi-major axis lead to a drift of the satellite to the East (if the semi-major axis is smaller than R_o) or to the West (if the semi-major axis is larger than R_o).

The amplitude of the overall orbital motion of the satellite is specified by the station-keeping box (see Figure 4.19b), whose limits are usually ±0.05° in longitude and latitude and 4×10^{-4} in eccentricity [MB09]. The attitude of the satellite is described by a local coordinate system with the center of mass in its origin. Typical ranges of rotational shifts are ±0.2° for the yaw axis and ±0.05° for the roll axis and the pitch axis [MB09].

Table 4.3.: Deviations from optimal antenna array geometry due to satellite movements (assuming the maximum dimensions of station-keeping box)

Type of satellite motion	$\lvert\varepsilon_{r_{\text{diff}}}\rvert$
radial shift of ±17.5 km	4.9×10^{-4}
longitudinal shift of ±32.5 km	9.5×10^{-7}
latitudinal shift of ±32.5 km	9.5×10^{-7}
rotation of ±0.2° in yaw axis	6.1×10^{-6}
rotation of ±0.05° in roll axis	3.8×10^{-7}
rotation of ±0.05° in pitch axis	3.8×10^{-7}

4.6.2. Capacity Analysis for Single-Satellite Applications

In the single-satellite case, capacity degradations due to changes of the satellite's attitude and movements around its ideal position can generally be neglected [KSO+08], [SKO+09]. The deviation of r_{diff} from the optimal value $v \cdot \lambda/V$ is too small in order to observe a significant effect on C_{opt}. Since the MIMO antennas are fixed with the satellite, movements of the satellite and variations of the attitude only slightly change the orientation of the satellite array. The antenna spacing d_{s} remain constant.

Results of $\varepsilon_{r_{\text{diff}}}$ due to satellite movements within the ranges as defined by the station-keeping box in Figure 4.19b are shown in Table 4.3. The values of $\varepsilon_{r_{\text{diff}}}$ are computed based on the following parameter setup:

antenna number:	$M = Z = 2$,	ground location:	$\theta_{\text{E}} = \phi_{\text{E}} = 0°$
carrier frequency:	$f = 20\,\text{GHz}$,	array orientation:	broadside, $\delta_{\text{E}} = \delta_{\text{s}} = 0°$
satellite position:	$\theta_{\text{s}} = 0°$,	antenna spacing:	$d_{\text{s}} = 3\,\text{m}$, $d_{\text{E}} = 89.5\,\text{km}$

The values in Table 4.3 confirm that, in the case of a single-satellite, satellite movements in the station-keeping box and changes of the satellite's attitude can be neglected as a potential source of capacity degradation.

4.6.3. Multiple-Satellites and Co-Located Satellites Applications

4.6.3.1. Type of Station-Keeping Strategy

If the antennas are deployed on different spacecrafts,[12] independent movements of the satellites directly affect the antenna spacing and array geometry in orbit. The

[12] The relative motion of the satellites with respect to each other is similar for both the multiple-satellites scenario and the co-located satellites scenario. Both categories of application are treated here together.

extent of this relative motion depends on the type of station-keeping that is applied to keep the satellites in the desired orbits. Basically the following two types can be distinguished [Soo94, Li14]:

a) *Uncoordinated station-keeping:* Each spacecraft is operated independently and is presumably handled by different control centers.
b) *Coordinated station-keeping:* The station-keeping and orbit control of each satellite depend on each other and are jointly performed by one operator in a single control center.

Simulation results will later show that an important target is to maintain the geometry between the satellites, which ultimately requires *coordinated station-keeping* in order to achieve a constantly high capacity gain. This objective is also treated as a formation flying or cluster geometry maintenance problem in the literature, e.g. in the context of distributed space systems [WN12]. Several possibilities already exist [Kaw90, MAG+99, dB17], one example is the master/slave (or leader/follower) station-keeping approach [dB17].

4.6.3.2. Modeling the Satellite Movements

The following analysis has partly been published in [SK19] investigating the MIMO capacity of two co-located satellites in longitude separation. The method can similarly be used to analyze scenarios with multiple satellites on different orbital slots. The key results and the applied approach is therefore summarized here again.

To analyze the impact of satellite movements on C_{opt}, the model in Section 4.3.1.2 is extended to consider small inclination and eccentricity values as well as deviations from $R_o = 42\,164.2\,\text{km}$. The approach relies on the method of linearized relative satellite motion [Soo94]. The three-dimensional Cartesian position vector of the z-th satellite is then given as

$$\mathbf{a}_{\text{s},z} = \left[R_z \cos\phi_{\text{s},z} \cos\theta_{\text{s},z},\ R_z \cos\phi_{\text{s},z} \sin\theta_{\text{s},z},\ R_z \sin\phi_{\text{s},z}\right]^{\text{T}}. \tag{4.52}$$

The parameters $\phi_{\text{s},z}$, $\theta_{\text{s},z}$ and R_z denote the latitude, the longitude and the orbit radius, respectively, which are now time-varying parameters. They are given as [MB09, Har95]

$$\phi_{\text{s},z} = i_z^x \sin\left(\Psi\left(t - t_0\right)\right) - i_z^y \cos\left(\Psi\left(t - t_0\right)\right), \tag{4.53}$$

$$\theta_{\text{s},z} = \theta_{0,z} - 3/2 \frac{\triangle R_z}{R_o} \Psi\left(t - t_0\right) + 2e_z^x \sin\left(\Psi\left(t - t_0\right)\right) - 2e_z^y \cos\left(\Psi\left(t - t_0\right)\right), \tag{4.54}$$

$$R_z = R_o + \triangle R_z - R_o \left[e_z^x \cos\left(\Psi\left(t - t_0\right)\right) + e_z^y \sin\left(\Psi\left(t - t_0\right)\right)\right], \tag{4.55}$$

with $\Psi = 7.292\,115 \times 10^{-5}\,\text{rad/s}$ being the angular velocity of the Earth. The pa-

rameters $\theta_{0,z}$ and $\triangle R_z$ denote the mean longitude at the epoch t_0 and the deviation of the actual semi-major axis from the ideal value R_o, respectively. Moreover, $\mathbf{i}_z = \left[i_z^x, i_z^y\right]^{\mathrm{T}}$ and $\mathbf{e}_z = \left[e_z^x, e_z^y\right]^{\mathrm{T}}$ denote the two-dimensional inclination and eccentricity vectors, respectively. The six parameters $\mathbf{i}_z$, $\mathbf{e}_z$, $\triangle R_z$, and $\theta_{0,z}$ are known as equinoctial elements and they fully define the time-varying position of the z-th satellite in orbit. The relative motion of two satellites with respect to each other can be described by the difference between their equinoctial elements, i.e.

$$\triangle\theta_0 = \theta_{0,k} - \theta_{0,l},\ \triangle R = \triangle R_k - \triangle R_l,\ \triangle\mathbf{e} = \mathbf{e}_k - \mathbf{e}_l,\ \triangle\mathbf{i} = \mathbf{i}_k - \mathbf{i}_l, \tag{4.56}$$

with $k, l = 1, \ldots, Z$, $k \neq l$. The total distance between two satellites is calculated by $d_{\mathrm{s},kl} = \left\|\mathbf{a}_{\mathrm{s},k} - \mathbf{a}_{\mathrm{s},l}\right\|$.

The accuracy with which the satellites can be maintained in its GEO is limited because of the following two main reasons: Firstly, estimation errors of the orbit determination system lead to inaccurate orbit parameters of the satellites. The approximate values are then the basis to determine station-keeping and cluster-keeping maneuvers. Secondly, inaccuracies of the propulsion system must be considered, which result in small positioning errors of the spacecrafts after a maneuver. To account for small inaccuracies in the positioning of the satellites, normally distributed random errors on the equinoctial elements of the z-th satellite are introduced as follows [Soo94], [Har95]:

$$\begin{aligned}
\mathbf{e}_z &= \bar{\mathbf{e}}_z + \boldsymbol{\varepsilon}_{e,z},\ \boldsymbol{\varepsilon}_{e,z} \sim \mathcal{N}_2\left([0,0]^{\mathrm{T}}, \sigma_e^2\mathbf{I}_2\right)\ \forall\, z,\\
\mathbf{i}_z &= \bar{\mathbf{i}}_z + \boldsymbol{\varepsilon}_{i,z},\ \boldsymbol{\varepsilon}_{i,z} \sim \mathcal{N}_2\left([0,0]^{\mathrm{T}}, \sigma_i^2\mathbf{I}_2\right)\ \forall\, z,\\
\theta_{0,z} &= \bar{\theta}_{0,z} + \varepsilon_{\theta,z},\ \varepsilon_{\theta,z} \sim \mathcal{N}\left(0, \sigma_\theta^2\right)\ \forall\, z,\\
\triangle R_z &= \triangle\bar{R}_z + \varepsilon_{\triangle a,z},\ \varepsilon_{\triangle a,z} \sim \mathcal{N}\left(0, \sigma_{\triangle a}^2\right)\ \forall\, z,
\end{aligned} \tag{4.57}$$

where $\bar{\mathbf{e}}_z$, $\bar{\mathbf{i}}_z$, $\bar{\theta}_{0,z}$ and $\triangle\bar{R}_z$ denote the exact values of the eccentricity vector, the inclination vector, the mean longitude and the deviation of the semi-major axis, respectively. The parameter $\boldsymbol{\varepsilon}$ denotes the random variable with zero mean and standard deviation σ, where a proper subscript is chosen to distinguish the errors between the six equinoctial elements. Since neither a particular orbit determination system is considered nor a specific type of thrusters is presumed, all random variables are assumed to be mutually independent.

4.6.3.3. Capacity Analysis Assuming Ideal Orbit Elements

The impact of independent motion of two satellites on C_{opt} is analyzed first assuming ideal orbit elements, i.e. the errors $\boldsymbol{\varepsilon}$ as defined in (4.57) are zero. The parameter

Table 4.4.: Parameter setup to analyze capacity degradations of the multiple/co-located-satellites scenario

Parameter		**Value**
A) General Parameters:	Number of antennas	$N = Z = M = 2$
	Total receive SNR	19.5 dB
	Up-/downlink frequency	$f_\mathrm{u} = 14\,\mathrm{GHz},\ f_\mathrm{d} = 12.5\,\mathrm{GHz}$
B) Transmit Station:	ULA center $(\phi_\mathrm{E}, \theta_\mathrm{E})$	48° N, 13° E
	ULA orientation	$\delta_\mathrm{E} = 0°$
	antenna spacing	$d_\mathrm{E}^{(\mathrm{opt})} = 10.75\,\mathrm{m}$
	uplink EIRP	$P_t = 80\,\mathrm{dBW}$
C) Satellite:	location cluster center	$\theta_\mathrm{s} = 13°\,\mathrm{E}$
	satellite spacing	$\triangle\theta_\mathrm{s} = 0.05°$
	payload gain	$\lvert a_\mathrm{s}\rvert^2 = 206\,\mathrm{dB}$
D) Receive Station:	ULA center $(\phi_\mathrm{E}, \theta_\mathrm{E})$	36° N, 67° E
	ULA orientation	$\delta_\mathrm{E} = 0°$
	antenna spacing	$d_\mathrm{E}^{(\mathrm{opt})} = 25.95\,\mathrm{m}$

setup is summarized in Table 4.4. Note that at t_0 the antenna arrangements in the uplink and downlink are optimal. The optimal antenna spacings have been calculated using (4.46). Thus, at the beginning of a station-keeping cycle (time $t = t_0$), the up- and downlink channels $\widetilde{\mathbf{H}}_\mathrm{u}$ and $\widetilde{\mathbf{H}}_\mathrm{d}$ are optimal and provide the maximal number of two equally strong sub-channels.

Simulation results over five sidereal days are summarized in Figure 4.20. Figure 4.20a shows $\triangle C$ as defined in (4.20) for three different equinoctial element setups. Figure 4.20b illustrates the satellite spacing for the particular setup $\|\triangle\mathbf{e}\| = 0, \|\triangle\mathbf{i}\| = 0.0012$, which corresponds to the blue capacity curve in Figure 4.20a.

In all three cases of Figure 4.20a, the mean longitude drift between both satellites differs because of $\triangle R_1 = 0.5\,\mathrm{km}, \triangle R_2 = 0\,\mathrm{km}$. Hence, satellite one performs a drift to the West while the mean longitude of the second satellite remains constant resulting in an increased longitude spacing over time (see also the dashed curve in the lower plot of Figure 4.20b). The mean capacity decreases for increasing t because the channel in the uplink and the downlink are no longer optimal. The higher the value of $\triangle R = |\triangle R_2 - \triangle R_1|$, the steeper the slope of $R_o\left(\theta_{\mathrm{s},2} - \theta_{\mathrm{s},1}\right)$, and the more rapidly the capacity degrades (not shown in the figure).

Moreover, the capacity oscillates if either the inclination vectors (blue curve) or the eccentricity vectors (red curve) or both of the individual orbits are not in parallel because the geometry between the satellites fluctuates (please also refer to Figure 4.20b, in particular the variation of the total separation $d_{\mathrm{s},21}$). Station-

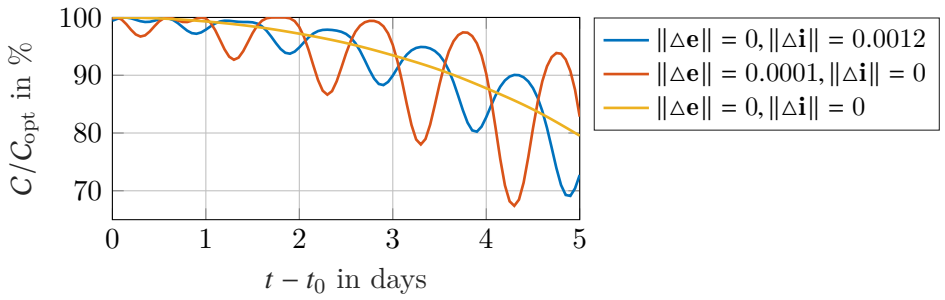

(a) Normalized capacity C/C_{opt}.

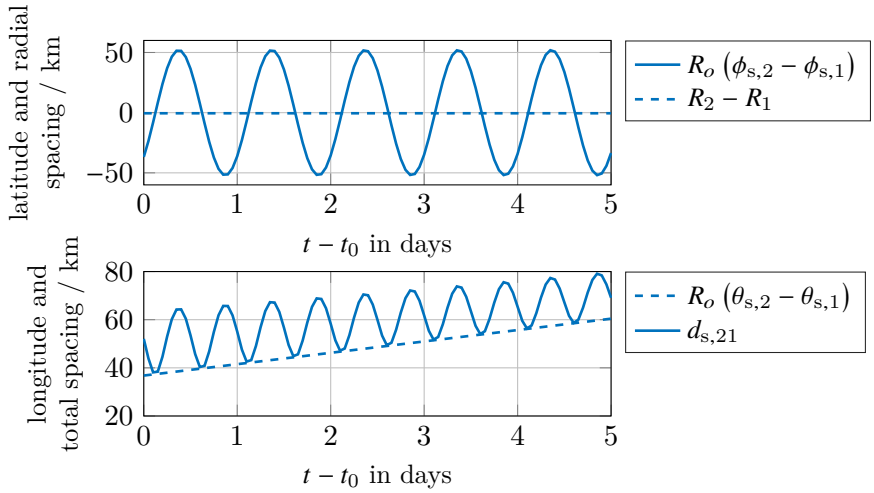

(b) Satellite spacing for the case $\|\triangle\mathbf{e}\| = 0, \|\triangle\mathbf{i}\| = 0.0012$.

Figure 4.20.: MIMO capacity (a) of $Z = 2$ co-located satellites in longitude separation for various inclination and eccentricity vectors; satellite separation (b) for the case of parallel eccentricity and orthogonal inclination vectors; $\triangle\theta_0 = 0.05°, i_1 = i_2 = 0.05°, e_1 = e_2 = 0.0002, \triangle R_1 = 0.5\,\text{km}, \triangle R_2 = 0\,\text{km}$

keeping of MIMO satellites must therefore target for correlated eccentricity and inclination vectors. In addition, the relative longitude drift must also be similar to keep the satellite spacing constant, which necessitates the implementation of a *coordinated station-keeping* strategy. This result applies to both MIMO categories of application, co-located satellites in longitude separation and multiple-satellites at different orbital slots.

4.6.3.4. Capacity Analysis Including Orbit Parameter Errors

Coordinated station-keeping is now assumed and the station-keeping maneuvers target to maintain fully correlated inclination and eccentricity vectors as well as a zero difference in the mean longitude drift rates, i.e. $\|\triangle\mathbf{e}\| = \|\triangle\mathbf{i}\| = \triangle R = 0$.

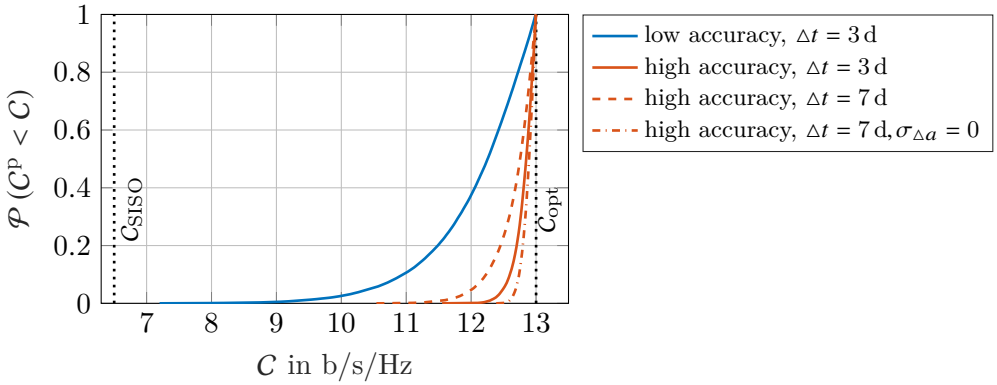

Figure 4.21.: Cumulative distribution function of C as a result of a Monte Carlo simulation.

However, due to the errors ε as introduced in (4.57), the actual differences between the equinoctial elements will not be equal to Zero.

Monte Carlo simulations have been performed assuming the following two sets of equinoctial variable errors as reported in [Soo94, Har95]:

Parameter	*high accuracy*	*low accuracy*
$3\sigma_e$	$\pm 0.9 \times 10^{-5}$	$\pm 4.5 \times 10^{-5}$
$3\sigma_i$	$\pm 0.7 \times 10^{-5}$	$\pm 3.4 \times 10^{-5}$
$3\sigma_\theta$	$\pm 0.0014°$	$\pm 0.0075°$
$3\sigma_{\triangle a}$	$\pm 100\,\mathrm{m}$	$\pm 500\,\mathrm{m}$

While the errors in the column *low accuracy* constitute a conservative assumption and can be easily achieved in practice, some additional effort (e.g. a second ranging antenna) is necessary to achieve the error levels in the column *high accuracy* [Soo94].[13]

The simulation results for both sets of error values are shown in Figure 4.21. Two durations of station-keeping maneuver cycles are considered ($\triangle t = 3\,\mathrm{d}$ and $\triangle t = 7\,\mathrm{d}$), after which potential longitude drifts are corrected. In all cases a minimum spacing of 10 km between the satellites was assured, and the satellites were always kept within the longitude deadband of ±0.05°.

[13] The actual error values can substantially differ because they strongly depend on the tracking and the thruster system (to only name a few relevant parameters, one must generally distinguish onboard vs. ground based tracking, number of tracking stations and their relative position to the satellites, electrical vs. chemical propulsion, location and number of the thrusters and related cross-coupling effects, etc.). However, the error values termed as *low accuracy* are construed as a worst case scenario [Soo94, Har95]. Current state-of-the-art technologies such as Global Positioning System (GPS) support on GEO satellites lead to much better orbit determination and station-keeping accuracies [dB17, CB94] so that the error values stated as *low accuracy* can easily be improved with manageable practical effort.

As expected, the smaller the errors of the equinoctial elements the lower is the capacity degradation. Even in the case of low positioning accuracy (blue curve), more than 11 b/s/Hz (approximately 85 % of $C_{\text{opt}} = 13$ b/s/Hz) is obtained in 90 % of all observations. Compared to the state-of-the-art SISO satellite system with $C_{\text{SISO}} = 6.5$ b/s/Hz, this constitutes a capacity gain of 1.7. If the satellite orbits can be maintained with *high accuracy*, the capacity loss is almost negligible. At least $C = 12.6$ b/s/Hz (97 % of C_{opt}) are achieved in 95 % of the time (red solid curve).

The capacity degradation depends on the station-keeping cycle $\triangle t$ after which a new longitude maneuver can be performed. Shorter cycle durations allow a more frequent correction of a deviation of $\triangle R$ from Zero (compare the red dashed curve with the red solid curve). If we set, in an ideal case, the error of the semi-major axis for both satellites to $\sigma_{\triangle a} = 0$, the mean longitude spacing remain constant over time and is no longer affected by a difference in the satellite drifts. In this case, the capacity degradation becomes independent of the longitude correction cycle (red dot-dashed curve), which motivates the implementation of a longitude station-keeping with high accuracy.

The simulation results show that for a constantly high MIMO capacity gain a coordinated station-keeping strategy is necessary that includes the maintenance of the geometry, in particular the longitudinal spacing between the satellites. This constraint for future MIMO multi-satellite systems is not seen as critical since several concepts with sufficiently high positioning accuracy and only small additionally required propellant consumption already exist. For example, the authors in [CB94] have proposed a GPS-based formation-keeping approach with which the position deviations can be maintained within a fraction of a kilometer after 40 h of small orbit control maneuvers. At the same time the additional fuel required to accurately control the satellite motion to a predetermined ephemeris is small and does not exceed 2.5 m/s per year [CB94].

4.6.3.5. Relation Between Positioning Accuracy and Satellite Spacing

It can be shown that the required accuracy to maintain the longitude spacing can be relaxed when the nominal spacing $\triangle\theta_{\text{s}}$ is increased. To this end, the deviation $\varepsilon_{r_{\text{diff}}}$ from the optimal array geometry as a function of longitude satellite motion is calculated, which is given as

$$\varepsilon_{r_{\text{diff}}} = \frac{v d_{\text{E}}^{(\text{opt})} \left(d_{\text{s}}^{(\text{opt})} + \triangle d_{\text{s}} \right) / r_{\min} \cdot a_{rf} - v \cdot \lambda / V}{\lambda / V} = v \frac{\triangle d_{\text{s}}}{d_{\text{s}}^{(\text{opt})}}. \tag{4.58}$$

The parameter $\triangle d_{\text{s}}$ denotes the deviation from the optimal spacing $d_{\text{s}}^{(\text{opt})} \approx \triangle\theta_{\text{s}} R_o$ in meter and describes the (differential) longitude movements. The value of $\triangle d_{\text{s}}$ must

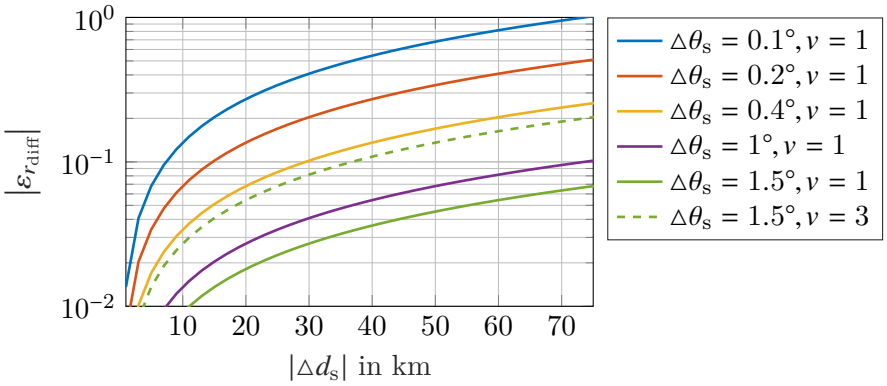

Figure 4.22.: Deviation from the optimal antenna arrangement due to independent satellite movements for various nominal orbital spacings $\triangle\theta_s$.

be decreased when $\triangle\theta_s$ is decreased for the same deviation $\varepsilon_{r_{\text{diff}}}$. In other words, the smaller $\triangle\theta_s$ the higher is the positioning accuracy. This linear dependence of $\varepsilon_{r_{\text{diff}}}$ on $\triangle\theta_s$ is intuitively clear as the same satellite movement appears small for a large satellite array and their effect is enhanced if the satellite array is small. While $\triangle\theta_s \leq 1.5°$ has been identified as an upper bound to limit SNR losses due to antenna depointing (see Section 4.5.3), equation (4.58) impose a lower limit for $\triangle\theta_s$ in dependence on $\triangle d_s$.

Second, the linear dependence of (4.58) on v clearly suggest not to make use of the periodicity of the solution (4.46). Since $d_E^{(\text{opt})}$ in a multiple-satellite scenario is in the decimeter range (see Figure 4.6 again), it seems to be an attractive possibility for the system designer to exploit the periodicity by choosing valid multiples of $d_E^{(\text{opt})}$. However, the slope of $\varepsilon_{r_{\text{diff}}}$ linearly increases with v and the same magnitude of satellite movements become, therefore, more severe.

Figure 4.22 shows the relation between $\varepsilon_{r_{\text{diff}}}$ and $\triangle d_s$ for various nominal spacings $\triangle\theta_s$. Consider the case of two MIMO satellites that are separated by nominally $\triangle\theta_s = 0.4°$ as an example (yellow curve). The link shall be operated with an SNR of $\rho_{r,\text{dB}} = 13\,\text{dB}$. To limit the capacity degradation to 0.4 % of C_{opt}, $|\varepsilon_{r_{\text{diff}}}| \leq 0.1$ must be ensured and, thus, the differential longitude librations must not exceed $\triangle d_s = 30\,\text{km}$. The results in Figure 4.22 show also the three-times increased positioning accuracy if v is set from one to three (compare green solid with green dashed curve).

Instead of increasing v to increase $v \cdot d_E^{(\text{opt})}$, the orientation of the earth station ULA δ_E can be changed. If the arrays deviate from broadside, the antenna spacings must be increased to still obtain C_{opt} (see also Figure 4.8 in Section 4.4.3 again). This possibility is illustrated in Figure 4.23, in which the channel capacity is shown as a contour plot projected onto an image. While the first receive antenna is fixed (red cross in the figure), the second receive antenna has been moved. Instead of

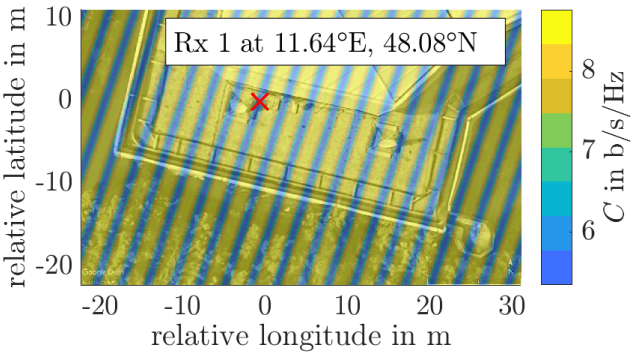

Figure 4.23.: Capacity contour of a 2×2 MIMO dual-satellite scenario (satellite spacing $\triangle\theta_s = 0.5°$, $\theta_s = 10°\,\mathrm{W}$, $f = 11\,\mathrm{GHz}$, $\rho_{r,\mathrm{dB}} = 13\,\mathrm{dB}$, background image © 2018 Google, map data © 2018 GeoBasis-DE/BKG (© 2009), Google).

increasing v, the second receive antenna can be moved on the first capacity maxima next to the red cross to the North or to the South. The actual spacing between the two receive antennas is then sufficiently large, whereas the *relevant antenna spacing* with respect to the two satellite antennas in the GEO is still $a_{rf} \cdot d_{\mathrm{E}}^{(\mathrm{opt})}$.

4.7. Impact of the Atmosphere

4.7.1. Impact of Atmospheric Phase Disturbances

It can be shown that the channel capacity remain unaffected by the phase disturbances $\xi_{\mathrm{u},n}$ in the uplink channel and $\xi_{\mathrm{d},m}$ in the downlink channel. To this end, first rewrite (3.2) to

$$C = \log_2\left(\det\left(\mathbf{I}_Z + \frac{\rho_\mathrm{u}}{N}\widetilde{\mathbf{H}}_\mathrm{u}\widetilde{\mathbf{H}}_\mathrm{u}^\mathrm{H} \cdot \left[\mathbf{I}_Z - \left(\mathbf{I}_Z + \frac{\sigma_{\boldsymbol{\eta}_\mathrm{u}}^2}{\sigma_{\boldsymbol{\eta}_\mathrm{d}}^2}\mathbf{F}^\mathrm{H}\widetilde{\mathbf{H}}_\mathrm{d}^\mathrm{H}\widetilde{\mathbf{H}}_\mathrm{d}\mathbf{F}\right)^{-1}\right]\right)\right). \tag{4.59}$$

To analyze the impact of atmospheric phase disturbances, consider the case where all MIMO antennas are perfectly aligned such that $\mathbf{G}_\mathrm{u} = \mathbf{1}$, $\mathbf{G}_\mathrm{d} = \mathbf{1}$. Applying the channel matrices $\widetilde{\mathbf{H}}_\mathrm{u} = \mathbf{H}_\mathrm{u}\mathbf{D}_\mathrm{u}$ and $\widetilde{\mathbf{H}}_\mathrm{d} = \mathbf{D}_\mathrm{d}\mathbf{H}_\mathrm{d}$ as defined in (2.7) to (4.59), it follows for the MIMO channel capacity

$$C = \log_2\left(\det\left(\mathbf{I}_Z + \frac{\rho_\mathrm{u}}{N}\mathbf{H}_\mathrm{u}\mathbf{D}_\mathrm{u}\mathbf{D}_\mathrm{u}^\mathrm{H}\mathbf{H}_\mathrm{u}^\mathrm{H}\left[\mathbf{I}_Z - \left(\mathbf{I}_Z + \frac{\sigma_{\boldsymbol{\eta}_\mathrm{u}}^2}{\sigma_{\boldsymbol{\eta}_\mathrm{d}}^2}\mathbf{F}^\mathrm{H}\mathbf{H}_\mathrm{d}^\mathrm{H}\mathbf{D}_\mathrm{d}^\mathrm{H}\mathbf{D}_\mathrm{d}\mathbf{H}_\mathrm{d}\mathbf{F}\right)^{-1}\right]\right)\right). \tag{4.60}$$

The matrices $\mathbf{D}_\mathrm{u}\mathbf{D}_\mathrm{u}^\mathrm{H}$ and $\mathbf{D}_\mathrm{d}^\mathrm{H}\mathbf{D}_\mathrm{d}$ are diagonal matrices having the elements $\left|\varsigma_{\mathrm{u},n}\right|^2, n = 1,\ldots,N$ and $\left|\varsigma_{\mathrm{d},m}\right|^2, m = 1,\ldots,M$ on their main diagonals, i.e.

$$\mathbf{D}_\mathrm{u}\mathbf{D}_\mathrm{u}^\mathrm{H} = \mathrm{diag}\left\{\left|\varsigma_{\mathrm{u},1}\right|^2,\ldots,\left|\varsigma_N\right|^2\right\}, \text{ and } \mathbf{D}_\mathrm{d}^\mathrm{H}\mathbf{D}_\mathrm{d} = \mathrm{diag}\left\{\left|\varsigma_{\mathrm{d},1}\right|^2,\ldots,\left|\varsigma_{\mathrm{d},M}\right|^2\right\}. \quad (4.61)$$

Consider now the case that $\left|\varsigma_{\mathrm{u},n}\right| = 1\ \forall n$ and $\left|\varsigma_{\mathrm{d},m}\right| = 1\ \forall m$, i.e. no additional path attenuation is assumed in the uplink and the downlink. It follows that $\mathbf{D}_\mathrm{u}\mathbf{D}_\mathrm{u}^\mathrm{H} = \mathbf{I}_N$ and $\mathbf{D}_\mathrm{d}^\mathrm{H}\mathbf{D}_\mathrm{d} = \mathbf{I}_M$. Hence, the MIMO channel capacity is not reduced by atmospheric disturbances of the signal phase.

4.7.2. Verification through Channel Measurements

The model in (2.13) assumes that the phase disturbance of two LOS rays ending at the same earth station antenna are identical because the horizontal separation of two paths is less than 0.5 cm (see the example in Section 2.2.3.2 again). This assumption has been verified through interferometric measurements in the Ku-band at 12.5 GHz [SHK15a, SHK15b]. Two ground antennas pointed to one single-satellite and received the same satellite signal (e.g. the beacon). The phase difference between the two receive signals have been measured and recorded for several months. The correlation between both receive signal streams reveal the desired phase difference. After a correction of imperfections of the receiving equipment (e.g. temperature drifts between the cables), a measurement sensitivity of better than 0.5° root mean square (RMS) with a resolution of 1/100 Hz was achieved.

Note that this measurement setup constitutes a worst-case scenario because the antennas on Earth were separated by a few meters. In this case, the horizontal distance between the two LOS paths through the atmosphere was approximately 2 m. Since $r_\mathrm{min} \gg h_\mathrm{a} \leq 20$ km, this spatial separation of 2 m of the two LOS paths through the turbulent atmosphere remain almost constant. In this respect, the results reported in [SHK15a, SHK15b] constitute a worst-case scenario.

Figure 4.24 is reproduced from [SHK15a, SHK15b] and shows a three-days snapshot of the RMS phase difference σ_p between two paths (lower part of Figure 4.24). The measured phase difference is related to local weather phenomena. The results indicate that the sun and the rise of the phase fluctuations between adjacent LOS paths are correlated. The maximal observed RMS phase difference was only slightly above 2°. A cumulative distribution function (CDF) of all the measurement data within one month shows that 99 % of all observations were below $\sigma_\mathrm{p} = 2.8°$ ([SHK15a, Fig. 5]). These measurement results are basically in line with the results reported from other campaigns, e.g. in [KCS+00, KIK86, KHL+12, MDAN13].[14]

[14] Note that it is very difficult to directly compare results from other measurements because the scope, measurement setup and signal processing prior to the estimation process differ. Most

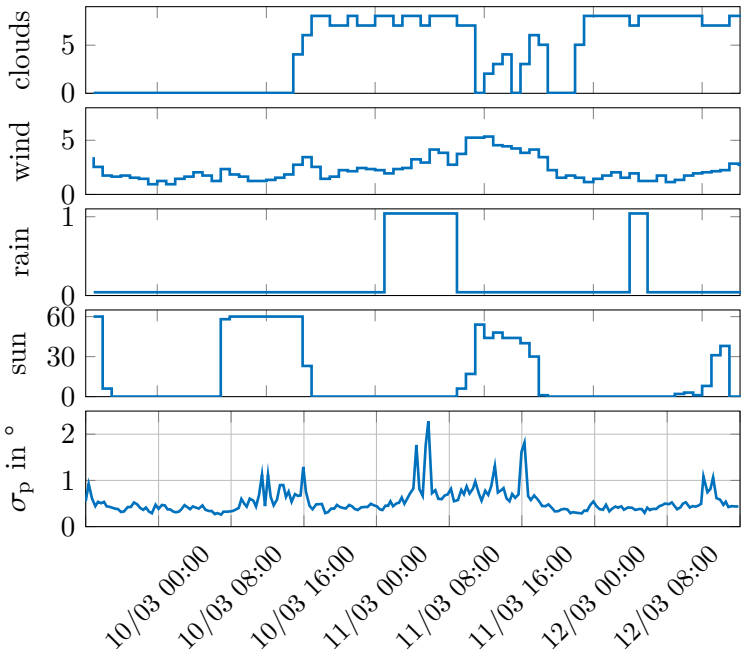

Figure 4.24.: Analysis of phase difference within a three day period; clouds are given in okta, wind in Beaufort, rain as a binary indicator and the visibility of the sun in minutes per hour [SHK15b]

Based on these results, the potential capacity degradation due to phase perturbations in the channel are now evaluated. To this end, the additional phase offset $\triangle\phi_m$ between two receiving paths at the m-th receive antenna is introduced. The phase-impaired channel matrix of a 2×2 MIMO downlink can then be modeled as

$$\mathbf{H}_{\mathrm{d}}^{(\mathrm{p})} = a_{\mathrm{d}} \begin{bmatrix} \mathrm{e}^{-\mathrm{j}\left(\frac{2\pi}{\lambda_{\mathrm{d}}} r_{\mathrm{d},11} + \triangle\phi_1\right)} & \mathrm{e}^{-\mathrm{j}\,\frac{2\pi}{\lambda_{\mathrm{d}}} r_{\mathrm{d},12}} \\ \mathrm{e}^{-\mathrm{j}\,\frac{2\pi}{\lambda_{\mathrm{d}}} r_{\mathrm{d},21}} & \mathrm{e}^{-\mathrm{j}\left(\frac{2\pi}{\lambda_{\mathrm{d}}} r_{\mathrm{d},22} + \triangle\phi_2\right)} \end{bmatrix}.$$

Potential depointing losses are neglected, i.e. perfect alignment of all antennas is assumed ($\mathbf{G}_{\mathrm{d}} = \mathbf{1}$). Furthermore, the relative phase offsets $\triangle\phi_m$ are statistically modeled following a Gaussian distribution [Whe01] with variance σ_{p}^2:

$$\triangle\phi_m \sim \mathcal{N}(0, \sigma_{\mathrm{p}}^2),\ \forall m.$$

of the interferometric measurements focus on celestial observations of stars or galaxies. The received signals are averaged over long time spans to improve the results and reduce the noise. Atmospheric phase fluctuations are effectively reduced, which contradicts the objective of the measurements in [SHK15b]. The performance of the system described in [SHK15a] constitutes a balanced compromise between measurement accuracy (better than 0.5° RMS phase difference) and temporal resolution (1/100 Hz).

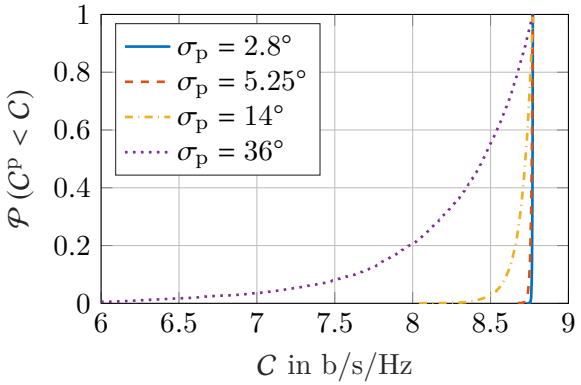

Figure 4.25.: Empirical CDF of the capacity C^{p} due phase impairments in the channel for different σ_{p} (reproduced from [SHK15b]).

Applying the same model in the uplink, the instantaneous channel capacity C^{p} is calculated by using $\mathbf{H}_{\mathrm{u}}^{(\mathrm{p})}$ and $\mathbf{H}_{\mathrm{d}}^{(\mathrm{p})}$ in (3.1).

The results of a Monte Carlo simulation of C^{p} are shown as an empirical CDF in Figure 4.25. To calculate the capacity for each observation a receive SNR of $\rho_{\mathrm{u}} |a_{\mathrm{u}}|^2 = \rho_{\mathrm{d}} |a_{\mathrm{d}}|^2 = 16\,\mathrm{dB}$ has been assumed. The result based on the highest reported value measurement result of $\sigma_{\mathrm{p}} = 2.8°$ from [SHK15a, SHK15b] is compared to the values of $\sigma_{\mathrm{p}} = 5.25°$, which has been reported in [KHL+12], and of $\sigma_{\mathrm{p}} = 36°$ reported in [KCS+00]. The values of $\sigma_{\mathrm{p}} = 5.25°$ and $\sigma_{\mathrm{p}} = 36°$ have been measured for an antenna distance of 33 m and 100 m at a carrier frequency of 12.4 GHz and 11.7 GHz, respectively.

The results for $\sigma_{\mathrm{p}} = 2.8°$ and $\sigma_{\mathrm{p}} = 5.25°$ show no significant loss in the channel capacity. Only for the very high value of $\sigma_{\mathrm{p}} = 36°$, a capacity loss can be observed. However, for 80 % of all observations at least $0.92 \cdot C_{\mathrm{opt}} = 8\,\mathrm{b/s/Hz}$ is obtained. Recall that the measurement results apply for carrier frequencies around 12 GHZ. Measurement results for higher frequency bands, like for example the Q/V-band, are not yet available. Further campaigns are necessary to validate the model assumptions also for higher frequencies. Particularly the Q/V-band is of interest and a promising candidate for future MIMO HTS scenarios.

Since Q/V-band measurements are not yet available, it is assumed that the phase disturbances at those frequencies are comparable to the perturbations at 12.5 GHz. If the worst-case value of $\sigma_{\mathrm{p}} = 2.8°$ from the measurements in [SHK15a] are applied to a 60 GHz carrier, the RMS phase difference between two LOS paths must be scaled according to $60\,\mathrm{GHz}/12.5\,\mathrm{GHz} \cdot 2.8° < 14°$. The simulation results for the value of $\sigma_{\mathrm{p}} = 14°$ are additionally presented in Figure 4.25. The curve for $\sigma_{\mathrm{p}} = 14°$ show that the capacity degradation remain very low.

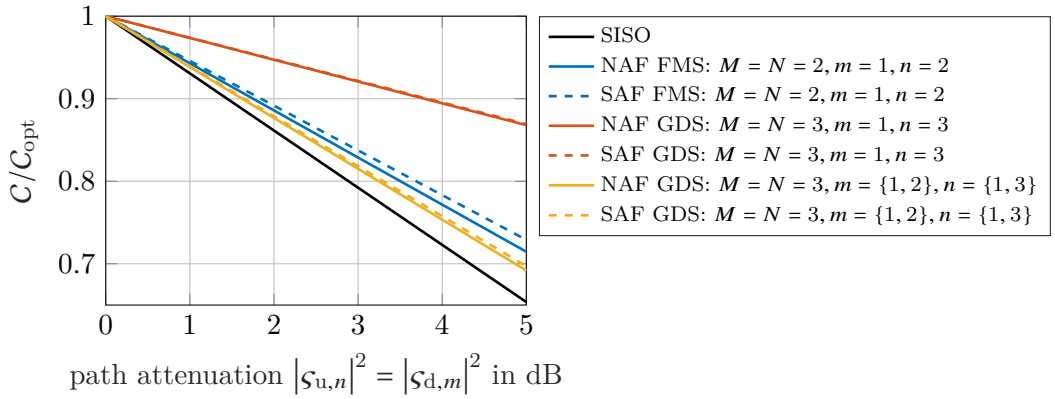

Figure 4.26.: Capacity degradation due to tropospheric attenuation at the transmit and receive antennas.

4.7.3. Impact of Atmospheric Attenuation

The diagonal matrices $\mathbf{D}_{\text{u}}\mathbf{D}_{\text{u}}^{\text{H}}$ and $\mathbf{D}_{\text{d}}^{\text{H}}\mathbf{D}_{\text{d}}$ in (4.61) contain the additional path attenuation in the uplink and downlink channel, respectively. While $|\varsigma_{\text{d},m}|^2$ reduces the receive SNR $\rho_{\text{d}}\,|a_{\text{d}}|^2$ individually at the m-th ground antenna, the values of $|\varsigma_{\text{u},n}|^2$ reduce the radiated power of the n-th transmit antenna.

Figure 4.26 shows the impact of tropospheric attenuation on C_{opt}. The relative capacity of a SISO system is compared to a $2\times2\times2$ FMS and a $3\times2\times3$ GDS. The case of one antenna in the uplink and downlink is faded (black, blue and red curves) is compared to the case that two out of three ground antennas in the uplink and downlink are faded (yellow curve). The curves show that the capacity degradation of a MIMO system relative to the respective optimum C_{opt} is always less than that of the SISO system. Only if all MIMO antennas are faded simultaneously, the slopes of the MIMO curves equal then the slope of the SISO curve [SKL09, KSL10] (not shown in the figure). This gain is a result of a site-diversity effect. An additional attenuation of, for example, 4 dB at one antenna does not result in a 4 dB lower SNR in one of the two equivalent sub-channels because all MIMO ground antennas contribute equally to the total receive SNR. Finally, the capacity advantage of the SAF over the NAF relay system can be observed when the orthogonality is lost between the row and column vectors in $\widetilde{\mathbf{H}}_{\text{u}}$ and $\widetilde{\mathbf{H}}_{\text{d}}$, respectively.

4.8. Key Results and Main Contribution

The key results and the main contribution of this chapter are summarized as follows:

1. **Optimal Positioning of MIMO Antennas (OPA):** The requirements for optimal MIMO satellite channels were derived. The lengths of the LOS propa-

gation paths must have a particular difference so that the signals at the receive antennas are combined with a distinct offset in phase. This requirement of different path lengths leads to specific geometrical arrangements of the antennas. The criterion of the **O**ptimal **P**ositioning of the MIMO **A**ntennas (OPA) is presented in (4.46) that allows to optimally place the antennas on Earth in dependence on the locations of the antennas in the GEO. The OPA has been verified through real MIMO channel measurements.

2. **Applicable to uplink and downlink:** The OPA criterion is valid for the uplink and the downlink. It can be used to calculate the optimal transmit antenna positions and the optimal receive antenna positions on the ground in relation to the satellite antennas.
3. **Antenna Spacing:** The antenna spacing is a key design parameter. Because of the very large distance of around 36 000 km between the earth stations and the GEO, comparably large antenna spacings are required, either on ground or in orbit. Figure 4.6 provides an excellent overview of the necessary spacing on the ground in relation to the antenna spacing in the GEO. As a general rule, the larger the spacing in orbit, the smaller is the spacing on ground and vice-versa.
4. The **orientation of the antenna arrays** with respect to each other is a further important parameter that directly affects the required antenna spacing. The smallest spacing is generally obtained if the antenna arrays are in broadside. If instead the earth station array is perpendicular to the axis of the satellite array, no difference in the phase of the receive signals can be observed. In such a *keyhole configuration* the available spatial sub-channels reduce to one, and only the minimum MIMO capacity is achieved.
5. **Definition of MIMO Application Categories:** The possibility to differently deploy the antennas in the GEO has led to the definition of three basic categories of MIMO SATCOM applications: the *Single-Satellite Application*, the *Co-Located Satellites Application* and the *Multiple-Satellites Application*.
6. **Depointing Loss and Antenna Patterns:** The maximum antenna spacing is constrained by the depointing loss of high-directional antennas. This limits the achievable capacity of the Multiple-Satellites Application. If the satellites are more than 1.5° apart, the depointing loss dominates the capacity degradation making this scenario impracticable for FSS applications.
7. **Positioning Accuracy on the Ground:** The necessary positioning accuracy with respect to the optimal antenna spacing on the ground depends on the category of MIMO applications. If the minimum spacing on the ground is large (Single-Satellite Application), huge deviations in the kilometer-range are possible and still the close-to-maximum channel capacity can be achieved. The required positioning accuracy increases to the decimeter range for Co-

Located Satellites Applications and to the centimeter range for Multiple-Satellites Applications.

8. **Longitude Reacquisition of a Single Satellite:** Once an optimal arrangement of the ground antennas has been installed, a huge part of the GEO can be used with this fixed installation without entailing a significant capacity loss. Depending on the orientation of the antenna arrays with respect to each other, the part of the geostationary arc that can be covered ranges from some tens of degrees up to the entire visible arc.
9. **Non-ideal GEO and Station-Keeping Requirements:** No capacity degradation is observed if a single-satellite moves within the limits of a typical station-keeping box. In the case multiple satellites in different orbits (co-located or in different orbital slots), coordinated station-keeping and cluster maintenance maneuver are necessary to limit the capacity variation due to independent satellite movements. State-of-the-art techniques are sufficient to achieve the necessary positioning accuracy.
10. **Impact of the Troposphere:** The results of interferometric channel measurements reveal that differential phase perturbations in the troposphere are very small such that the optimal capacity is not significantly degraded. Tropospheric attenuation at the transmit antenna and at the receive antenna leads to a attenuation of the effective EIRP and the receive SNR, respectively.

The results in this chapter indicate that the Single-Satellite Application is the most promising candidate application for MIMO over satellite. The complexity in the space segment and the expected capacity losses under real conditions are significantly lower compared to the case of multiple satellites (co-located or on different orbit positions). An example of a LLMF payload has been proposed in Figure 3.2. The main advantages of the Single-Satellite Application are summarized as follows:

- simplified station-keeping, no additional requirements
- no capacity degradation due to satellite motion
- implementation of the SAF architecture is possible (assuming DTP)
- no ground antenna depointing losses
- low requirements on positioning accuracy of ground antennas

The MIMO category of the Single-Satellite Application is the perfect candidate to address the data rate demands in future high-throughput satellite (HTS) applications. A MIMO system proposal based on a HTS scenario is presented next revealing the great advantage of spatial MIMO compared to the state-of-the-art.

5. MIMO HTS System Proposal

The proposed concept of spatial MIMO based on distributed antennas is now applied to a high-throughput satellite (HTS) system. HTS systems represent the most recent and powerful satellite architectures for high-data rate multicast and unicast communications. The aim of this chapter is to show how greatly state-of-the-art satellite systems can benefit from spatial multiplexing in both their uplink and their downlink if the design requirements derived in Chapter 4 are appropriately considered. In the following example, the theory from Chapter 4 will be used to maximize the sum throughput of an HTS system. This system proposal and the following results have recently been published in the journal paper [SDSK19].

5.1. System Description

The considered FSS scenario belongs to the class of single-satellite MIMO applications since one HTS equipped with several antennas is considered. The MIMO HTS system architecture is shown in Figure 5.1. The focus is on the forward link from the gateway to the users.

The Earth portion of the MIMO feeder link consists of $N = 2$ gateway antennas, separated by several kilometers (30 km to 50 km) and inter-connected via a central processing unit which supervises the generation of the transmit signals. Time and phase synchronization of the antennas is ensured. RF-over-fiber transport can, for example, be used for this purpose [LLT14]. This technology has been successfully applied at the NASA deep space network, where antennas separated by more than 10 km must be synchronized for deep space communications. In the following, it is assumed that the inter-connection between the gateway antennas is perfect.

At the satellite, $Z_\mathrm{r} = 2$ receive antennas are positioned $d_\mathrm{s} = 3\,\mathrm{m}$ apart, constituting the receive array of the MIMO feeder link. To operate this feeder link, the bands 42.5-43.5 GHz and 47.2-50.2 GHz are exploited such that a total bandwidth of 4 GHz per polarization state is available. The receive antennas cover the same geographical region centered in the middle of the gateway array, and the assumption is made that their beamwidth is sufficiently large. In that way, the antennas are relatively close to the beam center, and the receive antenna gain is maximum for all transmit-receive antenna links.

The satellite payload relies on a bent-pipe architecture with cross-strapping from

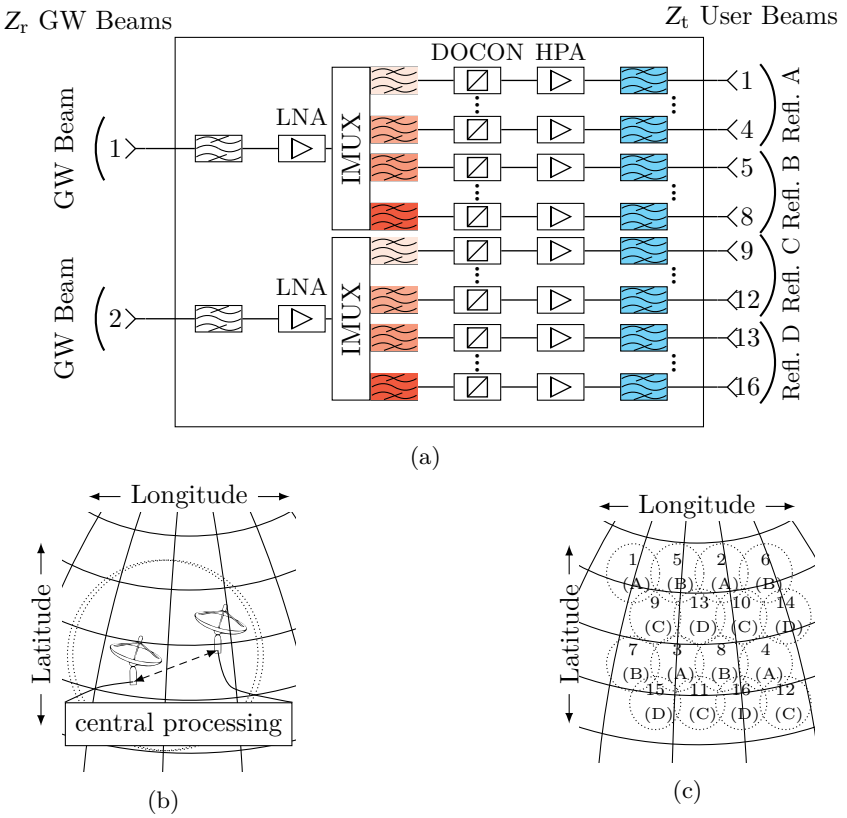

Figure 5.1.: Proposed system architecture [SDSK19]: (a) Block diagram of the payload. (b) Two gateway antennas are fed with signals by a common gateway station (central processing). (c) Illustration of the 16 spot beam footprints (3 dB contours). Source feed and reflector are labeled inside every footprint.

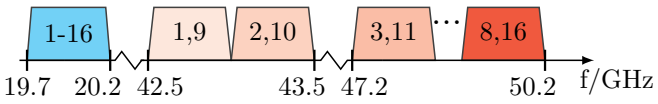

Figure 5.2.: Single polarization frequency plan for up- and downlink [SDSK19]. FFR in the Ka band downlink. The multiplexing gain enables a parallel transmission of two feed signals by the feeder link within the same frequency segment of the V band. The numbers indicate the corresponding beam according to Figure 5.1

.

the V band feeder uplink to the Ka band user downlink (see Figure 5.1a). No signal processing is considered in the payload to keep the satellite complexity low. The payload translates all incoming frequency bands to the same frequency band in the Ka band to enable FFR (see Figure 5.2). Colored bandpass filters in Figure 5.1a indicate the corresponding frequency range according to Figure 5.2

The downlink part of the HTS system is made of $Z_\mathrm{t} = 16$ Ka band user beams (see Figure 5.1c) delivering different data contents to fixed single antenna UTs. On the satellite a single-feed per beam (SFPB) architecture with $Z_\mathrm{refl} = 4$ multibeam reflectors is considered. The reflectors are geometrically arranged as a uniform circular array with a diameter of 3 m. On Earth a total of K_tot UTs are uniformly distributed over the area covered by the Z_t beams. A downlink bandwidth of 500 MHz within the range of 19.7-20.2 GHz is available in the service zone. Since an FFR scheme is addressed, this frequency band is jointly utilized by all beams.

The achievable multiplexing gain offered in the downlink is limited by the number of downlink feeds. Hence, a group of up to $Z_\mathrm{t} = 16$ UTs can be served simultaneously via space division multiple access (SDMA). Thus, the user downlink forms at most a 16×16 MIMO channel. Since $K_\mathrm{tot} \gg Z_\mathrm{t}$, additional user scheduling is necessary to build groups of UTs that will be served in different time slots based on a time division multiple access (TDMA) scheme. The approach from [SK17] will be applied to schedule the K_tot users.

5.2. Channel and System Model

5.2.1. MIMO Feeder Uplink and Multibeam Downlink Channel

The MIMO feeder link channel for the MIMO HTS scenario is modeled in the equivalent baseband using a block diagonal matrix

$$\widetilde{\mathbf{H}}_\mathrm{u} = \mathrm{diag}\left\{\widetilde{\mathbf{H}}_{\mathrm{u},1}, \ldots, \widetilde{\mathbf{H}}_{\mathrm{u},\frac{Z_\mathrm{t}}{2}}\right\} \in \mathbb{C}^{Z_\mathrm{t} \times Z_\mathrm{t}}, \tag{5.1}$$

where $\widetilde{\mathbf{H}}_{\mathrm{u},l}$ is a 2×2 channel matrix between the $N = 2$ gateway antennas and the $Z_\mathrm{r} = 2$ satellite receive antennas. The index l distinguishes the $Z_\mathrm{t}/2$ different center frequencies required due to the use of frequency division multiple access (FDMA) in addition to SDMA in the feeder uplink. Each entry $\widetilde{h}^{(\mathrm{u})}_{l,zn}$ corresponds to the channel coefficient from the n-th gateway antenna to the z-th satellite receive antenna at the l-th center frequency and takes both the free space propagation and the atmospheric impairments into account as well as the antenna patterns into account. Thus, the entries of $\widetilde{\mathbf{H}}_{\mathrm{u},l}$ are modeled according to (2.15).

In case of FFR, an arbitrary UT can potentially receive signal portions from all feeds. The antenna patterns of the multibeam antennas play an important role to

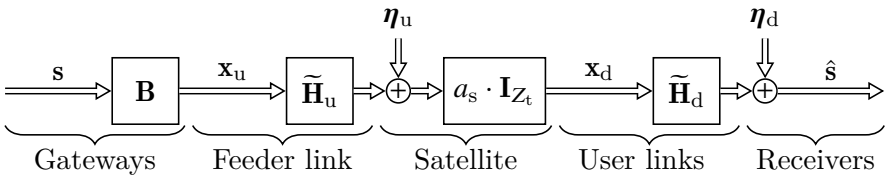

Figure 5.3.: Block diagram of the transmission chain

assess the achievable gains and must carefully be taken into account. Similar to the uplink, the downlink channel matrix $\widetilde{\mathbf{H}}_\mathrm{d} \in \mathbb{C}^{K \times Z_\mathrm{t}}$ is modeled according to (2.16) with the antenna patterns given by (2.9).

As stated before, only up to $K = Z_\mathrm{t}$ users can be simultaneously served within a single time slot. In order to supply all users with individual data, scheduling is necessary, i.e. the K_tot UTs must be divided into groups of at most Z_t users. Hence, in addition to spatial multiplexing, a further multiple access scheme like TDMA is necessary to support all users with individual data. Note that without spatial multiplexing, K_tot time slots would be necessary while with MIMO the number of necessary time slots reduces to K_tot/K.

The results of Chapter 4 have shown that the achievable data rate of any MIMO SATCOM scenario crucially depends on the location of the involved antennas. Since the locations of the users are arbitrary and do not follow any regular placement, an analytic solution for the optimal placement, like the one that has been derived in (4.46) for ULA arrangements, cannot be found here. However, the requirement of pairwise orthogonal channel vectors as formulated in (4.1) still holds. Assuming an optimal setup in the sense of (4.1), then all K UTs of a group have orthogonal channel vectors. However, the probability that such a set of UTs exists is zero for a finite number K_tot [SUBW04]. The idea of the proposed user grouping algorithm in [SK17] is, therefore, to combine UTs with channel vectors that are *at most* orthogonal. The orthogonality between two UTs is quantified by means of the scalar product of the two channel vectors according to (4.1). Since equality in (4.1) cannot be obtained for a finite set of channel vectors, the algorithm allows a small deviation from exact zero. This threshold is a design parameter and controls the entire system performance in terms of throughput [SK17]. The user grouping algorithm in [SK17] is applied here to schedule all users into N_G disjoint groups.

5.2.2. MIMO HTS System Model

The equivalent baseband model of the HTS system under study is now introduced. Figure 5.3 shows a block diagram of the transmission chain with the associated notations. Let $\mathbf{s} = [s_1, \ldots, s_K]^\mathrm{T} \in \mathbb{C}^{K \times 1}$ be the vector of data symbols to be transmitted in a given time slot to a group of K non-cooperative single-antenna UTs,

where s_k is the symbol for the k-th user. These symbols are chosen from a constellation alphabet[15] $\mathbb{A}$ with unit variance, and are uncorrelated such that $\mathrm{E}\left\{\mathbf{s}\mathbf{s}^{\mathrm{H}}\right\} = \mathbf{I}_K$. In the central processing unit of the gateway, a linear transformation of the data vector $\mathbf{s}$ is performed using a precoding matrix $\mathbf{B} \in \mathbb{C}^{Z_\mathrm{t} \times K}$. This matrix aims to mitigate the interference between the symbols transmitted in the same frequency channel in the uplink as well as in the downlink. For its computation full CSI of the uplink and the downlink is assumed in the central processing unit of the gateway. Recall that the focus here is not on the design of the precoding matrix. The applied approach to derive $\mathbf{B}$ is thoroughly explained in [SDSK19].

Denoting by P_u/N the maximum EIRP per gateway antenna, the following condition must be fulfilled

$$\mathrm{tr}\left\{\mathbf{B}^{\mathrm{H}}\bar{\mathbf{Q}}_n\mathbf{B}\right\} \leq P_\mathrm{u}/N\,, \quad n = 1,2. \tag{5.2}$$

The matrix $\bar{\mathbf{Q}}_n = \mathrm{diag}\left\{\mathbf{Q}_n, \ldots, \mathbf{Q}_n\right\}$ is a $Z_\mathrm{t} \times Z_\mathrm{t}$ block diagonal matrix where $\mathbf{Q}_n$ is a 2×2 matrix containing zeros in all entries except for the n-th diagonal element which is equal to 1. That is, in $\bar{\mathbf{Q}}_1$ all odd and in $\bar{\mathbf{Q}}_2$ all even diagonal entries are 1 while the remaining entries are zero. Condition (5.2) corresponds to a per-antenna power constraint and takes into account that the gateway antennas are equipped with their own HPA each. After the transmission over the MIMO feeder link, the symbols received by the satellite are

$$\mathbf{y}_\mathrm{u} = \left[y_{\mathrm{u},1}, \ldots, y_{\mathrm{u},Z_\mathrm{t}}\right]^{\mathrm{T}} = \widetilde{\mathbf{H}}_\mathrm{u}\mathbf{B}\mathbf{s} + \boldsymbol{\eta}_\mathrm{u}. \tag{5.3}$$

The vector $\boldsymbol{\eta}_\mathrm{u} = \left[\eta_{\mathrm{u},1}, \ldots, \eta_{\mathrm{u},Z_\mathrm{t}}\right]^{\mathrm{T}}$ is the vector of uplink circularly-symmetric complex Gaussian noise and is uncorrelated with the data symbols. In the sequel, the variance per real dimension of the complex uplink noise process is equal for all Z_t receive branches and is denoted by $\sigma^2_{\boldsymbol{\eta}_\mathrm{u}}/2$. In the satellite payload, the coefficient a_s models the amplification of the HPAs. The vector of channel inputs to the downlink is then given by

$$\mathbf{x}_\mathrm{d} = \left[x_{\mathrm{d},1}, \ldots, x_{\mathrm{d},Z_\mathrm{t}}\right]^{\mathrm{T}} = a_\mathrm{s} \cdot \widetilde{\mathbf{H}}_\mathrm{u}\mathbf{B}\mathbf{s} + a_\mathrm{s} \cdot \boldsymbol{\eta}_\mathrm{u} \tag{5.4}$$

with $x_{\mathrm{d},z}$ being the downlink signal transmitted by the z-th feed. The downlink EIRP in each beam should not exceed a maximum value of P_d such that

$$\left[\mathbf{R}_{\mathbf{x}_\mathrm{d}}\right]_{z,z} \leq P_\mathrm{d},\ z \in \{1, \ldots, Z_\mathrm{t}\}, \tag{5.5}$$

where $\mathbf{R}_{\mathbf{x}_\mathrm{d}} = \mathrm{E}\left\{\mathbf{x}_\mathrm{d}\mathbf{x}_\mathrm{d}^{\mathrm{H}}\right\}$ is the autocorrelation matrix of $\mathbf{x}_\mathrm{d}$. The gain a_s is consequently chosen to fulfill the constraint (5.5) with equality for at least one of the

[15] Modulations are chosen according to the DVB-S2X standard [Eur14].

feeds. At least one downlink beam provides the maximum downlink EIRP P_{d} while the EIRP of the remaining beams can be lower or, in the best case, equal to P_{d}.

In the user links, the receive symbols are obtained as

$$\hat{\mathbf{s}} = [\hat{s}_1, \ldots, \hat{s}_K]^{\mathrm{T}} = a_{\mathrm{s}} \cdot \widetilde{\mathbf{H}}_{\mathrm{d}} \widetilde{\mathbf{H}}_{\mathrm{u}} \mathbf{B} \mathbf{s} + a_{\mathrm{s}} \cdot \widetilde{\mathbf{H}}_{\mathrm{d}} \boldsymbol{\eta}_{\mathrm{u}} + \boldsymbol{\eta}_{\mathrm{d}}, \tag{5.6}$$

where $\boldsymbol{\eta}_{\mathrm{d}} = \left[\eta_{\mathrm{d},1}, \ldots, \eta_{\mathrm{d},K}\right]^{\mathrm{T}}$ is the vector of downlink circularly-symmetric complex Gaussian noise. This noise is uncorrelated with both the data symbols $\mathbf{s}$ and the uplink noise $\boldsymbol{\eta}_{\mathrm{u}}$. Assuming similar receiving equipment for all users, the variance per real dimension of the noise process at each UT is identical and represented by $\sigma^2_{\boldsymbol{\eta}_{\mathrm{d}}}/2$. The downlink receive SNR at the center of a spot beam is defined as

$$(C/N)_{\mathrm{bc}} = |a_{\mathrm{d}}|^2 \cdot P_{\mathrm{d}} / \sigma^2_{\boldsymbol{\eta}_{\mathrm{d}}}, \tag{5.7}$$

where a_{d} is the free space downlink gain as defined in (2.10).

5.3. Simulation Results

5.3.1. Performance Criterion

To assess the performance of the proposed MIMO HTS system, the sum achievable rate is used. The sum achievable rate can be obtained by first computing for each user its input-output mutual information. To this end, we define an auxiliary model from (5.6). Using $\mathbf{C} = a_{\mathrm{s}} \widetilde{\mathbf{H}}_{\mathrm{d}} \widetilde{\mathbf{H}}_{\mathrm{u}} \mathbf{B}$, we can write

$$\hat{\mathbf{s}} = \mathrm{diag}\{\mathbf{C}\}\,\mathbf{s} + (\mathbf{C} - \mathrm{diag}\{\mathbf{C}\})\,\mathbf{s} + a_{\mathrm{s}} \widetilde{\mathbf{H}}_{\mathrm{d}} \boldsymbol{\eta}_{\mathrm{u}} + \boldsymbol{\eta}_{\mathrm{d}} = \mathrm{diag}\{\mathbf{C}\}\,\mathbf{s} + \bar{\boldsymbol{\eta}}, \tag{5.8}$$

where $\bar{\boldsymbol{\eta}}$ is a vector gathering the contributions of the uplink and downlink noise as well as the inter-stream interference if $\mathbf{C}$ is non-diagonal. We note that the matrix $\mathbf{C}$ will not be diagonal if $\widetilde{\mathbf{H}}_{\mathrm{u}}$ or $\widetilde{\mathbf{H}}_{\mathrm{d}}$ are rank deficient, i.e. that no zero forcing is possible. In practice, a satellite link will be designed to avoid such a configuration. In the uplink, this is ensured if the gateway antennas are located following the design criteria of (4.46). In the downlink, this is ensured if the users who are jointly considered have nearly or at most orthogonal channel vectors according to (4.1). Assuming a circularly-symmetric complex Gaussian distribution for the inter-stream interference, the channel law for the k-th user in a given time slot is

$$\mathcal{P}(\hat{s}_k | s_k) = \frac{1}{2\pi\sigma^2_{\bar{\boldsymbol{\eta}},k}} \cdot \exp\left\{ -\frac{|\hat{s}_k - c_{kk} s_k|^2}{2\pi\sigma^2_{\bar{\boldsymbol{\eta}},k}} \right\} \tag{5.9}$$

Table 5.1.: Positioning parameters of the MIMO HTS example.

Parameter	**Value**
Center frequency uplink	$f = 46.35\,\mathrm{GHz}$
Orbit position HTS	$\theta_\mathrm{s} = 115°\,\mathrm{W}$
Spacing satellite receive antennas	$d_\mathrm{s} = 3\,\mathrm{m}$
Geographical position gateway ULA	$\phi_\mathrm{E} = 38°\,\mathrm{N}, \theta_\mathrm{E} = 98°\,\mathrm{W}$
Array orientation gateway / satellite	$\delta_\mathrm{E} = \delta_\mathrm{s} = 0°$
Optimal gateway antenna spacing	$d_\mathrm{E}^{(\mathrm{opt})} = 43\,\mathrm{km}$

with c_{kk} the k-th diagonal element of $\mathbf{C}$ and $2\sigma^2_{\bar{\boldsymbol{\eta}},k}$ the variance of the k-th entry of the complex vector $\bar{\boldsymbol{\eta}}$. With the knowledge of (5.9), the input-output mutual information in bit per channel use for the k-th user is given by

$$\mathcal{I}_k = \mathrm{E}\left\{\log_2\left(\frac{\sum_{s\in\mathbb{A}} \mathcal{P}\left(\hat{s}_k|s\right)}{\mathcal{P}\left(\hat{s}_k|s_k\right)}\right)\right\}. \tag{5.10}$$

The achievable rate in $\mathrm{bit\,s^{-1}}$ is obtained from the mutual information $\mathcal{I}_k$ by normalization with the symbol duration T_s. This duration is assumed to be given by $T_s = 1/W_\mathrm{d}$ such that $\mathcal{R}_k = W_\mathrm{d} \cdot \mathcal{I}_k$. The sum achievable rate is then given by

$$\mathcal{R} = \frac{1}{N_\mathrm{G}} \sum_{g=1}^{N_\mathrm{G}} \sum_{k=1}^{K^g} \mathcal{R}_k^g, \tag{5.11}$$

where the superscript g is introduced to take into account the fact that several user groups are considered. Finally, the rate per user beam $\overline{\mathcal{R}}$ is defined as $\overline{\mathcal{R}} = \mathcal{R}/Z_\mathrm{t}$. The sum achievable rate $\mathcal{R}$ defined in (5.11) together with the rate per user beam $\overline{\mathcal{R}}$ allow to assess the performance of the proposed MIMO HTS system.

5.3.2. MIMO HTS Simulation Results

The proposed MIMO uplink and downlink architectures will now be evaluated for a satellite positioned at the longitude $\theta_\mathrm{s} = 115°\,\mathrm{W}$. The feeder uplink operates in the V band, and the user downlink is in the Ka band. The gateway array has an orientation of $\delta_\mathrm{E} = 0°$. It is located at latitude $\phi_\mathrm{E} = 38°\,\mathrm{N}$ and longitude $\theta_\mathrm{E} = 98°\,\mathrm{W}$. With a center frequency of $f = 46.35\,\mathrm{GHz}$ in the uplink, the optimal antenna spacing is calculated according to (4.46) as $d_\mathrm{E}^{(\mathrm{opt})} = 43\,\mathrm{km}$ (see Table 5.1 for a summary of all relevant parameters). Finally, the $Z_\mathrm{t} = 16$ user beams in an SFPB architecture cover the U.S. West Coast where a total of $K_\mathrm{tot} = 4000$ households have to be served.

To emphasize the benefits of spatial multiplexing for an HTS system, the up-

Table 5.2.: Parameters for the feeder link evaluation

	SISO	**MIMO**
Frequency bands	42.5 GHz-43.5 GHz, 47.2 GHz-50.2 GHz	
Number of downlink feeds Z_t	16	
Usable bandwidth per downlink beam	250 MHz	500 MHz
Gateway antenna gain	61.4 dBi	
Transmit power per gateway antenna	22 dBW	19 dBW
Downlink configuration		
Architecture	MU-MIMO FFR	
SNR at the center of a beam $(C/N)_{bc}$	10 dB	

link and the downlink of the system described in Section 5.1 will be successively replaced by a state-of-the-art approach. Here, the two following configurations will be investigated in terms of the sum achievable data rate:

- A 2×2 MIMO feeder link is compared to a SISO feeder link with single-site diversity, i.e. one SISO gateway antenna is active while the second SISO gateway antenna is in stand-by.
- A MU-MIMO downlink is compared to a conventional FR4 SISO approach.

5.3.2.1. Feeder Link Performance

The system parameters for the analysis of the feeder link are provided in Table 5.2. The objective is to assess the performance of a 2×2 MIMO feeder link in terms of the sum achievable data rate. The available bandwidth in the feeder uplink is 4 GHz. Due to the 2×2 spatial multiplexing in the MIMO feeder link, a total of 8 GHz usable bandwidth is available in the user downlink. $Z_t = 16$ downlink feeds should be supported and, thus, the users in each downlink beam can be served with 500 MHz of bandwidth.

The SISO feeder link instead can only support a bandwidth of 4 GHz in total, and, therefore, the user bandwidth W_d is set for this benchmark system to 250 MHz. In order to still meet coordinated power density limits, the EIRP of the MIMO feeder link must be the same as of the SISO feeder link. Therefore, the transmit power per gateway antenna is 3 dB less in the case of a MIMO gateway antenna. Assume a gateway antenna gain of 61.4 dBi, and, together with a Figure of Merit (G/T) of 26 dB K^{-1} per satellite antenna, the feeder link budget is fully defined. Under clear sky conditions an uplink receive SNR of 24 dB is achieved.

For the user links a MU-MIMO FFR approach with a receive SNR of 10 dB at the center of the spot beams is always assumed. It ensures that the differences in terms of sum achievable rate between the SISO and the MIMO feeder links are, in

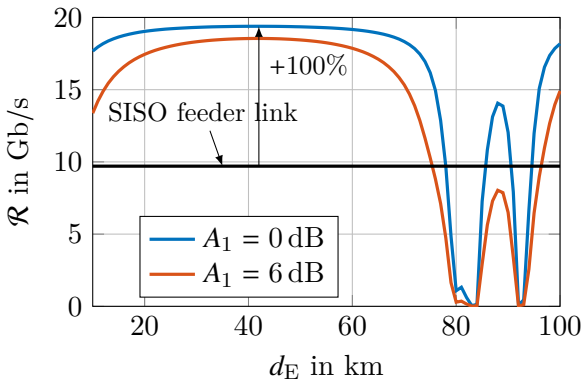

Figure 5.4.: Sum rate vs. gateway antenna spacing d_E for two different weather conditions at gateway antenna one while gateway antenna two experience clear sky, i.e. $A_2 = 0\,\text{dB}$

this case, only influenced by the uplink design.

In Figure 5.4, the influence of the gateway separation d_E on the sum achievable rate is shown for two different weather conditions. In one scenario, the first gateway antenna does not experience any rain attenuation, i.e. $A_1 = 0\,\text{dB}$, while the other scenario assumes a medium rain attenuation of $A_1 = 6\,\text{dB}$. The second gateway antenna benefits in both scenarios from clear-sky conditions, i.e. $A_2 = 0\,\text{dB}$. For the benchmark SISO feeder link, the second gateway is the only active antenna.

The sum achievable rate is maximized for a separation of around $d_E^{(\text{opt})} = 43\,\text{km}$ but a large range of $\triangle d_E = \pm 15\,\text{km}$ relative to the optimal position can be accepted without entailing serious performance degradations. By using (4.50), the huge range of $\triangle d_E = \pm 15\,\text{km}$ results in a deviation from the optimal antenna arrangement of $\varepsilon_{r_{\text{diff}}} = \triangle d_E / d_E^{(\text{opt})} = \pm 15\,\text{km}/43\,\text{km} = \pm 0.35$. Since the uplink SNR with 24 dB is comparably high, only a small capacity degradation of $\triangle C \approx 99.5\,\%$ must be accepted (see dot-dashed curve for $\rho_{r,\text{dB}} = 24\,\text{dB}$ in Figure 4.3). This explains the wide plateau of the blue curve in Figure 5.4.

The improved sum data rate of the MIMO solution is the result of spatial multiplexing in the feeder uplink. Although 4 GHz of bandwidth is allocated in the feeder uplink, 8 GHz of user link bandwidth instead of 4 GHz for the state-of-the-art can be used to serve the 4000 users in the downlink. It can be noted that the minima for values of d_E near 80 km and 90 km are due to the presence of close-to-singular MIMO channel matrices in the bands 47.2-50.2 GHz and 42.5-43.5 GHz, respectively. However, distances of more than 80 km do not belong to the region of interest for a practical system design.

Moreover, although the uplink exploits a huge part of the frequency spectrum ranging from 42.5 GHz to 50.2 GHz with a center frequency at $f = 46.35\,\text{GHz}$, only

a small capacity degradation must be accepted at the band edges. Using (4.22), the deviation from the optimal antenna arrangement is calculated as $\varepsilon_{r_{\text{diff}}} = \triangle f/f = \pm 3.85\,\text{GHz}/46.35\,\text{GHz} = \pm 0.08$, which is too small to observe a significant capacity degradation at an SNR of 24 dB.

The curves show also that an additional atmospheric attenuation does not severely degrade the data rate performance of the MIMO feeder link. Even for a rain attenuation of $A_1 = 6\,\text{dB}$ at gateway antenna one, the MIMO feeder link still outperforms the state-of-the-art SISO approach even in clear-sky. One reason for this small degradation is clearly the 14 dB higher uplink SNR compared to the downlink SNR (24 dB in the uplink vs. 10 dB in the downlink). However, an additional attenuation of 6 dB at one antenna does, nevertheless, not result in a 6 dB lower SNR in one of the two equivalent SISO sub-channels. In fact, since in an optimal MIMO channel both gateway antennas contribute equally to the receive SNR, an attenuation of 6 dB at one gateway antenna results only in a 3 dB lower SNR per receive antenna. Apart from the multiplexing gain, the additional spatial domain usage of the MIMO approach inherently provides a higher robustness against weather effects [KSL10, SKL09]. In other words: The results clearly suggest to avoid so-called *cold redundancy* with respect to gateway antennas, i.e. it is better to switch all available antennas on and operate them as a MIMO feeder link instead of preserving antennas for outage redundancy only.

The results presented in this section illustrate the potential of the spatial MIMO concept for the feeder links of HTS systems. The possibility to distribute spatially multiplexed signals containing individual content for multiple users perfectly supports the resort of the conventional TV broadcast scenario to unicast transmission. Please note again that the goal of this simulation example was to illustrate how spatial multiplexing can generally be realized in a single feeder link. Several tens of spatially separated feeder links are necessary in practice [VVL+12b], and, in this case, the advantage of the MIMO approach lies in the reduction of the interference between neighboring feeder links [DSSK18]. Less geographically separated MIMO feeder links than SISO feeder links are required to provide a given amount of data to serve all users with different content in a practical HTS. Therefore, if the feeder links have to be deployed in a certain country or continent, interference can be more easily avoided by guaranteeing a larger angular separation between the beams [DK18]. This is especially advantageous in terms of system availability as better link budgets reduce the probability of experiencing an outage when rain events affect the link quality [DK18].

Table 5.3.: Parameters for the user link evaluation

	SISO FR4	**MU-MIMO FFR**
Number of downlink feeds Z_t	16	
Bandwidth per beam	125 MHz	500 MHz
Downlink EIRP per beam P_d	51 dBW to 65 dBW	
User terminal G/T	16.9 dB K^{-1}	
SNR at beam center $(C/N)_{bc}$	6 dB to 20 dB	0 dB to 14 dB
Uplink configuration		
Architecture	MIMO feeder link with d_E = 40 km	
Frequency bands	42.5-43.5 GHz	42.5-43.5 GHz 47.2-50.2 GHz

5.3.2.2. User Link Performance

The second simulation aims to investigate the data rate performance of the proposed multiuser MIMO downlink. The objective is to show the advantage of having multiple spatially separated antennas on the satellite in combination with full frequency reuse among the user beams. The result is compared to a contemporary SISO scheme that is based on a single-reflector with four color frequency reuse. To highlight the importance of spatially separated antennas to benefit from a MIMO gain, the multiple-reflector approach is also compared to a MIMO downlink based on a single-antenna with multiple beams and FFR.

The system parameters for this simulation are provided in Table 5.3. As already introduced in Section 5.1, four reflectors form a circular array with a diameter of 3 m, and four feeds illuminate each reflector. Each reflector has a diameter of D = 2.6 m. The feed and reflector geometry is based on a satellite that is currently in orbit [FTA+16]. The service zone of the Z_t = 16 spot beams is over North America, and we assume 250 independent and fixed single-antenna receivers per beam. The location of an individual user is randomly chosen; all users are uniformly distributed over the entire service zone. Hence, in total $K_{tot} = 16 \cdot 250 = 4000$ users need to be served with data[16]. An equal G/T of 16.9 dB for each UT is assumed.

In order to show the benefit of spatial MIMO for different signal-to-noise ratios, various downlink EIRP values P_d are simulated in each beam ranging from 51 dBW to 65 dBW. Please note again that, in the case of MIMO, P_d constitutes the maximum power in at least one of the MIMO beams while the power in the remaining beams can actually be equal to or lower than P_d. This is the result of the power constraint as defined in (5.5). In the SISO case instead, each beam provides the maximum downlink EIRP P_d. Thus, the sum power over all beams of the SISO

[16] This simulation scenario and the parameter setup have also been used in [SK17]. An illustration of the antenna geometry on the satellite is shown in Figure 1 of the paper [SK17].

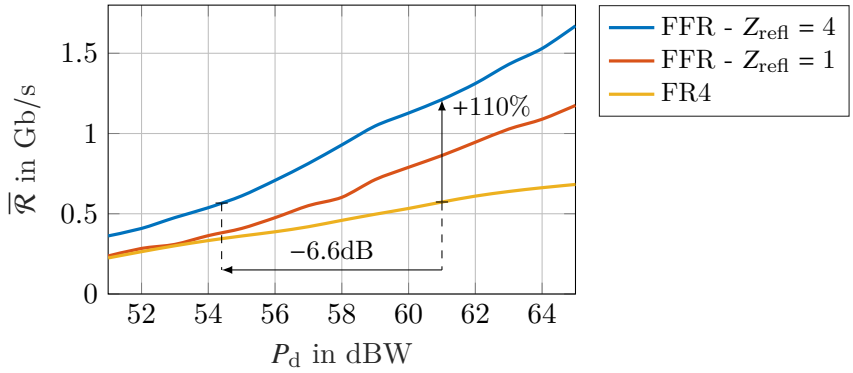

Figure 5.5.: Achievable rate per beam as a function of the downlink EIRP using a MIMO feeder link with $d_{\text{E}}^{(\text{opt})} = 40\,\text{km}$ and clear-sky conditions at both gateway stations.

downlink is always higher or at most equals the sum power of the MIMO downlink. This ensures a fair comparison between MIMO and SISO.

Moreover, in the FFR scheme the entire bandwidth of 500 MHz within the range of 19.7 GHz to 20.2 GHz is available in each beam. In the case of the four-color scheme instead, only 125 MHz per beam can be used. To ensure a fair comparison, the transmit power per beam is equal for both, the FFR and the FR4 scheme. As a consequence, the resulting receive SNR is even 6 dB higher for the FR4 scheme than for the FFR scheme.

Since the focus is now on the performance of the multiuser downlink, the feeder uplink configuration is identical for all considered cases. In particular, a 2×2 MIMO feeder link in the V band is assumed, and the gateway antennas have a spacing of $d_{\text{E}}^{(\text{opt})} = 40\,\text{km}$. Please note that, to support the aggregated bandwidth in the user link, the occupied bandwidth in the feeder link is adjusted accordingly. While for the FR4 scheme 1 GHz of bandwidth is sufficient, 4 GHz of bandwidth is necessary to support the FFR approach. A constant uplink receive SNR of 24 dB is achieved in all cases.

Figure 5.5 provides the simulation results of the sum achievable rate per user beam as a function of the downlink EIRP P_{d}. The blue curve corresponds to the proposed MU-MIMO FFR strategy with $Z_{\text{refl}} = 4$ reflectors. The yellow curve shows the result of the state-of-the-art FR4 approach with $W_{\text{d}} = 125\,\text{MHz}$ per user beam. As mentioned earlier, the result of a MIMO downlink with a single-reflector that generates all the user beams is also provided (red curve). The difference in the sum achievable rate depends on the downlink EIRP P_{d}.

The MU-MIMO downlink with four separated antennas offers the highest sum achievable data rate in all considered cases. To give an example: Comparing the blue and the yellow curves at $P_{\text{d}} = 61\,\text{dBW}$, the MU-MIMO downlink achieves

1.2 Gb/s per beam compared to 0.55 Gb/s only for the SISO FR4 approach. This constitutes an increase of 110 %. The satellite operator has now various options how this gain can be exploited:

1. Provide simply higher data rates to the users,
2. keep the sum data rate constant and reduce the necessary downlink EIRP,
3. exploit the gain as an additional link margin to increase the availability of the downlink.

For example, keeping the sum achievable data rate constant would allow for a reduction of the required downlink EIRP by 6.6 dB. This reduction could be transferred into a lower payload weight and power budget and, finally, cost reduction. As an alternative, the interference potential in terms of downlink adjacent satellite interference can be reduced.

Moreover, the MIMO downlink with four spatially separated reflectors indeed outperforms the multibeam MIMO approach based on a single-reflector. The reason is simply that the spacing of the feed elements is much smaller (in the centimeter-range) for the single-reflector approach compared to the four separated reflectors (in the meter-range). As a consequence, the spacing between two users who are part of the same group needs to be much larger[17], e.g. more than 1000 km compared to around 50 km. Since, in addition, the 3 dB-contour of one beam footprint is ≈ 500 km, the signal energy that can be received from neighboring MIMO beams is comparably low. In other words, the interference from neighboring MIMO beams, which we are seeking to exploit as information bearing signal, is very low due to this large separation of two users who are jointly served with data. Low signal interference results in a MIMO downlink channel matrix with small values, and the multiplexing gain is ultimately limited.

The simulation results have shown the data rate advantage of spatial multiplexing in both, the uplink and the downlink. Through multiplexing of different data streams, multiple users can be served simultaneously over the same channel. The gain of the considered HTS system relies on the spatial separation of the MIMO antennas.

[17] Recall the linear relation $d_{\mathrm{s}} d_{\mathrm{E}} \propto r\lambda$ between the antenna spacing as a function of the wavelength λ and the UT-satellite distance r, which has been introduced in Section 4.3. As a result, the smaller the spacing in orbit the larger must be the spacing on Earth.

6. Conclusion

The potentials of the spatial multiple-input multiple-output (MIMO) technology and its applicability to fixed satellite networks were investigated. The MIMO channel capacity was used as the metric to reveal the gains that can be expected in practice. The spatial distribution of multiple antennas offers an additional degree of freedom that can be used to realize the MIMO gains, be it an increased power efficiency through beamforming, an increased link reliability through spatial diversity or an increased bandwidth efficiency through spatial multiplexing. The actual gain that can be achieved by spatial MIMO strongly depends on the wireless channel. Whereas terrestrial mobile systems can usually take advantage of a large scattering environment with multipath in the channel, the satellite channel for fixed satellite services (FSS) is dominated by a strong Line-of-Sight (LOS) component.

The requirements for maximum-capacity MIMO channels over geostationary satellites were derived. It was shown that the physically correct modeling of the signal phase using the spherical wave model (SWM) is of utmost importance. The lengths of the LOS propagation paths must have a particular difference so that the signals at the receive antennas are combined with a distinct offset in phase. Based on this finding the criterion of the **O**ptimal **P**ositioning of the MIMO **A**ntennas (OPA) was derived that allows to optimally place the antennas on Earth and in orbit. The antenna spacing is a key design parameter. Due to the large Earth-to-space distance of about 36 000 km in geostationary earth orbit (GEO) applications, relatively large antenna spacing either on the ground or in orbit is required. If all MIMO antennas are deployed on a single satellite having a spacing in the meter range, the antenna spacing on the ground must be in the range of several tens of kilometers. It was shown that, if the OPA criterion is satisfied in *the uplink and the downlink*, the MIMO satellite system achieves the *maximum MIMO capacity gain*. The approach was validated through real satellite channel measurements. With the possibility to differently deploy the antennas in orbit, three categories of MIMO over satellite were defined: the *Single-Satellite Application*, the *Co-Located Satellites Application* and the *Multiple-Satellites Application*.

Assuming optimized satellite links, the capacity performance of MIMO FSS networks was analyzed taking real impact factors into account. Since the OPA is based on a particular geometrical antenna arrangements, the necessary positioning accuracy and potentially degrading effects were analyzed, including the impact of satellite motion or longitude reacquisition. The influence of the troposphere as well

as the impact of antenna radiation pattern on the optimal MIMO link were considered. The results show the feasibility of spatial MIMO to fixed satellite networks. In particular the Single-Satellite Application has been shown to be a promising candidate for future high-throughput satellite (HTS) and very high throughput satellite (VHTS) realizations. An example of a MIMO HTS system concept was proposed using MIMO in the feeder uplink and full frequency reuse (FFR) with multibeam antennas in the multiuser MIMO (MU-MIMO) downlink. Simulation results show the significantly improved throughput compared to the current state-of-the-art single-input single-output (SISO) feeder link with four color frequency reuse (FR4) in the user links.

Utilizing the spatial dimension as a further physical resource besides time, frequency and polarization is the perfect solution to cope with the interference in the satellite channel as well as to address the data rate requirements in future HTS applications. With OPA, a profound framework was provided to design multi-antenna satellite communication (SATCOM) systems that achieve the maximum capacity gain. This way, the interference issue in modern FSS networks can be solved by actively exploiting the interference as an information bearing signal, which is then part of a MIMO satellite network.

A. Detailed Derivation of Equation (3.14)

Using the substitutions $x = \gamma_{\mathrm{u},1}$, $y = \gamma_{\mathrm{d},1}$, $a = \rho_{\mathrm{u}}/N$ and $b = \rho_{\mathrm{d}}/N$, and considering the case $W = 2$, the optimization problem in (3.13) can be formulated as

$$\begin{aligned} \max_{x,y} \quad & f(x,y) = \left(1 + \left(\frac{1}{ax} + \frac{1}{by} + \frac{1}{abxy}\right)^{-1}\right) \cdot \\ & \qquad \left(1 + \left(\frac{1}{a(c-x)} + \frac{1}{b(d-y)} + \frac{1}{ab(c-x)(d-y)}\right)^{-1}\right) \qquad \text{(A.1)} \\ \text{s.t.} \quad & c > x > 0, d > y > 0, a > 0, b > 0. \end{aligned}$$

The parameters c and d are the sum of the two uplink and downlink eigenvalues. To find the maximum of $f(x,y)$, the two-dimensional gradient vector $\nabla f(x,y)$ has been computed. The two entries of $\nabla f(x,y)$ are given as

$$\begin{bmatrix} -\frac{ab(by+1)\cdot(bd-by+1)}{\left(ax+by+1\right)^2 \cdot \left(a(c-x)+b(d-y)+1\right)^2} \cdot \Big[(d-2y)\left(1+a^2x^2\right) + 2a(dx-cy) \\ \qquad + (c-2x)\left(aby^2 - abdy - a^2cy\right) \Big] \\ -\frac{ab(ax+1)\cdot(ac-ax+1)}{\left(ax+by+1\right)^2 \cdot \left(a(c-x)+b(d-y)+1\right)^2} \cdot \Big[(c-2x)\left(1+b^2y^2\right) + 2b(cy-dx) \\ \qquad + (d-2y)\left(abx^2 - abcx - b^2dx\right) \Big] \end{bmatrix},$$

which are required to be zero. Since the fractional terms in front of the square brackets can never be zero, the following system of equations must be solved

$$\begin{aligned} \Big[(d-2y)\left(1+a^2x^2\right) + 2a(dx-cy) + (c-2x)\left(aby^2 - abdy - a^2cy\right) \Big] &= 0 \\ \Big[(c-2x)\left(1+b^2y^2\right) + 2b(cy-dx) + (d-2y)\left(abx^2 - abcx - b^2dx\right) \Big] &= 0 \end{aligned}$$

By inspection, one solution is $x = c/2$ and $y = d/2$. To verify that this solution gives a maximum, the Hessian matrix is computed at this particular point, which is given as

$$\mathbf{H}_f\left(x = \frac{c}{2}, y = \frac{d}{2}\right) = \begin{bmatrix} -2a^2bd\frac{(bd+2)^2(2ac+bd+4)}{(ac+bd+2)^4} & 2ab\frac{(ac+2)^2(bd+2)^2}{(ac+bd+2)^4} \\ 2ab\frac{(ac+2)^2(bd+2)^2}{(ac+bd+2)^4} & -2ab^2c\frac{(ac+2)^2(ac+2bd+4)}{(ac+bd+2)^4} \end{bmatrix}.$$

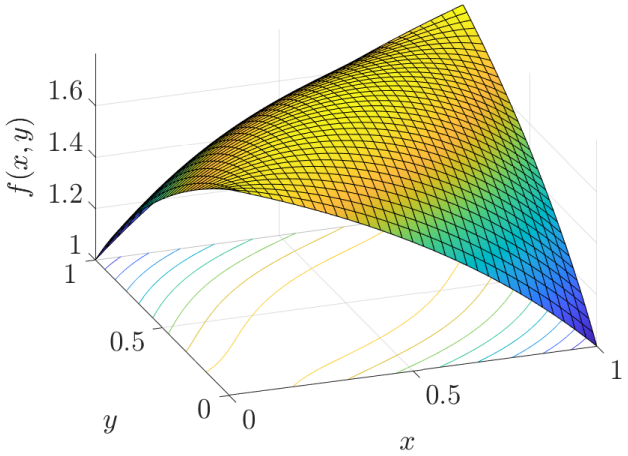

Figure A.1.: $f(x,y)$ for $a = b = 2$, $c = d = 1$ showing two maxima at $x = y = 0$ and $x = c, y = d$ in addition to $x = c/2, y = d/c$

If $x = c/2, y = d/2$ shall be a maximum, the determinant of $\mathbf{H}_f$ must be positive because $\left[\mathbf{H}_f\left(x = c/2, y = d/2\right)\right]_{1,1} < 0$. Therefore, we require that

$$\det\left(\mathbf{H}_f\left(x = \frac{c}{2}, y = \frac{d}{2}\right)\right) = 8a^2b^2 \cdot \frac{(abcd-2)(ac+2)^2(bd+2)^2}{(ac+bd+2)^6} > 0,$$

which can be simplified to $abcd > 2$. In other word, if the signal-to-noise ratio satisfies the condition $abcd > 2$, the solution of two equally strong eigenvalues in the uplink *and* two equally strong eigenvalues in the downlink provides a maximum of the problem in (3.13).

However, $abcd > 2$ is not a sufficient condition to ensure that $x = c/2, y = d/2$ leads to the global maximum of $f(x,y)$. To this end, $f(x,y)$ is shown in Figure A.1 for the parameters $a = b = 2, c = d = 1$ such that $abcd = 4 > 2$ is satisfied. It can be observed that the two points $x = c, y = d$ and $x = 0, y = 0$ provide a local maximum as well.[18] To ensure that $f(x = c/2, y = d/2)$ provides the global maximum, the inequality $f(x = c/2, y = d/2) > f(x = c, y = d) = f(x = 0, y = 0)$ must be satisfied, which results for $N = 2$ antennas in the stronger condition

$$\frac{(ac+2)^2(bd+2)^2(ac+bd+1)}{(ac+1)(bd+1)(ac+bd+2)^2} > 4.$$

[18] Please note that $x = c, y = d$ and $x = 0, y = 0$ are not valid points for the problem in (A.1) because (A.1) requires two non-zero eigenvalues. These boundary points could, therefore, not have been found with the approach of (A.1).

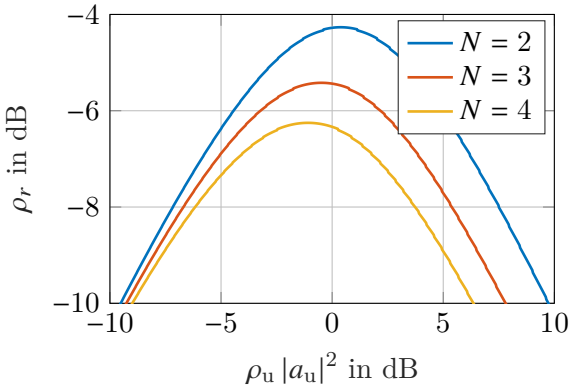

Figure A.2.: Minimum receive signal-to-noise ratio (SNR) ρ_r such that equally strong eigenvalues in the uplink and downlink lead to a global maximum of the channel capacity

This condition can be generalized for arbitrary N as follows:

$$
\begin{aligned}
f\left(x = \frac{c}{N}, y = \frac{d}{N}\right) &> f\left(x = c, y = d\right) \\
\left(1 + \left(\frac{1}{a\frac{c}{N}} + \frac{1}{b\frac{d}{N}} + \frac{1}{ab\frac{cd}{N^2}}\right)^{-1}\right)^N &> \left(1 + \left(\frac{1}{ac} + \frac{1}{bd} + \frac{1}{abcd}\right)^{-1}\right) \\
\sum_{k=1}^{N} \binom{N}{k} \left(\frac{1}{a\frac{c}{N}} + \frac{1}{b\frac{d}{N}} + \frac{1}{ab\frac{cd}{N^2}}\right)^{-k} &> \left(\frac{1}{ac} + \frac{1}{bd} + \frac{1}{abcd}\right)^{-1}
\end{aligned}
\tag{A.2}
$$

In other words, the total signal-to-noise ratio ρ_r at the receiving ground station must be sufficiently large. Figure A.2 shows the minimum receive SNR ρ_r as defined in (3.15) that is at least required in order to fulfill (A.2). All curves show negative values with a maximum of around $-4\,\mathrm{dB}$ for a satellite system with $M = Z = N = 2$ antennas. Receive SNR values of $-4\,\mathrm{dB}$ and less are not operationally relevant (the DVB-S2X waveform with the lowest spectral efficiency requires an SNR of at least $-2.9\,\mathrm{dB}$ to close the link [Eur14]). Therefore, it is concluded that condition (A.2) can be fulfilled in all practically relevant scenarios such that solution $x = c/2, y = d/2$ provides the global maximum of the problem in (A.1).

B. Approximation Error Assessment

B.1. Approximation Error Analysis of Equation (4.18)

The condition in (4.18) is an approximation for arbitrary antenna numbers with $W = \min\{M, Z\} > 2$. In the following, it will be shown that the approximation in (4.18) holds with negligible loss of accuracy for all practically relevant MIMO SATCOM application cases.

Denoting by $e_{M\times Z}$ the absolute error in (4.18) such that

$$r_{\text{diff}} = v \cdot \lambda/V + e_{M\times Z}, \tag{B.1}$$

the relative approximation error in (4.18) is then expressed by

$$\varepsilon_{M\times Z} = \left| e_{M\times Z}/(v \cdot \lambda/V + e_{M\times Z}) \right|. \tag{B.2}$$

Comparing (4.12) with (4.18) it follows that $e_{M\times Z} = 0$ if $M = Z = 2$, and the optimal capacity is obtained exactly at $r_{\text{diff}} = v\lambda/Z$. For $W \geq 3$ and large uniform linear array (ULA) dimensions compared to the transmitter-receiver distance, the absolute value of $|e_{M\times Z}|$ increases and r_{diff} must deviate from $v\lambda/Z$ in order to still achieve C_{opt}. To analyze this deviation, the parameters to describe the dimensions of the ULAs are introduced as follows:

$$L_{\text{s},Z} = (Z-1) \cdot d_{\text{s}}, \text{ and } L_{\text{E},M} = (M-1) \cdot d_{\text{E}}, \tag{B.3}$$

where d_{s} and d_{E} denote the antenna spacing at the transmit ULA and the receive ULA, respectively.

The relative error $\varepsilon_{M\times Z}$ versus $L_{\text{E},M}$ normalized by transmitter-receiver distance r is provided in Figure B.1a. The ratio $L_{\text{s},Z}/r$ was fixed and set to $L_{\text{s},Z}/r = 1 \times 10^{-3}$, which is sufficiently small compared to the range of $0 < L_{\text{E},M}/r \leq 0.4$ on the x-axis to ensures that $\varepsilon_{M\times Z}$ is only determined by $L_{\text{E},M}/r$. Note that all curves in Figure B.1a satisfy condition (B.1). As expected, the error generally increases for larger ratios $L_{\text{E},M}/r$. The more antennas are deployed, the higher are the slopes of the curves. However, the error is generally very small. In the case of three antennas at each side (dark blue curve) the error is $\varepsilon_{M\times Z} \approx$ over the entire range of $0 < L_{\text{E},M}/r \leq 0.4$. An error of 1 % for arrays with four antennas (red curve) requires a very high ratio of $L_{\text{E},M}/r = 0.4$, which has no practical relevance in GEO

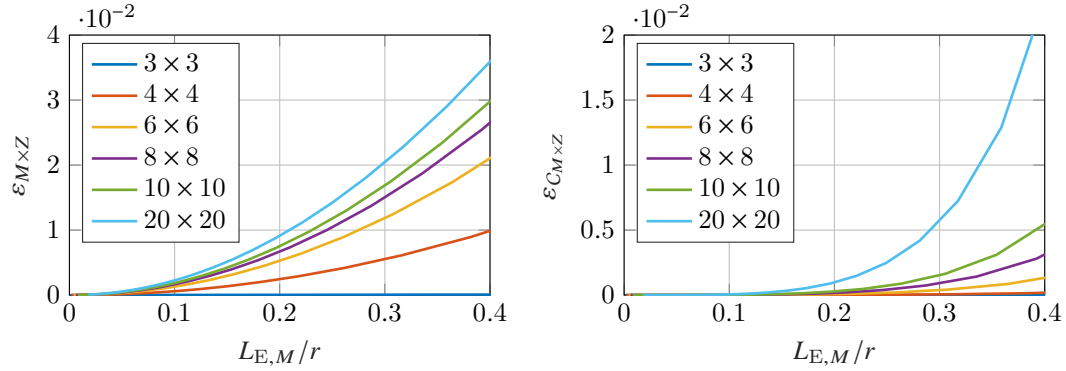

(a) Relative error $\varepsilon_{M\times Z}$ as a function of the array size $L_{\mathrm{E},M}$ normalized by the transmitter-receiver distance r for various antenna numbers.

(b) Capacity error $\varepsilon_{C_{M\times Z}}$ as a function of the array size $L_{\mathrm{E},M}$ normalized by the transmitter-receiver distance r for various antenna numbers.

Figure B.1.: Analysis of the approximation error in (4.18).

applications. In order to not exceed array dimensions of 2000 km, the maximum ratio is $L_{\mathrm{E},M}/r \leq 0.05$.

To prove that even the small values from Figure B.1a do not significantly affect C_{opt}, the relative capacity error

$$\varepsilon_{C_{M\times Z}} = 1 - C_{M\times Z}/C_{\mathrm{opt}}, \tag{B.4}$$

is provided in Figure B.1b. Here, $C_{M\times Z}$ denotes the channel capacity for which the differences between the path lengths is exactly $v\lambda/V$. The parameter setup in Figure B.1b matches that of Figure B.1a. The curves reveal that the capacity error due to the approximation in (4.18) can be neglected.

B.2. Approximation Error Analysis of Equation (4.46)

The accuracy of the analytical solution in (4.46) to calculate the optimal locations of the MIMO antennas is discussed. Denoting by e_r the total approximation error in (4.45), it follows for (4.45) that

$$r_{\mathrm{diff}} = |(r_{21} - r_{11}) - (r_{22} - r_{12})| = d_{\mathrm{E}} d_{\mathrm{s}}/r \cdot \left|\psi + 0.21 \cdot \alpha\beta/\triangle r^2\right| + e_r. \tag{B.5}$$

The absolute error e_r is composed of two parts. One part is the total remainder $\triangle R^{(2)}$ due to the Taylor series approximation in (4.42). The second part of e_r is the error due to the simplifications that have been applied from (4.43) to (4.45). Using the full expression of (4.43) as given in (C.6), the absolute error e_r is then given by

$$e_r = \triangle R^{(2)} + \frac{d_\mathrm{E} d_\mathrm{s}}{8r^3} \cdot \Big(\left(3M^2 - 12M + 13\right) d_\mathrm{E}^2 \psi + \left(3Z^2 - 12Z + 13\right) d_\mathrm{s}^2 \psi + (2MZ - 4M - 4Z + 8)\, d_\mathrm{E} d_\mathrm{s} \left(1 + 2\psi^2\right) - (8M - 16)\, d_\mathrm{E} R_o \alpha\psi + (8Z - 16)\, d_\mathrm{s} R_\oplus \beta\psi - (4Z - 8)\, d_\mathrm{s} R_o \alpha + (4M - 8)\, d_\mathrm{E} R_\oplus \beta \Big). \quad \text{(B.6)}$$

For $M = Z = 2$, (B.6) reduces to $e_r(2 \times 2) = \triangle R^{(2)} + d_\mathrm{E} d_\mathrm{s} / \left(8r^3\right) \cdot \left(d_\mathrm{E}^2 + d_\mathrm{s}^2\right) \psi$. In addition to $\triangle R^{(2)}$, the value of e_r depends on the number of antennas M, Z, the antenna spacings d_E and d_s, and the positioning of the antennas relative to each other (represented by α, β and ψ). The total remainder $\triangle R^{(2)}$ is composed of the individual parts according to

$$\triangle R^{(2)} = \left(R_{21}^{(2)} - R_{11}^{(2)}\right) - \left(R_{22}^{(2)} - R_{12}^{(2)}\right), \quad \text{(B.7)}$$

where $R_{mz}^{(2)}$ is the remainder so that $r_{mz} = P_{mz}^{(2)} + R_{mz}^{(2)}$. Using (C.3), an explicit expression of this remainder in the Lagrange form is given by [Kli98]

$$R_{mz}^{(2)} = \frac{f^{(3)}(c_{mz})}{3!} \Delta_{mz}^3 = \frac{r}{16} \cdot (1 + c_{mz})^{-\frac{5}{2}} \cdot \Delta_{mz}^3,$$

with c_{mz} being some number between 0 and Δ_{mz}. It follows for the total remainder

$$\triangle R^{(2)} = \frac{r}{16} \cdot \left((1 + c_{22})^{-\frac{5}{2}} \Delta_{22}^3 - (1 + c_{12})^{-\frac{5}{2}} \Delta_{12}^3 + (1 + c_{11})^{-\frac{5}{2}} \Delta_{11}^3 - (1 + c_{21})^{-\frac{5}{2}} \Delta_{21}^3 \right).$$

An analytical expression of a sharp upper bound of $\left|\triangle R^{(2)}\right|$ is not possible because the actual values of c_{mz} are unknown and can be different for different antenna pairs m, z. In addition, the parameter Δ_{mz} can be positive, negative or zero, depending on the configuration of the geometrical parameters ϕ_E, $\triangle\theta$, δ_E and δ_s. The sign and the value of Δ_{mz} determine the range of c_{mz} and consequently $\triangle R^{(2)}$ making an analytical derivation of an upper bound of $\triangle R^{(2)}$ cumbersome. To this end, computer simulation are preformed to assess e_r.

Figure B.2 shows the results of the relative error

$$\varepsilon_{e_r} = \left| e_r / (\lambda / V) \right|. \quad \text{(B.8)}$$

For all curves the optimal difference between the path lengths is assumed, i.e. $r_\mathrm{diff} = \lambda / V$ with $v = 1$. The geographical longitude of the earth station ULA was fixed at $\theta_\mathrm{E} = 0°$, while θ_s was varied from $-60°$ to $0°$. The remaining parameter setup is as follows: $d_\mathrm{s} = 1\,\mathrm{m}$, $\delta_\mathrm{s} = 0°$, $f = 10\,\mathrm{GHz}$.

As expected from (B.6), the error ε_{e_r} generally increases for increasing $\triangle\theta$ because the antenna spacing d_E must be enlarged to still satisfy (4.46). The slope of each

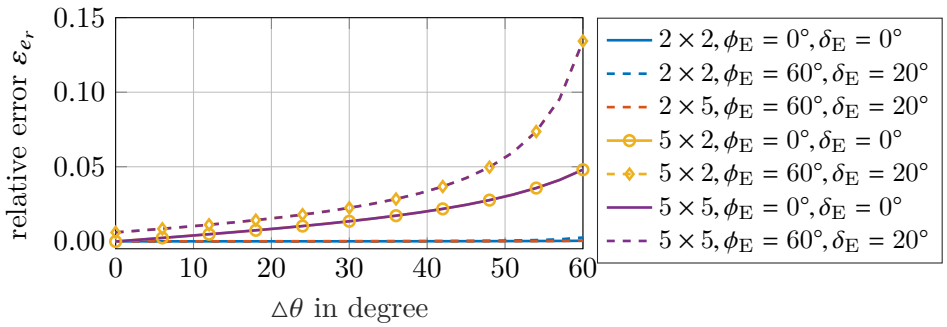

Figure B.2.: Relative error ε_{e_r} due to the approximations in (4.46).

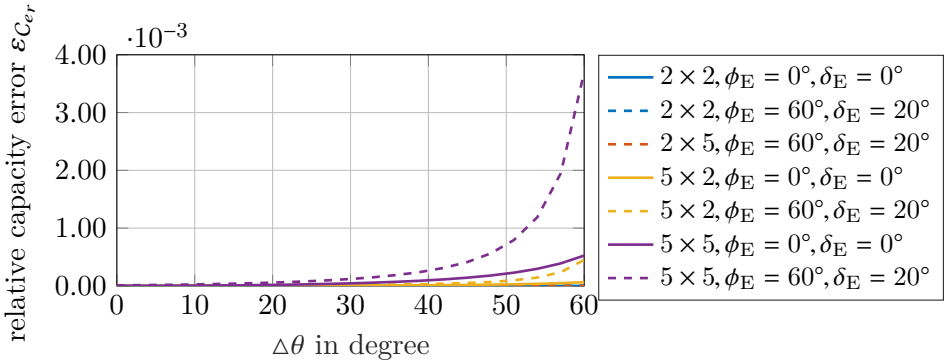

Figure B.3.: Relative capacity error $\varepsilon_{C_{e_r}}$ due to the approximations in (4.46).

curve now depends on the particular parameter setup that affects the increment of d_E. For example, ε_{e_r} is almost identical for both the 5×2 and the 5×5 setup. The impact of Z on ε_{e_r} is negligible because $d_s \ll d_E$. The slopes increase if the orientation δ_E of the ground station ULA significantly differs from that of the satellite ULA because d_E must be increased accordingly (recall the discussion of the *array reduction factor* in Section 4.4.3 along with Figures 4.7 and 4.8).

The relative capacity error

$$\varepsilon_{C_{e_r}} = 1 - C_{e_r}/C_{\text{opt}} \tag{B.9}$$

is shown in Figure B.3, where C_{e_r} is the capacity when the antennas are arranged according to (4.46). The uplink is neglected and a receive SNR of $\rho_{r,\text{dB}} = 10 \log_{10}\left(\rho\,|a|^2\right) = 13\,\text{dB}$ was assumed. The setup of the remaining parameters in Figure B.3 matches that of Figure B.2. The results confirm that the capacity error due to the approximations in (4.46) can be neglected.

C. Detailed Derivations

C.1. Detailed Derivation of Equation (4.40)

In the following the Taylor polynomial approximation given in (4.40) of the path-lengths

$$r_{mz} = r \cdot (1 + \Delta_{mz})^{1/2}$$

is derived. The Taylor series of the function $r_{mz} = f(\Delta_{mz})$ expanded around $\Delta_{mz} = 0$ is also known as the Maclaurin series and is given by [AS83]

$$r_{mz} = f(\Delta_{mz}) = f(0) + \sum_{k=1}^{\infty} \frac{f^{(k)}(0)}{k!} \Delta_{mz}^{k}. \tag{C.1}$$

Here, $k!$ denotes the factorial of k and $f^{(k)}(0)$ denotes the k-th derivative of f evaluated at the point $\Delta_{mz} = 0$. An approximation of r_{mz} is then given by its K-th order Taylor polynomial $P_{mz}^{(K)}$ as

$$r_{mz} \approx P_{mz}^{(K)} = f(0) + \sum_{k=1}^{K} \frac{f^{(k)}(0)}{k!} \Delta_{mz}^{k}. \tag{C.2}$$

The approximation error is given by the remainder term $R_{mz}^{(K)} = r_{mz} - P_{mz}^{(K)}$. An explicit formula of this remainder in the Lagrange form is given by [Kli98]

$$R_{mz}^{(K)} = \frac{f^{(K+1)}(c_{mz})}{(K+1)!} \Delta_{mz}^{K+1}, \text{ with } c_{mz} \in \begin{cases} \{\mathbb{R}, 0 \leq c_{mz} \leq \Delta_{mz}\}, \text{ if } \Delta_{mz} \geq 0 \\ \{\mathbb{R}, \Delta_{mz} \leq c_{mz} \leq 0\}, \text{ if } \Delta_{mz} < 0 \end{cases} \tag{C.3}$$

The parameter c_{mz} is some number between 0 and Δ_{mz}. Applying $K = 2$ in (C.2), the second order Taylor polynomial of (C.1) is then given by

$$P_{mz}^{(2)} = f(0) + f^{(1)}(0) \cdot \Delta_{mz} + f^{(2)}(0) \cdot \Delta_{mz}^{2}/2$$

With $f(0) = r$, $f^{(1)}(0) = r/2$, and $f^{(2)}(0) = -r/4$ it follows that

$$P_{mz}^{(2)} = r \left(1 + \frac{\Delta_{mz}}{2} - \frac{\Delta_{mz}^{2}}{8}\right), \tag{C.4}$$

which is the result given in eq. (4.40). Using (4.34) in (C.4) finally yields

$$P_{mz}^{(2)} = r \cdot \left(1 + \frac{d_{\mathrm{E},m}^2 + d_{\mathrm{s},z}^2}{2r^2} + \frac{R_o\alpha d_{\mathrm{E},m} - R_\oplus\beta d_{\mathrm{s},z} + d_{\mathrm{E},m}d_{\mathrm{s},z}\psi}{r^2} - \frac{d_{\mathrm{E},m}^4 + d_{\mathrm{s},z}^4}{8r^4} \right.$$
$$- \frac{d_{\mathrm{E},m}^2 d_{\mathrm{s},z}^2 + R_o^2\alpha^2 d_{\mathrm{E},m}^2 + R_\oplus^2\beta^2 d_{\mathrm{s},z}^2 + d_{\mathrm{E},m}^2 d_{\mathrm{s},z}^2\psi^2}{4r^4}$$
$$- \frac{R_o\alpha d_{\mathrm{E},m}^3 - R_\oplus\beta d_{\mathrm{s},z}^3 + d_{\mathrm{E},m}d_{\mathrm{s},z}^3\psi + d_{\mathrm{E},m}^3 d_{\mathrm{s},z}\psi + R_o\alpha d_{\mathrm{E},m}d_{\mathrm{s},z}^2 - R_\oplus\beta d_{\mathrm{E},m}^2 d_{\mathrm{s},z}}{2r^4}$$
$$\left. - \frac{R_o\alpha d_{\mathrm{E},m}^2 d_{\mathrm{s},z}\psi - R_\oplus\beta d_{\mathrm{E},m}d_{\mathrm{s},z}^2\psi - R_\oplus R_o\alpha\beta d_{\mathrm{E},m}d_{\mathrm{s},z}}{r^4}\right). \quad \text{(C.5)}$$

C.2. Full Expression of Eq. (4.43)

Applying the substitution Δ_{mz} as defined in (4.34) to (4.43), the full expression of the differences between the second order Taylor polynomials is given by

$$\left|\left(P_{21}^{(2)} - P_{11}^{(2)}\right) - \left(P_{22}^{(2)} - P_{12}^{(2)}\right)\right| = \frac{d_\mathrm{E}d_\mathrm{s}}{8r^3} \cdot \left|8R_\oplus R_o\alpha\beta + 8\psi r^2 - \left(3M^2 - 12M + 13\right) d_\mathrm{E}^2\psi \right.$$
$$- \left(3Z^2 - 12Z + 13\right) d_\mathrm{s}^2\psi - (2MZ - 4M - 4Z + 8)\, d_\mathrm{E}d_\mathrm{s}\left(1 + 2\psi^2\right) + (8M - 16)\, d_\mathrm{E}R_o\alpha\psi$$
$$\left. - (8Z - 16)\, d_\mathrm{s}R_\oplus\beta\psi + (4Z - 8)\, d_\mathrm{s}R_o\alpha - (4M - 8)\, d_\mathrm{E}R_\oplus\beta\right|. \quad \text{(C.6)}$$

Considering the Full Multiplexing System (FMS) ($M = Z$), (C.6) can be further simplified to

$$\left|\left(P_{21}^{(2)} - P_{11}^{(2)}\right) - \left(P_{22}^{(2)} - P_{12}^{(2)}\right)\right| = \frac{d_\mathrm{E}d_\mathrm{s}}{8r^3} \cdot \left|8R_\oplus R_o\alpha\beta + 8\psi r^2 \right.$$
$$- \left(3M^2 - 12M + 13\right)\left(d_\mathrm{E}^2\psi + d_\mathrm{s}^2\psi\right) - 2\,(M-2)^2\, d_\mathrm{E}d_\mathrm{s}\left(1 + 2\psi^2\right)$$
$$\left. - 8\,(M-2)\,(d_\mathrm{s}R_\oplus\beta - d_\mathrm{E}R_o\alpha)\,\psi - 4\,(M-2)\,(d_\mathrm{E}R_\oplus\beta + d_\mathrm{s}R_o\alpha)\right|. \quad \text{(C.7)}$$

If additionally $M = Z = 2$ is assumed, (C.7) finally results in

$$\left|\left(P_{21}^{(2)} - P_{11}^{(2)}\right) - \left(P_{22}^{(2)} - P_{12}^{(2)}\right)\right| = \frac{d_\mathrm{E}d_\mathrm{s}}{r}\left|\psi + R_\oplus R_o\alpha\beta/r^2 - 1/8\left(d_\mathrm{E}^2 + d_\mathrm{s}^2\right)\psi/r^2\right|, \quad \text{(C.8)}$$

which equals (4.44) in Section 4.3.

List of Operators and Symbols

List of Operators

$\mathbf{A}^{\mathrm{H}}$	conjugate transpose of a matrix $\mathbf{A}$
$\mathrm{diag}\{.\}$	diagonal operator
$\mathbf{A}^{\mathrm{T}}$	transposed of a matrix $\mathbf{A}$
$\mathrm{E}\{X\}$	expectated value of random variable X
$\det(\mathbf{A})$	determinant of matrix $\mathbf{A}$
$\max\{.\}$	maximum of a set of variables
$\min\{.\}$	minimum of a set of variables
$\lvert a\rvert$	absolute value of scalar a
$\lVert\mathbf{A}\rVert$	norm of matrix or vector $\mathbf{A}$
$\arg\{a\}$	argument of complex scalar a
$\mathcal{P}(A)$	probability of event A
$\mathrm{tr}\{\mathbf{A}\}$	trace of matrix $\mathbf{A}$
$J_a(b)$	Bessel function of first kind, order a and argument b
$[\mathbf{A}]_{m,n}$	entry of matrix $\mathbf{A}$ at row m and column n
e	Euler's constant
$\mathrm{j} = \sqrt{-1}$	Imaginary unit
$\odot$	elementwise product of two vectors / matrices

List of Symbols

$c_0 = 299\,792\,458\,\mathrm{m/s}$	speed of light in vacuum
$\mathbf{B}$	precoding matrix
$\mathbf{Q}_1, \mathbf{Q}_2$	matrix with ones only on odd / even enries of main-diagonal
$\bar{\mathbf{Q}}_1$	block diagonal matrix containing matrix $\mathbf{Q}_1$
$\lambda, \lambda_{\mathrm{u}}, \lambda_{\mathrm{d}}$	carrier wavelength, uplink, downlink
$f, f_{\mathrm{u}}, f_{\mathrm{d}}$	carrier frequency, uplink, downlink
$\triangle f$	frequency spacing to carrier frequency
$h_{\mathrm{u},mn}, h_{\mathrm{d},mn}$	LOS channel coefficient between antenna pair m,n, uplink, downlink

$\widetilde{\mathbf{H}}, \widetilde{\mathbf{H}}_{\mathrm{u}}, \widetilde{\mathbf{H}}_{\mathrm{d}}$	MIMO channel transfer matrix, uplink, downlink
$\mathbf{H}_{\mathrm{norm}}, \mathbf{H}_{\mathrm{fro}}$	normalized channel matrix, Frobenius normalized channel matrix
$\mathbf{I}_M$	identity matrix of dimension $M \times M$
$\mathbf{F}, \widetilde{\mathbf{F}}$	satellite transfer matrix, optimal relaying matrix
$\hat{\mathbf{H}}$	estimated channel transfer matrix
$\hat{\mathbf{H}}_{\mathrm{norm}}, \hat{\mathbf{H}}_{\mathrm{fro}}$	estimated normalized channel transfer matrix
$a, a_{\mathrm{u}}, a_{\mathrm{d}}$	free space path loss, free space path loss uplink, downlink
$a_{mn}, a_{\mathrm{u},mn}, a_{\mathrm{d},mn}$	free space path loss between receive antenna m and transmit antenna n, uplink, downlink
$a_{\mathrm{s},z}$	amplitude satellite transfer coefficient
$\upsilon_{\mathrm{s},z}$	satellite phase shift
φ	channel phase
t, t_0	time, time at epoch
k, l, m, n, z, w	indices, counting variables
T_s	symbol period
B_w	system bandwidth
$R_o = 42\,164.2\,\mathrm{km}$	radius of ideal geostationary orbit
$R_\oplus = 6378.1\,\mathrm{km}$	mean equatorial earth radius
$r_{\min} = 35\,786.1\,\mathrm{km}$	geostationary satellite altitude above equator
r	distance between earth station ULA center and satellite ULA center
$r_{mn}, r_{\mathrm{u},mn}, r_{\mathrm{d},mn}$	geometrical distance between antenna pair m,n, uplink, downlink
$\bar{r}$	mean geometrical distance between all antenna pairs
$\triangle r$	relative increase of $r_{\min}$ in dependence on earth station ULA relative to satellite ULA
r_{diff}	difference between path lengths
$\triangle r_{\mathrm{diff}}$	deviation to difference between path lengths
$L_{\mathrm{E},m}, L_{\mathrm{s},n}$	geometrical length of earth station antenna array with m elements, respectively, satellite antenna array with n elements
α, β, ψ	substitution of sum of angular terms
Δ_{mn}	substitution of sum of angular terms between receive antenna m and transmit antenna n
a_{rf}	array reduction factor
$P^{(n)}$	Taylor polynom of order n
$R^{(n)}$	Remainder of Taylor polynom of order n

$\triangle R^{(n)}$	sum of Remainders of Taylor polynom of order n
$e_{M\times Z}$	absolute error of difference between path lengths for arbitrary $M \times N$ systems
e_r	absolute error of difference between path lengths due to multiple approximations
$\varepsilon_{M\times Z}$	relative error of difference between path lengths for arbitrary $M \times N$ systems
ε_{e_r}	relative error of difference between path lengths due to multiple approximations
$\varepsilon_{r_{\text{diff}}}$	relative deviation from optimal antenna arrangement
$\varepsilon_{C_{M\times Z}}$	relative capacity error due to arbitrary $M \times N$ systems
$\varepsilon_{C_{e_r}}$	relative capacity error due to multiple approximations
$\theta_{\text{E}}, \theta_{\text{s}}$	geographical longitude earth station ULA, respectively, satellite ULA
$\triangle\theta$	relative longitude between satellite ULA and earth station ULA
$\theta_{\text{s},n}$	geographical longitude of n-th satellite
$\mathbf{a}_{\text{E},m}, \mathbf{a}_{\text{s},n}$	position vector in cartesian coordinates of m-th earth station antenna, respectively, of n-th satellite antenna
$x_{\text{s},n}, y_{\text{s},n}, z_{\text{s},n}$	x-, y- and z-coordinate of n-th satellite antenna position
$x_{\text{E},m}, y_{\text{E},m}, z_{\text{E},m}$	x-, y- and z-coordinate of m-th earth station antenna position
$d_{\text{E}}, d_{\text{s}}$	earth station antenna spacing, satellite antenna spacing
$\triangle d_{\text{E}}, \triangle d_{\text{s}}$	deviation from earth station antenna spacing / satellite antenna spacing
$d_{\text{E}}^{(\text{opt})}, d_{\text{s}}^{(\text{opt})}$	optimal earth station antenna spacing / satellite antenna spacing
$d_{\text{E},m}, d_{\text{s},n}$	spacing with respect to array center of m-th earth station antenna, respectively, n-th satellite antenna
$\triangle\theta_{\text{s}}$	satellite spacing in longitude in orbit
$\delta_{\text{E}}, \delta_{\text{s}}$	ULA orientation angle of earth station array, respectively, satellite array
N, M, Z	number of antennas at the transmitter, the receiver and the satellite
$Z_{\text{refl}}, Z_{\text{t}}$	number of satellite reflectors, number of satellite feeds
Z_{r}	number of satellite receive antennas
$V, W, V_{\text{u}}, W_{\text{u}}, V_{\text{d}}, W_{\text{d}}$	maximum and minimum number of antennas (uplink and downlink)

v	integer represents the periodicity of optimal antenna arrangements
$\mathbf{D}, \mathbf{D}_\mathrm{u}, \mathbf{D}_\mathrm{d}$	matrix containing the atmospheric impairments, uplink, downlink
$\mathbf{U}, \mathbf{U}_\mathrm{u}, \mathbf{U}_\mathrm{d}$	unitary matrix containing left-singular column vectors, uplink, downlink
$\mathbf{V}, \mathbf{V}_\mathrm{u}, \mathbf{V}_\mathrm{d}$	unitary matrix containing right-singular column vectors, uplink, downlink
$\mathbf{G}, \mathbf{G}_\mathrm{u}, \mathbf{G}_\mathrm{d}$	matrix containing antenna depointing losses, uplink, downlink
$\mathbf{E}$	matrix containing complex unit numbers
$\mathbf{\Gamma}, \mathbf{\Gamma}_\mathrm{u}, \mathbf{\Gamma}_\mathrm{d}$	matrix containing eigenvalues of the channel, uplink, downlink
$\gamma_w, \gamma_{\mathrm{u},w}, \gamma_{\mathrm{d},w}$	w-th eigenvalue, uplink, downlink
$\eta_\mathrm{u}, \eta_\mathrm{d}$	noise contribution in uplink, downlink
$\boldsymbol{\eta}, \boldsymbol{\eta}_\mathrm{u}, \boldsymbol{\eta}_\mathrm{d}$	vector containing total noise contribution, uplink noise contribution, downlink noise contribution
$\bar{\boldsymbol{\eta}}$	total noise vector including inter-stream interference
$\eta_m, \eta_{\mathrm{u},m}, \eta_{\mathrm{d},m}$	noise contribution at m-the receive antenna of the total link, the uplink and the downlink, respectively
$\sigma^2_{\boldsymbol{\eta}}, \sigma^2_{\boldsymbol{\eta}_\mathrm{u}}, \sigma^2_{\boldsymbol{\eta}_\mathrm{d}}$	variance of total noise contribution, uplink noise contribution, downlink noise contribution
$\sigma^2_{\bar{\boldsymbol{\eta}}k}$	variance of total noise including inter-stream interference of user k
$\mathbb{A}$	modulation alphabet
$\mathbf{s}$	vector containing transmit symbols
s_n	transmit symbol at n-th transmit antenna
$\mathbf{x}, \mathbf{x}_\mathrm{u}, \mathbf{x}_\mathrm{d}$	vector containing transmit signals, transmit signal vector uplink / downlink
$x_n, x_{\mathrm{u},n}, x_{\mathrm{d},n}$	transmit signal at n-th transmit antenna, uplink transmit signal, downlink transmit signal
P_t, P_d	equivalent isotropically radiated power (EIRP), uplink EIRP, downlink EIRP
$\mathbf{R}$	covariance matrix
$\mathbf{R}_\mathbf{x}, \mathbf{R}_{\mathbf{x}_\mathrm{u}}, \mathbf{R}_{\mathbf{x}_\mathrm{d}}$	covariance matrix transmit signal, uplink, downlink
$\mathbf{R}_{\boldsymbol{\eta}}, \mathbf{R}_{\boldsymbol{\eta}_\mathrm{u}}, \mathbf{R}_{\boldsymbol{\eta}_\mathrm{d}}$	covariance matrix noise signal, uplink, downlink
$\hat{\mathbf{s}}$	vector containing the receive symbols
$\hat{s}_m$	receive symbol at m-th antenna
$\mathbf{y}, \mathbf{y}_\mathrm{u}, \mathbf{y}_\mathrm{d}$	vector containing receive signals, uplink, downlink
$y_m, y_{\mathrm{u},m}$	receive signal at m-the receive antenna, uplink

C_B	channel capacity in b/s
C	channel capacity normalized by system bandwidth
$C_{\text{opt}}, C_{\text{key}}$	optimal spectral efficiency, keyhole spectral efficiency
C_{SISO}	spectral efficiency SISO channel
$\hat{C}$	estimated spectral efficiency
$\hat{C}_{\text{norm}}, \hat{C}_{\text{fro}}$	estimated spectral efficiency calculated with $\hat{\mathbf{H}}_{\text{norm}}$, $\hat{\mathbf{H}}_{\text{fro}}$
ρ	signal-to-noise ratio
$\rho_r, \rho_{r,\text{dB}}$	receive SNR, receive SNR in dB
$\mathbf{h}_{\text{r},k}, \mathbf{h}_{\text{c},k}$	k-th row vector of $\mathbf{H}$, k-th column vector of $\mathbf{H}$
$C_{M\times Z}$	channel capacity for which path length difference equals $v\lambda/V$
C_{e_r}	actual channel capacity according to (4.46)
σ_{p}	root mean square (RMS) phase
d_{h}	distance of two paths at altitude h_{a}
h_{a}	altitude above Earth's surface
$\triangle\phi_m$	relative atmospheric phase offset between two paths at m-th antenna
ς_n	atmospheric impairment at n-th transmit antenna
A_n	atmospheric path attenuation in dB at n-th antenna
ξ_n	atmospheric phase disturbance at n-th antenna
$\widetilde{C}$	impaired channel capacity
$\widetilde{\mathbf{H}}_{\text{u},l}$	uplink channel matrix at frequency l
n_{dr}	field decreasing rate
T_{e}	edge taper
$\triangle C$	spectral efficiency normalized by C_{opt}
$\vartheta_{mn}, \vartheta_{mn}^{(\text{E})}, \vartheta_{mn}^{(\text{s})}$	off-axis angle from point of boresight between antenna pair m,n, earth station antenna, satellite antenna
D	antenna diameter
$\triangle f$	frequency difference
K, K_{tot}, K^g	number of users, total number of users, number of users in group g
N_{G}	number of user groups
W_{d}	user bandwidth
c_{mn}	total channel coefficient between antenna pair m,n
$(C/N)_{\text{bc}}$	carrier-to-noise ratio at beam center
$\mathcal{I}, \mathcal{I}_k$	mutual information, mutual information k-th user
$\mathcal{R}, \mathcal{R}_k, \mathcal{R}_k^g$	sum achievable rate, achievable rate of user k, achievable rate of user k of group g

Acronyms

G/T Figure of Merit. 96, 99

ADC analog-to-digital converter. 32

ASI adjacent satellite interference. 8, 72

ASIC Application-Specific Integrated Circuit. 32

AWGN additive white Gaussian noise. 14, 69

BEP bit error probability. 6

CAZAC constant amplitude zero autocorrelation. 31

CCI co-channel interference. 3

CDF cumulative distribution function. 83, 85, 123

CINR carrier-to-interference-noise-ratio. 3

CoC center of coverage. 70

CSI channel state information. 23–25, 31, 93

DAC digital-to-analog converter. 32

DSP digital signal processor. 31, 32

DTP Digital Transparent Payload. 32, 88

DVB-S2X DVB-S2 extensions. 93

ECEF Earth-centered Earth-fixed. 46, 48, 121

EIRP equivalent isotropically radiated power. 14, 15, 23, 26, 27, 29, 77, 88, 93, 94, 96, 99–101, 123

EM electromagnetic. 19, 22

ESOMP earth station on mobile platform. 2

FDMA frequency division multiple access. 91

FFR full frequency reuse. 3, 9, 90, 91, 96, 98–100, 104, 123

FMS Full Multiplexing System. 27, 28, 30, 34, 35, 86, 114

FPGA Field Programmable Gate Array. 32

FR4 four color frequency reuse. 3, 6, 96, 99, 100, 104

FSS fixed satellite service. 1, 2, 6, 7, 9, 19, 23, 56, 69, 72, 87, 89, 103, 104

GDS Ground Diversity System. 28–30, 34, 35, 86

GEO geostationary earth orbit. 1, 7, 10, 16, 22, 35, 41, 46, 47, 49, 50, 52, 62, 66, 76, 79, 82, 87, 88, 103, 109, 122

GPS Global Positioning System. 79, 80

GSDS Ground and Satellite Diversity System. 29

HD high-definition. 2

HPA high power amplifier. 32, 93

HTS high-throughput satellite. 2–4, 6, 9, 10, 28, 32, 46, 85, 88, 89, 91, 92, 94, 95, 98, 101, 104

i.i.d. independent and identically distributed. 14

IF Intermediate Frequency. 32

IMUX Input Multiplexer. 32

IP Internet Protocol. 1, 2

LLMF Low-Level Matched Filter. 31, 32, 88, 121

LOS Line-of-Sight. 6, 7, 9, 18–22, 31, 33, 35, 37, 45, 52, 68, 72, 83, 85, 86, 103

LTE Long Term Evolution. 4, 6

MADOC Multiple Antenna Downlink Orthogonal Clustering. 9

MIMO multiple-input multiple-output. 4–10, 13–16, 19, 21–26, 28, 30–35, 37, 38, 40, 41, 43, 45–48, 52, 54–56, 61, 62, 64–72, 74, 75, 78, 80–89, 91–101, 103, 104, 109, 110, 119, 121–123

MMSE minimum mean square error. 4

MU-MIMO multiuser MIMO. 10, 33, 37, 96, 99, 100, 104

NAF naive-amplify-and-forward. 14, 24, 30, 34, 86

NASA National Aeronautics and Space Administration. 89

OMUX Output Multiplexer. 32

OPA **O**ptimal **P**ositioning of the MIMO **A**ntennas. 52, 87, 103, 104

PAPR peak-to-average power ratio. 32

PWM plane wave model. 19, 32, 37

RF radio frequency. 89

RMS root mean square. 83–85

SAF smart-amplify-and-forward. 26, 30–32, 34, 86, 88, 121

SATCOM satellite communication. 1, 8–10, 37, 43, 56, 72, 87, 92, 104, 109

SC-FDE single carrier - frequency domain equalizer. 8

SDMA space division multiple access. 91

SDS Satellite Diversity System. 29, 30, 34

SES Société Européenne des Satellites. 1

SFPB single-feed per beam. 91, 95

SIC successive interference cancellation. 4

SISO single-input single-output. 6, 8, 10, 14, 15, 25, 33, 70, 80, 86, 96–100, 104

SNR signal-to-noise ratio. 8, 26–29, 33, 34, 44, 46, 56, 61, 63, 66, 68, 70, 71, 77, 81, 85, 86, 88, 94, 96–98, 100, 106, 107, 112, 124

SVD singular value decomposition. 24

SWM spherical wave model. 7, 19, 103

TDMA time division multiple access. 91, 92

TV television. 1, 2, 98

UCA uniform circular array. 8

UHD ultra-high-definition. 2

ULA uniform linear array. 7, 39–43, 47–50, 57, 58, 62, 68, 70, 77, 81, 92, 95, 109, 111, 112, 121

UPC Uplink Power Control. 31

UT user terminal. 33, 91, 92, 94, 99, 101

VHTS very high throughput satellite. 104

VoD Video-on-Demand. 1

w.l.o.g. without loss of generality. 18, 22, 43, 47

WLAN wireless local area network. 7

ZF zero forcing. 4, 94

List of Tables

List of Figures

Bibliography

[ADMPN12] J. Arnau, B. Devillers, C. Mosquera, and A. Pérez-Neira, "Performance study of multiuser interference mitigation schemes for hybrid broadband multibeam satellite architectures," *EURASIP J. Wirel. Commun. Netw.*, vol. 2012, no. 1, p. 132, dec 2012.

[ALB+11] P.-D. Arapoglou, K. Liolis, M. Bertinelli, A. Panagopoulos, P. Cottis, and R. De Gaudenzi, "MIMO over Satellite: A Review," *IEEE Commun. Surv. Tutorials*, vol. 13, no. 1, pp. 27–51, 2011.

[All11] J. E. Allnutt, *Satellite-to-ground radiowave propagation*, 2nd ed., ser. Electromagnetic Waves Series 54. The Institution of Engineering and Technology, 2011.

[AS83] M. Abramowitz and I. A. Stegun, *Handbook of Mathematical Functions: with Formulas, Graphs, and Mathematical Tables*, 9th ed., M. Abramowitz and I. A. Stegun, Eds. Dover Publications, 1983.

[BC02] N. Benvenuto and G. Cherubini, *Algorithms for Communications Systems and their Applications*, 4th ed. John Wiley & Sons, 2002.

[BCC+07] E. Biglieri, R. Calderbank, A. Constantinides, A. Goldsmith, A. Paulraj, and H. V. Poor, *MIMO Wireless Communications*. Cambridge University Press, 2007.

[BOO05] F. Bohagen, P. Orten, and G. Oien, "Construction and capacity analysis of high-rank line-of-sight MIMO channels," in *IEEE Wirel. Commun. Netw. Conf. 2005*, vol. 1. IEEE, 2005, pp. 432–437.

[BOO07] ——, "Design of Optimal High-Rank Line-of-Sight MIMO Channels," *IEEE Trans. Wirel. Commun.*, vol. 6, no. 4, pp. 1420–1425, apr 2007.

[BOO09] ——, "On spherical vs. plane wave modeling of line-of-sight MIMO channels," *IEEE Trans. Commun.*, vol. 57, no. 3, pp. 841–849, mar 2009.

[CB94] C. Chao and H. Bernstein, "Onboard stationkeeping of geosynchronous satellite using a global positioning system receiver," *J. Guid. Control. Dyn.*, vol. 17, no. 4, pp. 778–786, jul 1994.

[CCO15] D. Christopoulos, S. Chatzinotas, and B. Ottersten, "Multicast Multigroup Precoding and User Scheduling for Frame-Based Satellite Communications," *IEEE Trans. Wirel. Commun.*, vol. 14, no. 9, pp. 4695–4707, sep 2015.

[CCZ+12] D. Christopoulos, S. Chatzinotas, G. Zheng, J. Grotz, and B. Ottersten, "Linear and nonlinear techniques for multibeam joint processing in satellite communications," *EURASIP J. Wirel. Commun. Netw.*, vol. 2012, no. 1, p. 162, dec 2012.

[CIS17] CISCO, "Cisco Visual Networking Index: Forecast and Methodology, 2016–2021," Cisco, Tech. Rep., 2017.

[CKL04] M. Chouayakh, A. Knopp, and B. Lankl, "On the Boundaries of the MIMO-Channel-Capacity with a Focus on Line-of-Sight-Connections," *Facta Univ.*, vol. 17, pp. 185–197, 2004.

[Cla45] A. C. Clarke, "Extra-Terrestrial Relays: Can Rocket Stations Give World Wide Radio Coverage?" *Wirel. World*, pp. 305 —- 308, 1945.

[Col85] R. E. Collin, *Antennas and Radiowave Propagation.* McGraw-Hill, 1985.

[dB17] F. J. de Bruijn, "GUIDANCE CONTROL AND DYNAMICS OF A NEW GENERATION OF GEOSTATIONARY SATELLITES," Ph.D. dissertation, TU Delft, 2017.

[DF99] P. Driessen and G. Foschini, "On the capacity formula for multiple input-multiple output wireless channels: a geometric interpretation," *IEEE Trans. Commun.*, vol. 47, no. 2, pp. 173–176, feb 1999.

[DK18] T. Delamotte and A. Knopp, "Outage Analysis of a MIMO-Based Smart Gateway Architecture," in *2018 IEEE Int. Conf. Commun.*, may 2018, pp. 1–6.

[DK19] ——, "Distributed Gateway Antennas for Q/V-band MIMO Feeder Links," *IEEE Trans. Aerosp. Electron. Syst.*, vol. under revi, 2019.

[DSKL10] V. Dantona, R. T. Schwarz, A. Knopp, and B. Lankl, "Uniform circular arrays: The key to optimum channel capacity in mobile MIMO satellite links," *ASMS 2010 5th Adv. Satell. Multimed. Syst. Work.*, pp. 421–428, sep 2010.

[DSSK18] T. Delamotte, R. T. Schwarz, K.-U. Storek, and A. Knopp, "MIMO Feeder Links for High Throughput Satellites," in *WSA 2018; 22nd Int. ITG Work. Smart Antennas*. VDE, 2018, pp. 1–8.

[ETC+11] B. G. Evans, P. T. Thompson, G. E. Corazza, A. Vanelli-Coralli, and E. A. Candreva, "1945–2010: 65 Years of Satellite History From Early Visions to Latest Missions," *Proc. IEEE*, vol. 99, no. 11, pp. 1840–1857, nov 2011.

[Eur14] European Telecommunications Standards Institute, "Digital Video Broadcasting (DVB); Second generation framing structure, channel coding and modulation system for Broadcasting, Interactive Services, News Gathering and other broadband satellite applications; Part 2: DVB-S2 Extension (DVB-S2X)," 2014.

[EWL+05] B. Evans, M. Werner, E. Lutz, M. Bousquet, G. Corazza, G. Maral, and R. Rumeau, "Integration of satellite and terrestrial systems in future multimedia communications," *IEEE Wirel. Commun.*, vol. 12, no. 5, pp. 72–80, oct 2005.

[FG98] G. Foschini and M. Gans, "On Limits of Wireless Communications in a Fading Environment when Using Multiple Antennas," *Wirel. Pers. Commun.*, vol. 6, no. 3, pp. 311–335, 1998.

[FTA+16] H. Fenech, A. Tomatis, S. Amos, V. Soumpholphakdy, and J. L. Serrano Merino, "Eutelsat HTS systems," *Int. J. Satell. Commun. Netw.*, vol. 34, no. 4, pp. 503–521, jul 2016.

[FVCC+01] F. Fontan, M. Vazquez-Castro, C. Cabado, J. Garcia, and E. Kubista, "Statistical modeling of the LMS channel," *IEEE Trans. Veh. Technol.*, vol. 50, no. 6, pp. 1549–1567, 2001.

[Gay09] J.-D. Gayrard, "Terabit Satellite: Myth or Reality?" in *2009 First Int. Conf. Adv. Satell. Sp. Commun.* IEEE, jul 2009, pp. 1–6.

[GBGP02] D. Gesbert, H. Bolcskei, D. Gore, and A. Paulraj, "Outdoor MIMO wireless channels: models and performance prediction," *IEEE Trans. Commun.*, vol. 50, no. 12, pp. 1926–1934, dec 2002.

[GCO12] Gan Zheng, S. Chatzinotas, and B. Ottersten, "Generic Optimization of Linear Precoding in Multibeam Satellite Systems," *IEEE Trans. Wirel. Commun.*, vol. 11, no. 6, pp. 2308–2320, jun 2012.

[GVCTM17] A. Guidotti, A. Vanelli-Coralli, G. Taricco, and G. Montorsi, "User Clustering for Multicast Precoding in Multi-Beam Satellite Systems," *arXiv Prepr. arXiv1706.09482*, pp. 1–30, jun 2017.

[GYW16] Z. Guo, Y. Yilmaz, and X. Wang, "Transmitter-Centric Channel Estimation and Low-PAPR Precoding for Millimeter-Wave MIMO Systems," *IEEE Trans. Commun.*, vol. 64, no. 7, pp. 2925–2938, jul 2016.

[Har95] S. Hardacre, "Control of Colocated Geostationary Satellites," Ph.D. dissertation, Cranfield University, 1995.

[HGF+17] A. Hofmann, R. Glein, L. Frank, R. Wansch, and A. Heuberger, "Reconfigurable on-board processing for flexible satellite communication systems using FPGAs," in *2017 Top. Work. Internet Sp.* IEEE, jan 2017, pp. 1–4.

[HK03] T. Haustein and U. Kruger, "Smart geometrical antenna design exploiting the LOS component to enhance a MIMO system based on rayleigh-fading in indoor scenarios," in *14th IEEE Proc. Pers. Indoor Mob. Radio Commun. 2003. PIMRC 2003.*, vol. 2. IEEE, sep 2003, pp. 1144–1148.

[HKO+08] C. Hofmann, A. Knopp, D. Ogermann, R. Schwarz, and B. Lankl, "Deficiencies of common MIMO channel models with regard to indoor Line-of-Sight channels," in *2008 IEEE 19th Int. Symp. Pers. Indoor Mob. Radio Commun.* IEEE, sep 2008, pp. 1–6.

[HSK17] C. A. Hofmann, R. T. Schwarz, and A. Knopp, "Multisatellite UHF MIMO Channel Measurements," *IEEE Antennas Wirel. Propag. Lett.*, vol. 16, pp. 2481–2484, 2017.

[HSSK16] C. Hofmann, K.-U. Storek, R. T. Schwarz, and A. Knopp, "Spatial MIMO over satellite: A proof of concept," in *2016 IEEE Int. Conf. Commun.* Kuala Lumpur, Malaysia: IEEE, may 2016, pp. 1–6.

[IN05a] M. T. Ivrlac and J. A. Nossek, "MIMO Performance Gains – Antenna Gain, Diversity Gain, and Multiplexing Gain," in *Third Int. Conf. Syst. Signals Devices*, 2005.

[IN05b] M. Ivrlac and J. Nossek, "Mimo Perfomance Measures -A Signal Processing Point of View," in *2005 18th Int. Conf. Appl. Electromagn. Commun.* IEEE, 2005, pp. 1–4.

[Int03] International Telecommunication Union, "Radiation diagrams for use as design objectives for antennas of earth stations operating with geostationary satellites," 2003. [Online]. Available: https://www.itu.int/rec/R-REC-S.580/en

[Ipp08] L. J. Ippolito, *Satellite Communications Systems Engineering - Atmospheric Effects, Satellite Link Design and System Performance*. John Wiley & Sons, 2008.

[JI05] J.-S. Jiang and M. Ingram, "Spherical-wave model for short-range MIMO," *IEEE Trans. Commun.*, vol. 53, no. 9, pp. 1534–1541, sep 2005.

[JVPN16] V. Joroughi, M. Vazquez, and A. Perez-Neira, "Precoding in Multigateway Multibeam Satellite Systems," *IEEE Trans. Wirel. Commun.*, pp. 1–1, 2016.

[JVPN17] V. Joroughi, M. A. Vazquez, and A. I. Perez-Neira, "Generalized Multicast Multibeam Precoding for Satellite Communications," *IEEE Trans. Wirel. Commun.*, vol. 16, no. 2, pp. 952–966, feb 2017.

[Kam08] K.-D. Kammeyer, *Nachrichtenübertragung*, 4th ed. Vieweg + Teubner, 2008.

[Kaw90] S. Kawase, "Intersatellite tracking methods for clustered geostationary satellites," *IEEE Trans. Aerosp. Electron. Syst.*, vol. 26, no. 3, pp. 469–474, may 1990.

[KCL05] A. Knopp, M. Chouayakh, and B. Lankl, "Capacity Optimization and Modeling ofFrequency Selective WLAN Indoor MIMOChannels Based on Measured Data," in *IEEE Conf. Syst. Signals Devices, SSD*, 2005, pp. 21–24.

[KCS+00] M. Kirkland, R. Carlos, X.-M. Shao, X. DeHaven, and A. Jacobson, "The Los Alamos microwave interferometer," *IEEE Trans. Geosci. Remote Sens.*, vol. 38, no. 2, pp. 849–857, mar 2000.

[KET+14] A. Kyrgiazos, B. Evans, P. Thompson, P. T. Mathiopoulos, and S. Papaharalabos, "A terabit/second satellite system for European broadband access: a feasibility study," *Int. J. Satell. Commun. Netw.*, vol. 32, no. 2, pp. 63–92, mar 2014.

[KFC+00] E. Kubista, F. Fontan, M. Castro, S. Buonomo, B. Arbesser-Rastburg, and J. Baptista, "Ka-band propagation measurements and

statistics for land mobile satellite applications," *IEEE Trans. Veh. Technol.*, vol. 49, no. 3, pp. 973–983, may 2000.

[KHL+12] R. S. Kimberk, T. R. Hunter, P. S. Leiker, R. Blundell, G. U. Nystrom, G. R. Petitpas, J. Test, R. W. Wilson, P. Yamaguchi, and K. H. Young, "A Multi-Baseline 12 GHz Atmospheric Phase Interferometer with One Micron Path Length Sensitivity," *J. Astron. Instrum.*, vol. 01, no. 01, p. 23, dec 2012.

[KIK86] T. Kasuga, M. Ishiguro, and R. Kawabe, "Interferometric measurement of tropospheric phase fluctuations at 22 GHz on antenna spacings of 27 to 540 m," *IEEE Trans. Antennas Propag.*, vol. 34, no. 6, pp. 797–803, jun 1986.

[Kli98] M. Kline, *Calculus: An Intuitive and Physical Approach*, 2nd ed. Dover, 1998.

[KLS13] A. Knopp, B. Lankl, and R. Schwarz, "Verfahren und Einrichtung zur MIMO-Datenübertragung mit einer Höhenplattform," 56073 Koblenz, nov 2013. [Online]. Available: https://register.dpma.de/DPMAregister/pat/register?AKZ=1020130009030

[Kno08] A. Knopp, "Bandbreiteneffizienz von MIMO Funkkanälen in Innenräumen," Ph.D. dissertation, Universität der Bundeswehr München, nov 2008.

[KSH+07] A. Knopp, R. T. Schwarz, C. A. Hofmann, M. Chouayakh, and B. Lankl, "Measurements on the Impact of Sparse Multipath Components on the LOS MIMO Channel Capacity," in *2007 4th Int. Symp. Wirel. Commun. Syst.* IEEE, oct 2007, pp. 55–60.

[KSL10] A. Knopp, R. T. Schwarz, and B. Lankl, "On the capacity degradation in broadband MIMO satellite downlinks with atmospheric impairments," *IEEE Int. Conf. Commun.*, pp. 1–6, may 2010.

[KSL11] ——, "MIMO system implementation with displaced ground antennas for broadband military SATCOM," *Proc. - IEEE Mil. Commun. Conf. MILCOM*, pp. 2069–2075, nov 2011.

[KSL13] ——, "Secure MIMO SATCOM transmission," *Proc. - IEEE Mil. Commun. Conf. MILCOM*, pp. 284–288, 2013.

[KSO+08] A. Knopp, R. T. Schwarz, D. Ogermann, C. A. Hofmann, and B. Lankl, "Satellite system design examples for maximum mimo

spectral efficiency in los channels," in *GLOBECOM - IEEE Glob. Telecommun. Conf.*, 2008, pp. 2890–2895.

[Li14] H. Li, *Geostationary Satellites Collocation.* Springer, 2014.

[LLT14] K. Y. Lau, G. F. Lutes, and R. L. Tjoelker, "Ultra-Stable RF-Over-Fiber Transport in NASA Antennas, Phased Arrays and Radars," *J. Light. Technol.*, vol. 32, no. 20, pp. 3440–3451, oct 2014.

[LT03] Lizhong Zheng and D. Tse, "Diversity and multiplexing: a fundamental tradeoff in multiple-antenna channels," *IEEE Trans. Inf. Theory*, vol. 49, no. 5, pp. 1073–1096, may 2003.

[Lüt96] H. Lütkepohl, *Handbook of Matrices.* John Wiley & Sons, 1996.

[MAG+99] V. Manikonda, P. Arambel, M. Gopinathan, R. Mehra, and F. Hadaegh, "A model predictive control-based approach for spacecraft formation keeping and attitude control," in *Proc. 1999 Am. Control Conf. (Cat. No. 99CH36251).* IEEE, 1999, pp. 4258–4262 vol.6.

[MB09] G. Maral and M. Bousquet, *Satellite Communications Systems: Systems, Techniques and Technology*, 5th ed. John Wiley & Sons Ltd., 2009.

[MDAN13] D. D. Morabito, L. R. D'Addario, R. J. Acosta, and J. A. Nessel, "Tropospheric delay statistics measured by two site test interferometers at Goldstone, California," *Radio Sci.*, vol. 48, no. 6, pp. 729–738, nov 2013.

[MSD18] Z. Mokhtari, M. Sabbaghian, and R. Dinis, "Massive MIMO Downlink Based on Single Carrier Frequency Domain Processing," *IEEE Trans. Commun.*, vol. 66, no. 3, pp. 1164–1175, mar 2018.

[MVCS11] V. Mignone, M. A. Vazquez-Castro, and T. Stockhammer, "The Future of Satellite TV: The Wide Range of Applications of the DVB-S2 Standard and Perspectives," *Proc. IEEE*, vol. 99, no. 11, pp. 1905–1921, nov 2011.

[NIM97] NIMA, "Department of Defense World Geodetic System 1984, Its Definition and Relationships With Local Geodetic Systems," National Imagery and Mapping Agency, Tech. Rep., 1997.

[Pel10] J. Pelton, "The start of commercial satellite communications [History of communications," *IEEE Commun. Mag.*, vol. 48, no. 3, pp. 24–31, mar 2010.

[Ray79] Rayleigh, "XXXI. Investigations in optics, with special reference to the spectroscope," *London, Edinburgh, Dublin Philos. Mag. J. Sci.*, vol. 8, no. 49, pp. 261–274, oct 1879.

[RCB16] B. Ramamurthy, W. G. Cowley, and G. Bolding, "MIMO Applicability to UHF SATCOM," in *2016 IEEE Glob. Commun. Conf.* IEEE, dec 2016, pp. 1–7.

[RSC+18] B. Ramamurthy, R. T. Schwarz, W. G. Cowley, G. Bolding, and A. Knopp, "Passive Channel Orthogonality Measurement Technique for MIMO SATCOM," in *MILCOM 2018 - 2018 IEEE Mil. Commun. Conf.*, no. 2. IEEE, oct 2018, pp. 1–6.

[SCA18] S. K. Sharma, S. Chatzinotas, and P.-D. Arapoglou, Eds., *Satellite Communications in the 5G Era.* Institution of Engineering and Technology, jul 2018.

[SDSK19] R. T. Schwarz, T. Delamotte, K.-U. Storek, and A. Knopp, "MIMO Applications for Multibeam Satellites," *IEEE Trans. Broadcast.*, pp. 1–18, jan 2019.

[SES17a] SES, "Anzahl der TV-Haushalte in Deutschland nach Empfangsart am Hauptfernsehgerät 2017 (in Millionen)," 2017. [Online]. Available: https://de.statista.com/statistik/daten/studie/290180/umfrage/anzahl-der-tv-haushalte-in-deutschland-nach-empfangsart/

[SES17b] ——, "SES Annual Report 2017," SES, Chateau de Betzdorf, Tech. Rep., 2017.

[Sha48] C. E. Shannon, "A Mathematical Theory of Communication," *Bell Syst. Tech. J.*, vol. 27, no. 3, pp. 379–423, jul 1948.

[SHK15a] K.-U. Storek, C. A. Hofmann, and A. Knopp, "Interferometer for Measurements of the MIMO Satellite Channel at Ku-Band," in *2015 IEEE 82nd Veh. Technol. Conf.* IEEE, sep 2015, pp. 1–5.

[SHK15b] ——, "Measurements of phase fluctuations for reliable MIMO space communications," in *2015 IEEE Asia Pacific Conf. Wirel. Mob.*, no. 1. IEEE, aug 2015, pp. 157–162.

[SHK16] R. T. Schwarz, C. A. Hofmann, and A. Knopp, "Results of a MIMO Testbed with Geosynchronous Ku-Band Satellites," *20th Int. ITG Work. Smart Antennas*, pp. 93–97, 2016.

[SK17] K.-U. Storek and A. Knopp, "Fair User Grouping for Multibeam Satellites with MU-MIMO Precoding," in *GLOBECOM 2017 - 2017 IEEE Glob. Commun. Conf.* IEEE, dec 2017, pp. 1–7.

[SK19] R. T. Schwarz and A. Knopp, "MIMO Capacity of Co-Located Satellites in Longitude Separation," in *IEEE Int. Conf. Commun.*, 2019, pp. 1–7.

[SKL+08] R. T. Schwarz, A. Knopp, B. Lankl, D. Ogermann, and C. A. Hofmann, "Optimum-capacity MIMO satellite broadcast system: Conceptual design for LOS channels," *2008 4th Adv. Satell. Mob. Syst. - Proceedings, ASMS 2008*, pp. 66–71, aug 2008.

[SKL09] R. T. Schwarz, A. Knopp, and B. Lankl, "The channel capacity of MIMO satellite links in a fading environment: A probabilistic analysis," in *IWSSC'09 - 2009 Int. Work. Satell. Sp. Commun. - Conf. Proc.*, sep 2009, pp. 78–82.

[SKL11] ——, "Performance of an SC-FDE SATCOM system in block-time-invariant orthogonal MIMO channels," *GLOBECOM - IEEE Glob. Telecommun. Conf.*, pp. 1–6, dec 2011.

[SKL12] ——, "SC-FDE V-BLAST system concept for MIMO over satellite with antenna misalignment," *Int. Multi-Conference Syst. Signals Devices, SSD 2012 - Summ. Proc.*, pp. 1–8, mar 2012.

[SKO+08] R. T. Schwarz, A. Knopp, D. Ogermann, C. A. Hofmann, and B. Lankl, "Optimum-capacity MIMO satellite link for fixed and mobile services," in *2008 Int. ITG Work. Smart Antennas, WSA 2008*, feb 2008, pp. 209–216.

[SKO+09] R. T. Schwarz, A. Knopp, D. Ogermann, C. A. Hofmann, and B. Lank, "On the prospects of mimo satcom systems: The tradeoff between capacity and practical effort," in *2009 6th Int. Multi-Conference Syst. Signals Devices, SSD 2009*, mar 2009, pp. 1–6.

[SN06] I. Sarris and A. Nix, "Design and performance assessment of maximum capacity MIMO architectures in line-of-sight," *IEE Proc. - Commun.*, vol. 153, no. 4, p. 482, aug 2006.

[Soo94] E. M. Soop, *Handbook of Geostationary Orbits*, 1994th ed., J. R. Wertz, Ed. Dordrecht: Springer Netherlands, 1994.

[SRGdP15] G. A. Siles, J. M. Riera, and P. Garcia-del Pino, "Atmospheric Attenuation in Wireless Communication Systems at Millimeter and THz Frequencies [Wireless Corner]," *IEEE Antennas Propag. Mag.*, vol. 57, no. 1, pp. 48–61, feb 2015.

[ST12] W. L. Stutzmann and G. A. Thiele, *Antenna Theory and Design*. John Wiley & Sons, Inc., 2012.

[SUBW04] C. Swannack, E. Uysal-Biyikoglu, and G. Wornell, "Low complexity multiuser scheduling for maximizing throughput in the MIMO broadcast channel," in *Proc. Allert. Conf. Commun. Control Comput.*, 2004.

[SVK+17] R. T. Schwarz, F. Volk, A. Knopp, C. A. Hofmann, and K.-U. Storek, "The multiple-satellite MIMO channel of narrow band vehicular communications at UHF," in *MILCOM 2017 - 2017 IEEE Mil. Commun. Conf.* IEEE, oct 2017, pp. 447–452.

[SWK14] R. T. Schwarz, S. P. Winter, and A. Knopp, "MIMO application for reduced adjacent satellite interference in SATCOM downlinks," *2014 IEEE Int. Conf. Commun. ICC 2014*, pp. 3570–3575, 2014.

[TH07] X. Tang and Y. Hua, "Optimal Design of Non-Regenerative MIMO Wireless Relays," *IEEE Trans. Wirel. Commun.*, vol. 6, no. 4, pp. 1398–1407, apr 2007.

[Uni] Union of Concerned Scientists, "UCS Satellite Database." [Online]. Available: http://www.ucsusa.org/

[VPNC+16] M. A. Vazquez, A. Perez-Neira, D. Christopoulos, S. Chatzinotas, B. Ottersten, P.-D. Arapoglou, A. Ginesi, and G. Tarocco, "Precoding in Multibeam Satellite Communications: Present and Future Challenges," *IEEE Wirel. Commun.*, vol. 23, no. 6, pp. 88–95, dec 2016.

[VVL+12a] O. Vidal, G. Verelst, J. Lacan, E. Alberty, J. Radzik, and M. Bousquet, "Next generation High Throughput Satellite system," in *2012 IEEE First AESS Eur. Conf. Satell. Telecommun.* IEEE, oct 2012, pp. 1–7.

[VVL+12b] ——, "Next generation High Throughput Satellite system," in *2012 IEEE First AESS Eur. Conf. Satell. Telecommun.* IEEE, oct 2012, pp. 1–7.

[Whe01] A. D. Wheelon, *Electromagnetic Scintillation*, 1st ed. Cambridge: Cambridge University Press, 2001.

[WN12] J. Wang and S. Nakasuka, "Cluster flight orbit design method for fractionated spacecraft," *Aircr. Eng. Aerosp. Technol.*, vol. 84, no. 5, pp. 330–343, aug 2012.

[WSS06] H. Weingarten, Y. Steinberg, and S. Shamai, "The Capacity Region of the Gaussian Multiple-Input Multiple-Output Broadcast Channel," *IEEE Trans. Inf. Theory*, vol. 52, no. 9, pp. 3936–3964, sep 2006.

[Wyn94] A. Wyner, "Shannon-theoretic approach to a Gaussian cellular multiple-access channel," *IEEE Trans. Inf. Theory*, vol. 40, no. 6, pp. 1713–1727, 1994.

[YG06] T. Yoo and A. Goldsmith, "On the optimality of multiantenna broadcast scheduling using zero-forcing beamforming," *IEEE J. Sel. Areas Commun.*, vol. 24, no. 3, pp. 528–541, mar 2006.